UC Riverside

UC Riverside Electronic Theses and Dissertations

Title

Search for new Physics with Long-Lived Particles Decaying to Photons and Missing Energy in pp Collisions at a Center-of-Mass Energy of 7 TeV with the CMS Experiment at the LHC

Permalink

https://escholarship.org/uc/item/90k102cm

Author

Liu, Hongliang

Publication Date

2011

Peer reviewed|Thesis/dissertation

eScholarship.org Powered by the California Digital Library
University of California

UNIVERSITY OF CALIFORNIA
RIVERSIDE

Search for new Physics with Long-Lived Particles Decaying to Photons and Missing Energy in pp Collisions at a Center-of-Mass Energy of 7 TeV with the CMS Experiment at the LHC

A Dissertation submitted in partial satisfaction
of the requirements for the degree of

Doctor of Philosophy

in

Physics

by

Hongliang Liu

December 2011

Dissertation Committee:

Dr. Gail G. Hanson, Chairperson
Dr. Richard Seto
Dr. Ernest Ma

Copyright by
Hongliang Liu
2011

The Dissertation of Hongliang Liu is approved:

Committee Chairperson

University of California, Riverside

Acknowledgments

A "thank you" would not be enough to express my greatest gratitude for my advisor, Professor Gail Hanson. I would not have gone all the way without her guidance and generous support during the years. She is no doubt the most important influence in my scientific career. She encourages me for the original ideas of my own, helps me to put them into practice, provides help when needed. In such process, she drives me to advance and progress in my area. Also I would like to acknowledge her assistance in reading and correcting this thesis.

My very special thanks go to Dr. Kevin Burkett. He is a good friend and a great advisor at the LHC Physics Center at Fermilab. He was patiently teaching me every single technical detail of the CMS software since the very beginning of my PhD studies. He also provided me great help on the tracking software and kept encouraging me at the time when I started implementing my idea of tracker-seeded conversion reconstruction algorithm.

I must also thank Professor Yuri Gershtein, a close and great research partner. With his broad knowledge of experimental high energy physics and insight in problem solving, he has given me great help and precious suggestions through numerous constructive discussions which enables me to finish the analysis.

Then I want to thank Dr. Alexander Ledovskoy. Sasha is a co-worker in this analysis, dealing with all the crucial statistics and mathematics work. He helped us solve quite a lot of difficult problems. I enjoy the experience of working with him during the time.

I also need to express my gratitude for an honest scientist, a great teacher, Professor Nancy Marinelli. Working with her is a precious experience to encourage me

to persist the high and strict standard of scientific work.

I would like to thank Dr. Ning Chen for sharing his study of theoretical aspects of supersymmetry.

I would also like to thank Chris Heidt for his days of assistance in reading and correcting this thesis.

Finally, I want to express my thanks to my parents. Like most parents, they do not understand very much about their kid's expertise. It doesn't matter though for them to give out all the doubtless love, support and belief to encourage my wildest dream of being a scientist.

To my parents for their love and support.

To my young sister, for urging me to pursue the dreams of “the poetic, the afar”.

ABSTRACT OF THE DISSERTATION

Search for new Physics with Long-Lived Particles Decaying to Photons and Missing Energy in pp Collisions at a Center-of-Mass Energy of 7 TeV with the CMS Experiment at the LHC

by

Hongliang Liu

Doctor of Philosophy, Graduate Program in Physics
University of California, Riverside, December 2011
Dr. Gail G. Hanson, Chairperson

We perform a search for long-lived neutral particles decaying into a photon and invisible particles in pp collisions at a center-of-mass energy of 7 TeV at the Large Hadron Collider. In the context of gauge mediated supersymmetry with the lightest neutralino as the next-to-lightest supersymmetric particle and the gravitino as the lightest supersymmetric particle, the neutralino can decay into a gravitino and a photon with a non-zero lifetime. The impact parameter of the photon relative to the beam-beam collision point can be reconstructed using converted photons. The method is sensitive to lifetimes of the order of $\mathcal{O}(0.1$ ns). The data sample corresponds to an integrated luminosity of 2.1 ± 0.1 fb^{-1} recorded in the first part of 2011 by the CMS experiment at the LHC at $\sqrt{s} = 7$ TeV. The search is performed using events containing photons, missing transverse energy and jets. Upper limits at the 95% confidence level are presented on the cross section for such particles from pair-production, each of which decays into a photon and invisible particles.

Contents

List of Figures

List of Tables

Chapter 1

Introduction

The Standard Model (SM) of elementary particles provides an elegant theoretical framework. It is consistent with almost all experimental observations. However, the SM has its natural drawbacks and unsolved open questions, ranging from the origin of the particle masses to the nature of the Dark Matter in the Universe.

There are several alternative theories to the SM which try to answer these open questions. In these models, new physics, in terms of new particles and new interactions, is expected to be visible at the TeV energy scale. Supersymmetry (SUSY) is one of the well developed theories for physics beyond the SM. It foresees the existence of supersymmetric partners of the ordinary particles. If SUSY exists, it must be broken spontaneously, due to the fact that no mass-degenerate superpartners of the SM particles have been found. One of the SUSY breaking scenarios is gauge-mediated supersymmetry breaking (GMSB). In GMSB, the gravitino is the Lightest Supersymmetric Particle (LSP) and the lightest neutralino is the Next-to-Lightest Supersymmetric Particle (NLSP). The neutralino can decay into a gravitino and a photon with a non-zero lifetime.

An algorithm for the reconstruction of converted photons is presented. The algorithm selects the reconstructed tracks from the CMS tracking system and creates the converted photon track pairs using the photon conversion signatures. It provides a physics measurement that the regular photon reconstruction cannot: the photon direction. The photon direction is exploited to calculate the photon impact parameter, which can be used as an indication of long-lived particles decaying into photons.

In this dissertation, we reconstruct the impact parameter of the photon relative to the beam-beam collision point using converted photons. Then we use the photon impact parameter method to search for long-lived neutralinos decaying into photons. Upper limits at the 95% confidence level are presented on the cross section for such particles from pair-production, each of which decays into a photon and invisible particles.

The analysis has been completed with a dataset that corresponds to an integrated luminosity of 2.1 fb^{-1} collected by the Compact Muon Solenoid (CMS) experiment in 2011. The dissertation is organized as follows:

- A theoretical outline of the SM, supersymmetry and gauge-mediated supersymmetry breaking is discussed in Chapter 2;
- A description of the Large Hadron Collider and the CMS experiment are reviewed in Chapter 3;
- Data handling and event reconstruction are outlined in Chapter 4;
- Photon conversion reconstruction is discussed in details in Chapter 5;
- The search for new physics with long-lived particles decaying to photons and missing energy is presented in Chapter 6;
- The conclusions are given in Chapter 7.

Chapter 2

The Standard Model of Particle Physics and Supersymmetric Models

This chapter is dedicated to a theoretical outline of the Standard Model and Supersymmetric Models. Firstly, it gives a brief introduction to the Higgs boson and Higgs boson mass constraints in both theoretical and experimental views. Secondly, it presents the motivations of physics beyond the Standard Model. Thirdly, it introduces Supersymmetry as a possible alternative model. Last but not the least, it briefly reviews the Supersymmetry breaking mechanism and Gauge-Mediated Supersymmetry Breaking (GMSB). Finally, it discusses the gravitino as the Lightest Supersymmetric Particle (LSP) in GMSB models and the neutralino as Next to Lightest Supersymmetric Particle (NLSP), as well as the long-lived neutralino.

2.1 The Standard Model

The Standard Model (SM) of particle physics is a relativistic Quantum Field Theory concerning the electromagnetic, weak, and strong interactions of elementary particles. It includes 12 elementary particles of spin-$\frac{1}{2}$ known as fermions, which respect the Pauli exclusion principle, according to the spin-statistics theorem. Each fermion has a corresponding antiparticle. All fermions are categorized into three generations of leptons and quarks. The types of SM fermions are summarized in Table 2.1.

Table 2.1: The types of Standard Model fermions. There are three generations of quarks, each comprising an up-type quark and a down-type quark, and three generations of leptons, each comprising a charged lepton and the corresponding neutrino.

	Generation	Flavor	Symbol	Charge (e)
Lepton	1	electron neutrino	ν_e	0
		electron	e^-	-1
	2	muon neutrino	ν_μ	0
		muon	μ^-	-1
	3	tau neutrino	ν_τ	0
		tau	τ^-	-1
Quark	1	up	u	2/3
		down	d	-1/3
	2	charm	c	2/3
		strange	s	-1/3
	3	top	t	2/3
		bottom	b	-1/3

The SM is a non-Abelian Yang-Mills gauge theory [5], according to which all the fundamental forces are mediated by an exchange of the gauge fields, which can be described by a specific symmetry group. The symmetry group of the SM is $SU(3)_C \otimes SU(2)_L \otimes U(1)_Y$, where C stands for the color quantum number, L for the left-handed chirality (weak isospin) and Y for the hypercharge. This symmetry group has 8 gluons, 3 intermediate weak bosons and an abelian boson. In the framework of Quantum Field Theory, the SM is described by a Lagrangian written as

$$\mathcal{L}_{SM} = \mathcal{L}_{EW} + \mathcal{L}_{QCD} + \mathcal{L}_{Higgs} + \mathcal{L}_{Yukawa} \tag{2.1}$$

The first two terms, $\mathcal{L}_{EW}$ and $\mathcal{L}_{QCD}$, describe

- free fermions,
- free gauge bosons associated with the $SU(2)_L \otimes U(1)_Y$ and the $SU(3)_C$ gauge symmetries,
- the interaction between fermions and gauge bosons,
- the interaction among gauge bosons.

The third term $\mathcal{L}_{Higgs}$ represents

- the electroweak symmetry breaking,
- the Higgs particle.

The last term $\mathcal{L}_{Yukawa}$ describes the flavor physics (e.g. quarks and leptons).

Both gauge bosons and fermions acquire their masses due to the spontaneous symmetry breaking of $SU(2)_L \otimes U(1)_Y$ in the Higgs mechanism. The Higgs mechanism

requires the introduction of a complex scalar field ϕ, the Higgs field, which is represented as a $SU(2)$ doublet of scalar fields ϕ_i

$$\phi = \begin{pmatrix} \phi^+ \\ \\ \phi^- \end{pmatrix} = \frac{1}{\sqrt{2}} \begin{pmatrix} \phi_1 + i\phi_2 \\ \\ \phi_3 + i\phi_4 \end{pmatrix} \tag{2.2}$$

The Dirac fermion can be described in terms of left-handed (L) and right-handed (R) chiral states (Weyl fermion fields):

$$\psi = \begin{pmatrix} \psi_L \\ \\ \psi_R \end{pmatrix} \tag{2.3}$$

where $\psi_L = \frac{1}{2}(1-\gamma^5)\psi$ and $\psi_R = \frac{1}{2}(1+\gamma^5)\psi$. The left-handed fermions ψ_L transform as isospin doublets under $SU(2)_L$ gauge transformation, while the right-handed ones ψ_R transform as isospin signlets.

A vacuum state can be arbitrarily chosen at $\phi_3 = v$ and $\phi_1 = \phi 2 = \phi 3 = 0$. An expansion can be made around the minimum:

$$\phi = \frac{1}{\sqrt{2}} \begin{pmatrix} 0 \\ \\ v + h(x) \end{pmatrix} \tag{2.4}$$

where v stands for the vacuum expectation value (VEV) and $h(x)$ for a real scalar Higgs field. With this choice of ϕ, the $\mathcal{L}_{Higgs}$ provides the mass terms for the $W^\pm$ and Z bosons, while the photon remains massless:

$$\left(\frac{1}{2}vg\right)^2 W_\mu^+ W^{-\mu}, \left(\frac{1}{2}v\sqrt{g^2+(g')^2}\right)^2 Z_\mu Z^\mu \tag{2.5}$$

and the $W^\pm$ and Z boson masses are:

$$M_{W^\pm} = \frac{1}{2}vg \tag{2.6}$$

$$M_Z = M_{W^\pm}/\cos\theta_W \tag{2.7}$$

where θ_W is the weak mixing angle (Weinberg angle). It is the angle by which spontaneous symmetry breaking rotates the original W^0 and B^0 vector boson plane and produces the Z boson and the photon.

$$\begin{pmatrix} \gamma \\ Z^0 \end{pmatrix} = \begin{pmatrix} \cos\theta_W & \sin\theta_W \\ -\sin\theta_W & \cos\theta_W \end{pmatrix} \begin{pmatrix} B^0 \\ W^0 \end{pmatrix} \tag{2.8}$$

Several couplings arise between the gauge bosons and the scalar Higgs field $h(x)$, which is associated to a new scalar particle, the Higgs boson. This boson has mass of $\sqrt{2\lambda}v$, where λ stands for the strength of the Higgs field self interaction. This boson carries no electric charge. It has a weak isospin component -1/3, and a weak hypercharge $Y = 1$. Since λ is a free parameter in the SM, the Higgs boson mass cannot be predicted in the SM and remains an unknown.

Several searches for the Higgs boson have been performed. The direct searches at the Large Electron-Positron (LEP) collider set a lower limit on the Higgs mass at 114.4 GeV/c^2 at the 95% C.L. [6]. The Tevatron experiments at CDF and DØ excluded the mass range of 156 to 177 GeV/c^2 at the 95% C.L. [7]. Recently, the two LHC experiments at CMS and ATLAS excluded 141-476 GeV/c^2 at the 95% C.L. [8, 9].

2.2 Open Questions in Standard Model

The Standard Model is consistent with almost all experimental observations. However, it has its natural drawbacks and unsolved theoretical problems. The most relevant ones to this thesis are described below.

Hierarchy problem

The "Hierarchy Problem" is related the Higgs mass stability under radiative corrections, which can be described in terms of

$$\Delta m_H^2 = -\frac{|\lambda_f|^2}{8\pi^2}[-2\Lambda^2 + 6m_f^2 \cdot \ln(\Lambda/m_f)...], \tag{2.9}$$

where m_f is the fermion mass, λ_f is the fermion coupling to the Higgs and Λ is the cut-off used in the integrals. The fermion loop diagram is shown in Figure 2.1.

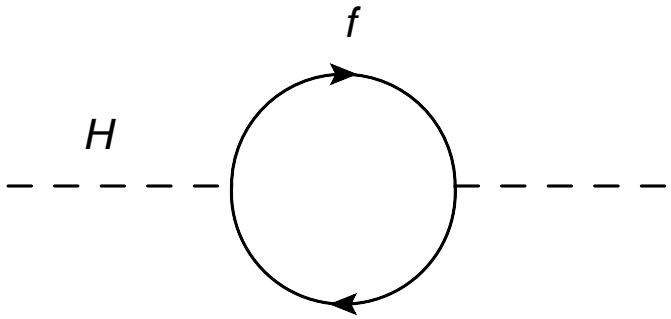

Figure 2.1: One-loop correction to the Higgs squared mass parameter m_H^2, due to a Dirac fermion.

In the SM, the Δm_H^2 correction is quadratic divergent. It is known that the SM is only effective under a low-energy condition, so a cut-off Λ should be imposed on these internal momenta, corresponding to the scale of new physics. Only gravity at Planck scale ($M_p = \sqrt{\hbar c/G_N} \approx 10^{19}$ GeV) has a higher energy scale than the electroweak scale ($m_{W,Z} \approx 10^2$ GeV). If one assumes $\Lambda = M_p$, the Δm_H^2 correction should be several orders of magnitude larger than the expected value for the Higgs mass (around 100 GeV). In order to adjust the electroweak scale to be much smaller than the Planck scale, the SM requires several fine tunings of parameters.

Unification of Gauge couplings

The Grand Unification Theories (GUT) [10] are based on the hypothesis that all known interactions of the SM are merged into one single interaction. It is characterized by one larger gauge symmetry, thus one unified coupling constant. If GUT excludes the very small contribution of the gravity, the unification of strong, weak and electromagnetic couplings to a single GUT coupling should occur at some high energy scale, which is far from the low energy range in the current experiments.

In the SM according to the renormalization group equation, the coupling constants evolve as a function of the energy scale Q:

$$\alpha_i^{-1} = \alpha_i^{-1}(m_Z) + \frac{b_i}{2\pi} \log \frac{Q}{m_Z} \tag{2.10}$$

where $\alpha_i = g_i^2/4\pi$ for different coupling constants g_3 (strong), g_2(weak) and g_1(electromagnetic), $\alpha_i^{-1}(m_Z)$ is the coupling constant calculated at the Z boson mass m_Z scale, and b_i is a coefficient characteristic of each coupling which depends on the number of generations of quarks and leptons and the number of Higgs doublets. The evolution of the inverse of the coupling α_i^{-1} is shown in Figure 2.2 as a function of the logarithm of energy scale. The values of the coupling constants do not converge to a common value at any scale, which means the unification can only be obtained under the condition that new physics appears between the electroweak scale and the Planck scale.

The SM has some other weaknesses:

- It provides masses for all the elementary fermions except the neutrino. However, neutrino masses are now considered to be experimentally established from atmospheric neutrino oscillations [11, 12].

- It does not provide any convincing explanations for the imbalance in baryonic and

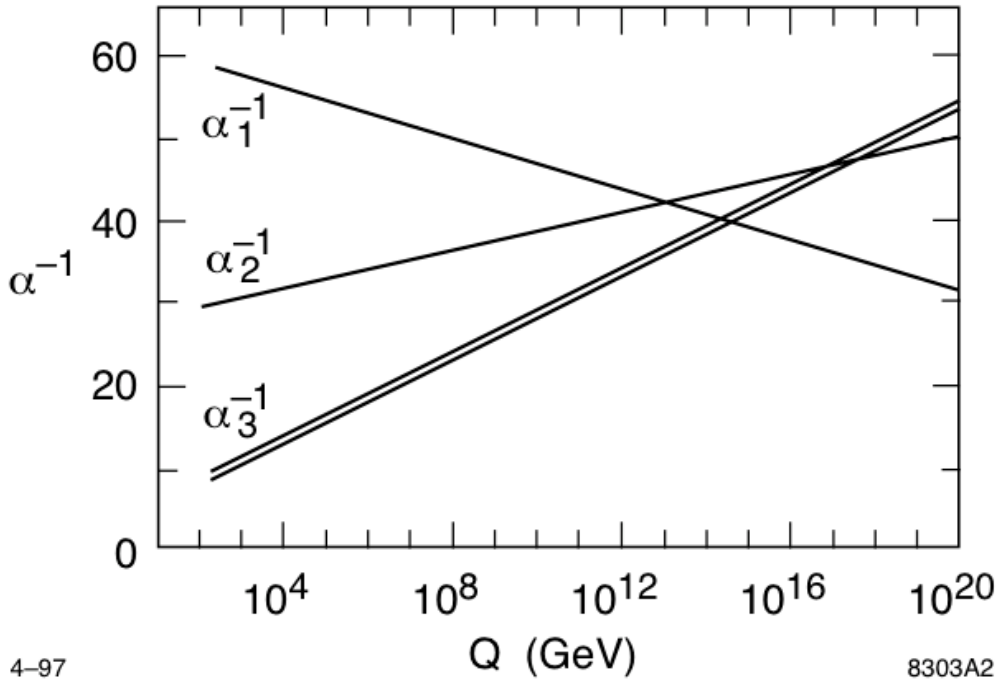

Figure 2.2: Evolution of the inverse of the coupling constants in the SM [1]. The theoretical error bands on α_3^{-1} are shown.

anti-baryonic matter observed in the Universe.

- It does not explain the gravitational force.
- It cannot explain the amount of cold dark matter (CDM) which gives far too large contributions to dark energy.

The discussions above are the most important open questions in the SM. Several alternative models, including for example String Theory [13] and Extra Dimensions [14], have been proposed in the last decades to answer these questions. Among them, supersymmetry is considered to be one of the promising theories for the new physics beyond the SM.

2.3 Supersymmetry

Supersymmetry (SUSY) [15] is a symmetry that relates elementary particles of one spin to other particles (superpartners) that differ by 1/2 spin. It uses a SUSY operator to turn a bosonic quantum state into a fermionic state, and vice versa,

$$Q|Boson\rangle = |Fermion\rangle \tag{2.11}$$

$$Q|Fermion\rangle = |Boson\rangle \tag{2.12}$$

where Q is the generator of the SUSY algebra [16]. SUSY should be invariant under the Q transformation, which requires that each fermion of the SM correspond to a supersymmetric boson, and vice versa (Figure 2.3).

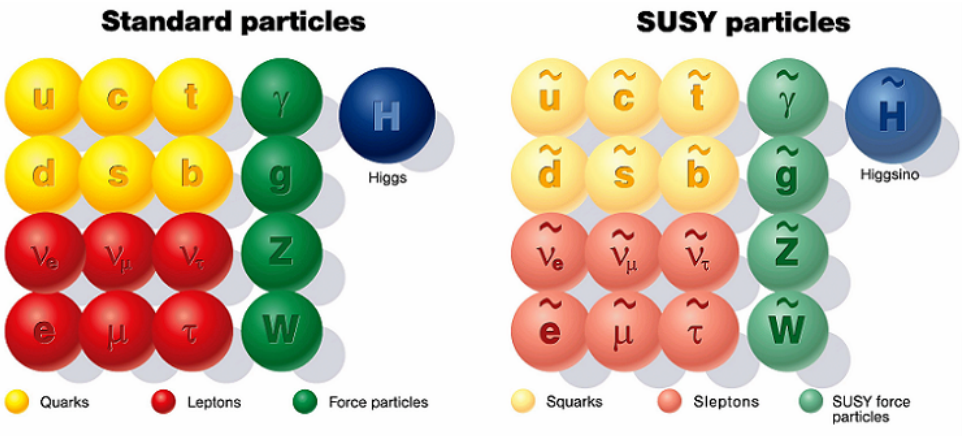

Figure 2.3: A schematic picture of the SM particles and the relative supersymmetric partners.

SUSY is one of the well developed theories for physics beyond the Standard Model. It not only preserves the consistency of all SM results confirmed by current experiments, but also excludes the quantum loop effects that cause the hierarchy problem.

It gives a scalar superpartner S for a new one-loop correction (Figure 2.4).

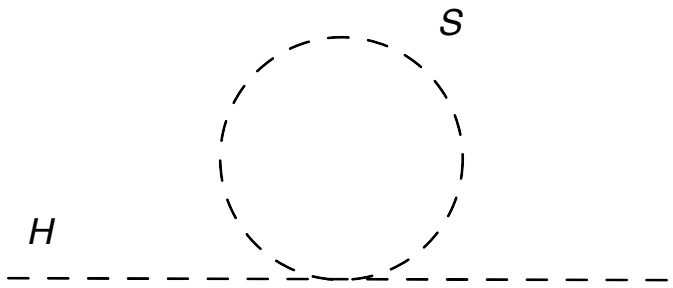

Figure 2.4: One-loop scalar correction to the Higgs mass.

Then the Δm_H^2 correction for S is

$$\Delta m_H^2 = 2 \cdot \frac{\lambda_S}{16\pi^2}[-2\Lambda^2 + 6m_S^2 \cdot \ln(\Lambda/m_S)...], \tag{2.13}$$

where the Δm_H^2 is positive because of the spin-statistics theorem, which means fermion wavefunctions are antisymmetric so the swap of wavefunctions gets a minus contribution, while boson wavefunctions are symmetric for a positive contribution. By comparing with Equation 2.9, if

$$(\lambda_f)^2 = \lambda_S,$$

$$m_f = m_S,$$

the quadratic divergence in the hierarchy problem is canceled.

In addition, SUSY also provides the unification of the three gauge coupling constants at the GUT energy scale below the Planck scale. The convergence of the three coupling constants is shown in Figure 2.5.

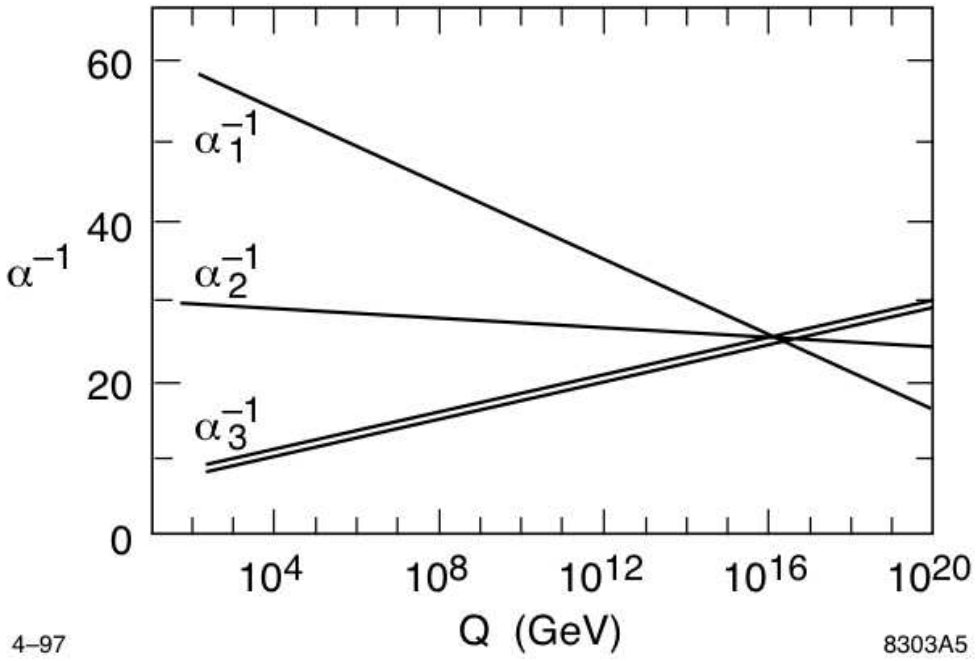

Figure 2.5: Evolution of the gauge couplings to high energy scales, using the renormalization group equation of the supersymmetric generalization of the SM [1]. The theoretical error bands on α_3^{-1} are shown.

2.4 The Minimal Supersymmetric Standard Model

The Minimal Supersymmetric Standard Model (MSSM) is the minimal extension of the Standard Model that includes SUSY [16]. In this minimal version of SUSY, the number of particles is doubled, with an additional Higgs doublet with its superpartner.

The particle content of the MSSM is presented in Table 2.2. There is one supersymmetric partner for each of the SM particles. There are two Higgs doublets. The notation rule of the SUSY particles uses the suffix "s-" before the name of the corresponding SM fermion, for example quark/s-quark. It uses the ending "-ino" after the name of the corresponding SM boson, for example Higgs/Higgs-ino.

If SUSY were a perfect symmetry of Nature, superpartners should have the

Table 2.2: The particle content of the MSSM.

SM Particle type	Particle	Symbol	Spin	R-Parity	Superpartner	Symbol	Spin	R-parity
Fermions	Quark	q	$\frac{1}{2}$	+1	Squark	$\tilde{q}$	0	-1
	Lepton	ℓ	$\frac{1}{2}$	+1	Slepton	$\tilde{\ell}$	0	-1
Bosons	W	W	1	+1	Wino	$\tilde{W}$	$\frac{1}{2}$	-1
	B	B	1	+1	Bino	$\tilde{B}$	$\frac{1}{2}$	-1
	Gluon	g	1	+1	Gluino	$\tilde{g}$	$\frac{1}{2}$	-1
Higgs bosons	Higgs	h_u,h_d	0	+1	Higgsinos	$\tilde{h}_u$, $\tilde{h}_d$	$\frac{1}{2}$	-1

same mass as their SM counterparts and should have already been discovered by experiments. The absence of such discoveries can be explained by SUSY being a broken symmetry, with SUSY masses large enough to evade current experimental bounds.

The Lagrangian of the MSSM can be presented as

$$\mathcal{L}_{MSSM} = \mathcal{L}_{SUSY} + \mathcal{L}_{Breaking} \tag{2.14}$$

where the first term $\mathcal{L}_{SUSY}$ is the SUSY generalization of the SM Lagrangian, and the second term $\mathcal{L}_{Breaking}$ describes the SUSY breaking.

Due to the SUSY breaking, MSSM states can mix to form the physical mass eigenstates. Five Higgs bosons are produced after electroweak symmetry breaking:

- two CP-even neutral states, h^0 and H^0,
- a CP-odd neutral state, A^0,
- two charged states $H^{\pm}$.

The neutral gaugino states ($\tilde{B}$, $\tilde{W^0}$) and neutral higgsino states ($\tilde{H_u^0}$, $\tilde{H_d^0}$), the superpartners of the Higgs boson, mix to form four neutral mass eigenstates, $\tilde{\chi_1^0}$, $\tilde{\chi_2^0}$, $\tilde{\chi_3^0}$, $\tilde{\chi_4^0}$ (in order of increasing mass by convention). The charged wino states ($\tilde{W^+}$, $\tilde{W^-}$) and higgsino states ($\tilde{H_u^+}$, $\tilde{H_d^-}$) mix to create four charginos, $\tilde{\chi_1^{\pm}}$, $\tilde{\chi_2^{\pm}}$. Gauge and mass eigenstates in MSSM are listed in Table 2.3.

The states can be labeled with a multiplicative quantum number called R-parity which is defined as

$$R_p = (-1)^{3(B-L)+2s}, \tag{2.15}$$

where B stands for the baryon number, L for the lepton number and s for the spin of

Table 2.3: The gauge and mass eigenstate particles in the MSSM.

Names	Spin	Gauge Eigenstates	Mass Eigenstates
squarks	0	$\tilde{u}_L\ \tilde{u}_R\ \tilde{d}_L\ \tilde{d}_R$	same
		$\tilde{s}_L\ \tilde{s}_R\ \tilde{c}_L\ \tilde{c}_R$	same
		$\tilde{t}_L\ \tilde{t}_R\ \tilde{b}_L\ \tilde{b}_R$	$\tilde{t}_1\ \tilde{t}_2\ \tilde{b}_1\ \tilde{b}_2$
sleptons	0	$\tilde{e}_L\ \tilde{e}_R\ \tilde{\nu}_e$	same
		$\tilde{\mu}_L\ \tilde{\mu}_R\ \tilde{\nu}_\mu$	same
		$\tilde{\tau}_L\ \tilde{\tau}_R\ \tilde{\nu}_\tau$	$\tilde{\tau}_1\ \tilde{\tau}_2\ \tilde{\nu}_\tau$
neutralinos	1/2	$\tilde{B}$, $\tilde{W}^0$, $\tilde{H}_u^0$, $\tilde{H}_d^0$	$\tilde{\chi}_1^0$, $\tilde{\chi}_2^0$, $\tilde{\chi}_3^0$, $\tilde{\chi}_4^0$
charginos	1/2	$\tilde{W}^+$, $\tilde{W}^-$, $\tilde{H}_u^+$, $\tilde{H}_d^-$	$\tilde{\chi}_1^\pm$, $\tilde{\chi}_2^\pm$
gluino	1/2	$\tilde{g}$	same
gravitino	3/2	$\tilde{G}$	same

the particle. $R_p = +1$ is required for the SM particles, with the Higgs boson included, and $R_p = -1$ for the SUSY superpartners.

R-parity conservation has two effects. One is suppressing proton decay and the other is preventing any mixing between SM and SUSY particles. In addition, R-parity conservation plays important roles for the following experimental searches:

- Any initial state created in laboratories has a R_p value of +1, which implies the pair-production of SUSY particles.
- Every SUSY particle decays to a $R_p = -1$ state which has an odd number of SUSY particles.
- The Lightest Supersymmetric Particle (LSP) is stable due to energy and R-parity conservation laws.

2.5 Supersymmetry Breaking Mechanisms

If SUSY exists it must be broken spontaneously, due to the fact that no mass-degenerate superpartners of the SM particles have been found. The breaking mechanism should preserve the renormalizability of the theory as well as the cancellation of quadratic divergences to maintain the hierarchy of the energy scales as discussed before. A symmetry breaking can be introduced into the theory by adding a term called "soft-breaking," which has only SUSY particles in the Lagrangian density, defined as

$$\mathcal{L}_{soft} = -(\frac{1}{2}M_a\lambda^a\lambda^a + \frac{1}{6}a^{ijk}\phi_i\phi_j\phi_k + \frac{1}{2}b^{ij}\phi_i\phi_j) + c.c. - (m^2)^i_j\phi^{j*}\phi_i \tag{2.16}$$

where $(m^2)^i_j$ and b^{ij} stand for the squared scalar mass terms, a^{ijk} for the cubic scalar couplings and M_a for the gaugino mass terms for each gauge group.

This "soft-breaking" procedure explicitly breaks the symmetry, and introduces 105 new parameters into the theory in total:

- 21 masses, 36 mixing angles, 40 CP-violating phases in the squark and slepton sector;
- 5 real parameters and 3 CP-violating parameters in the Higgs sector.

The number of the free parameters can be largely reduced by assuming the existence of an underlying mechanism which produces the SUSY breaking in a natural way. Any form of spontaneous symmetry breaking, such as the Higgs mechanism, is not possible in the MSSM, because none of the fields can have non-zero VEV to break SUSY without spoiling the gauge invariance.

The most common framework for SUSY breaking models is based on a so-called "hidden sector," in which the symmetry is broken spontaneously [17, 18]. Accordingly, there should be two sectors: the visible sector containing the usual MSSM fields and the

hidden sector containing additional fields which lead to the breaking of SUSY. The SUSY breaking, which occurs at some high energy in the hidden sector, is mediated to the visible sector by the exchange of the weakly interacting "messengers." This mediation mechanism, however, depends strongly on the assumptions of the model framework.

The most common scenarios are:

- gauge mediation (GMSB) [19, 20]
- gravity mediation (mSUGRA) [21]
- gaugino mediation [22]
- anomaly mediation (AMSB) [23]

We concentrate on gauge mediated supersymmetry breaking in this thesis.

2.6 Gauge-Mediated Supersymmetry Breaking

The GMSB scenario, as a low-energy SUSY breaking scenario, includes three sectors:

- The visible sector. It contains the particles of MSSM, i.e. quarks, leptons, gauge bosons and two Higgs doublets, together with their superpartners.
- The hidden sector. It is responsible for the SUSY breaking. It contains a collection of as yet unobserved quantum superfields and the corresponding hypothetical particles, which do not interact via the SM force messengers, such as gluons, photons, and W/Z bosons.
- The messenger sector. It is represented by some new superfields Φ and $\bar{\Phi}$. These new superfields interact with MSSM via $SU(3)_C \otimes SU(2)_L \otimes U(1)_Y$ and couple to a

chiral superfield X of the hidden sector at tree level, via some Yukawa interaction.

The earliest and simplest implementation is the minimal GMSB (MGM), which involves communication of the SUSY breaking from the hidden sector through a single set of vectors, such as the messenger sectors. The Yukawa interaction between the chiral superfield X and the messengers Φ is given by the superpotential term

$$W = \lambda X \bar{\Phi} \Phi \tag{2.17}$$

The chiral superfield X acquires a non-zero VEV of its scalar and the auxiliary components

$$\langle X \rangle = M_m + \theta^2 F_m \tag{2.18}$$

where θ stands for an additional "Grassman" coordinate of the superspace with units of energy$^{-1/2}$, M_m ([mass]) and F_m ([mass^2]) represent fundamental mass scales, which can be from several TeV up to the GUT scale. According to Equation 2.18, the coupling between Φ and X generates masses (M_{Φ_1,Φ_2}) for the messenger fields (order of M_m) and the mass-squared splittings between the components of the messenger multiplets (order of F_m), defined as

$$(M_{\Phi_1,\Phi_2})^2 = (M_m)^2 + F_m \tag{2.19}$$

where the λ in Equation 2.17 can be absorbed in the definitions of M_m and F_m. Therefore, $\sqrt{F_m}$ can be used as a measure of SUSY breaking in the messenger sector.

In addition, the relation

$$M_m \ll M_p \tag{2.20}$$

should be satisfied in order to keep the gravitational interactions negligible (M_p is the Planck mass). The messenger squared mass is positive, thus it requires

$$F_m < (M_m)^2. \tag{2.21}$$

The visible sector is affected by the SUSY breaking in the messenger sector. In the visible sector, ordinary particles are degenerate at tree level, due to the fact that they do not directly couple to the chiral field X. The mass splittings of these particles arise because of the gauge interactions between the MSSM and the messenger fields.

Through this mechanism, the SUSY breaking is transmitted from the hidden sector to the visible sector and then assigns mass to the gaugino λ_i and the scalar particle ϕ of the MSSM:

$$m_{\lambda_i} = N_m \cdot \Lambda \cdot f_\lambda(\alpha_i) \tag{2.22}$$

$$m_\phi = N_m \cdot \Lambda \cdot f_\phi(\alpha_i) \tag{2.23}$$

where $\Lambda = F_m/M_m$ stands for the effective SUSY breaking scale in the visible sector, N_m for the number of Φ messenger generations and f_λ, f_ϕ for the three gauge coupling constants α_i in the SM.

The MGM predicts that all scalar and gaugino mass terms are related by using a single messenger mass scale $\sqrt{F_m}$. Sparticles obtain masses proportional to powers of their gauge couplings. Therefore, there is a large mass hierarchy in the spectrum. For example, if the next-to-lightest supersymmetric particle (NLSP) is a colored sparticle, the inclusive signature is di-jets plus missing energy. Therefore, the bounds (approximately 300 GeV) tend to be similar to those found in searches for MSUGRA [24]. According to the naturalness, it is not realistic that the lower bound of the MSSM sparticle spectrum is so high. With the spectrum of the MGM pushed higher, some non-minimal GMSB models become more interesting.

Simple extensions to the MGM have been studied in Ref [25, 26]. One of the promising extensions is the general gauge mediation (GGM). A simple framework [27] is proposed for counting allowed parameters in the GGM schemes. The GGM requires that

"*in the limit that the MSSM gauge couplings* $\alpha_i \to 0$*, the theory decouples into the MSSM and a separate hidden sector that breaks SUSY* [27]". Then the SM gauge group must be part of a weakly-gauged global symmetry of the hidden sector. All the dependence of the soft masses on the hidden sector are interpreted by total six parameters: three real parameters for the sfermion masses, and three complex parameters for the gaugino masses.

In addition, there are some low scale gauge mediation scenarios [28]. The SM-like Higgs boson can decay into pairs of lightest neutralinos ($H \to \tilde{\chi}_1^0 \tilde{\chi}_1^0$), each of which decays to a photon and a gravitino, $\tilde{\chi}_1^0 \to \gamma + \tilde{G}$.

2.7 The Gravitino as the Lightest Supersymmetric Particle

As a result of the spontaneous SUSY breaking, the physical spectrum contains a massless spin-1/2 fermion (the goldstino) coming from the fermionic component of the chiral superfield X. When a global supersymmetric theory is coupled to the gravity and promoted to a local supersymmetric theory, the goldstino is absorbed by the longitudinal component of the gravitino field (the supersymmetric partner of the graviton with a spin 3/2). The gravitino acquires a mass

$$m_{\tilde{G}} = \frac{F_0}{\sqrt{3} M_p} \tag{2.24}$$

where F_0 stands for the fundamental scale of the SUSY breaking. In the minimal GMSB model, a dimensionless factor C_{grav} can be introduced and defined as

$$C_{grav} = \frac{F_0}{F_m}. \tag{2.25}$$

The mass of the gravitino can be represented in terms of C_{grav} as

$$m_{\tilde{G}} = \frac{C_{grav}}{\sqrt{3}} \cdot \frac{F_0}{M_p} \sim C_{grav} \left(\frac{\sqrt{F_m}}{100\text{TeV}} \right)^2 2.4\text{eV}. \tag{2.26}$$

In the GMSB models, the mass of other SUSY particles is above 100 GeV. $m_{\tilde{G}}$ is lower than a few GeV, and therefore the gravitino is the LSP for any relevant value of $\sqrt{F_m}$.

2.8 The Lightest Neutralino as the Next-to-Lightest Supersymmetric Particle

In gauge mediation, the LSP is a nearly-massless gravitino as discussed in the previous section. The lightest MSSM superpartner is then the next-to-lightest supersymmetric particle (NLSP). The NLSP always decays into the gravitino and its SM superpartner in a universal way. In the GMSB, the lightest MSSM sparticle is the lightest neutralino $\tilde{\chi}_1^0$. We use GGM as a case study to have a general discussion of the neutralino.

The general neutralino NLSP can be any linear combination of bino, wino, and Higgsino gauge eigenstates [29]:

$$\tilde{\chi}_1^0 = \sum_{i=1}^{4} N_{1i} \tilde{\psi}_i^0 \tag{2.27}$$

where $\tilde{\psi}_i^0 = (\tilde{B}, \tilde{W}, \tilde{H}_d^0, \tilde{H}_u^0)$. The mass eigenvectors N_{1i} depend on four MSSM parameters: M_1, the soft mass for the bino; M_2, the soft mass for the wino; μ, the supersymmetric Higgs mass; and $\tan\beta$, the ratio of the up-type to down-type Higgs VEVs.

A general neutralino NLSP has three possible decay modes, $\tilde{\chi}_1^0 \to \gamma + \tilde{G}$, $\tilde{\chi}_1^0 \to Z + \tilde{G}$ and $\tilde{\chi}_1^0 \to h + \tilde{G}$. The different gauge eigenstates are characterized by

different branching ratios to respective decay modes. The formulas for the decay widths are [30, 25]:

$$\begin{aligned}
\Gamma(\tilde{\chi}_1^0 \to \gamma + \tilde{G}) &= |N_{11}c_W + N_{12}s_W|^2 \,\mathcal{A} \\
\Gamma(\tilde{\chi}_1^0 \to Z + \tilde{G}) &= \left(|N_{12}c_W - N_{11}s_W|^2 + \frac{1}{2}\,|N_{13}c_\beta - N_{14}s_\beta|^2\right)\left(1 - \frac{m_Z^2}{m_{\tilde{\chi}_1^0}^2}\right)^4 \mathcal{A} \\
\Gamma(\tilde{\chi}_1^0 \to h + \tilde{G}) &= \frac{1}{2}\,|N_{13}c_\beta + N_{14}s_\beta|^2 \left(1 - \frac{m_h^2}{m_{\tilde{\chi}_1^0}^2}\right)^4 \mathcal{A}
\end{aligned} \tag{2.28}$$

where $\mathcal{A}$ sets the scale of the neutralino lifetime:

$$\mathcal{A} = \frac{m_{\tilde{\chi}_1^0}^5}{16\pi F_0^2} \approx \left(\frac{m_{\tilde{\chi}_1^0}}{100\ \text{GeV}}\right)^5 \left(\frac{100\ \text{TeV}}{\sqrt{F_0}}\right)^4 \frac{1}{0.1\ \text{mm}}. \tag{2.29}$$

where $\sqrt{F_0}$ stands for the fundamental scale of the SUSY breaking, related to the gravitino mass via $m_{3/2} = F_0/(\sqrt{3}M_P)$. The range of the possible $\sqrt{F_0}$ is

$$10\ \text{TeV} \lesssim \sqrt{F_0} \lesssim 10^6\ \text{TeV}. \tag{2.30}$$

The branching ratios of the bino-like and the wino-like neutralino NLSP are shown in Figure 2.6 [29]. One can find that the binos dominantly decay into photons with a branching ratio proportional to $\cos^2\theta_W$. A subdominant component of binos decay into Z's, with a branching ratio proportional to $\sin^2\theta_W$. For a neutral wino-like NLSP, the branching ratios are flipped and most wino NLSP decays mostly to Z's. A higgsino NLSP dominantly decays to Z or h, with a branching ratio that depends on the value of $\tan\beta$ and the sign of μ.

The neutralino NLSP lifetime is determined by the fundamental scale of the SUSY breaking ($\sqrt{F_0}$), as in Equation 2.29. For $\sqrt{F_0} \lesssim 10^2$ TeV, the neutralino generally decays promptly [31]. For $\sqrt{F_0}$ between $\sim 10^2 - 10^3$ TeV, if the lifetime is in the range of $\mathcal{O}(10$ ns), the neutralino can decay a measurable distance from its production point but inside the detector, referred as "long-lived." Most studies of long-lived neutralinos use

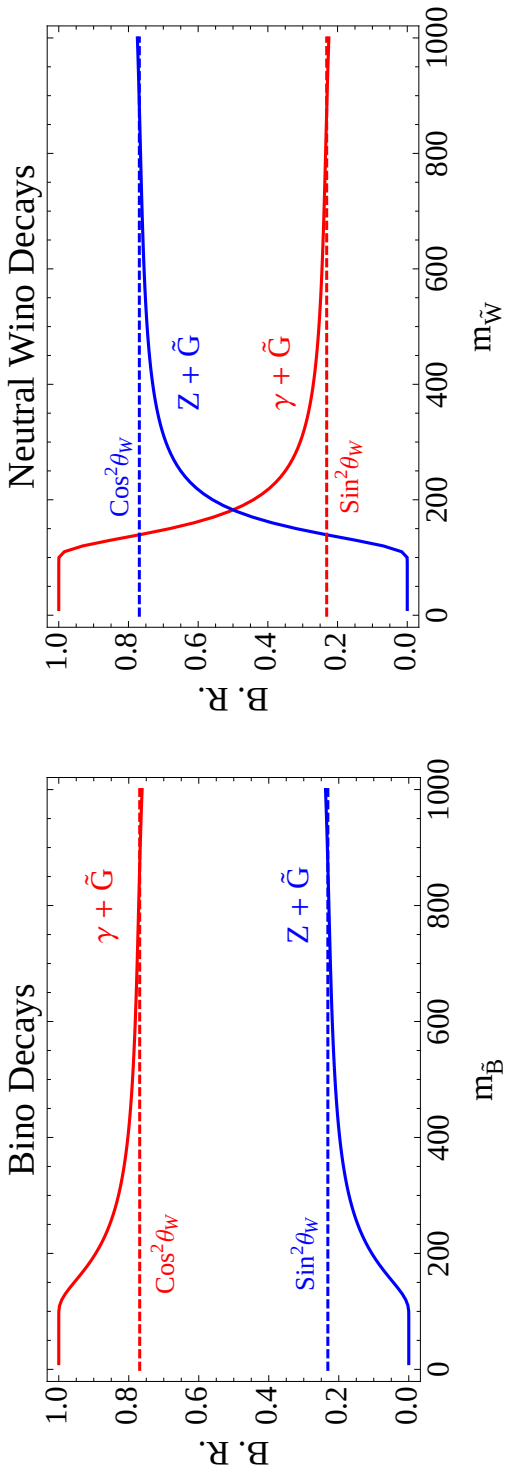

Figure 2.6: The bino and neutral wino NLSP branching ratios to Z or γ, plus gravitino [2]. The branching ratio is determined by the weak mixing angle, and by the phase space suppression of decays into Zs at low mass.

only the wino-like ones. They search for Z in the final state [31, 32] by reconstructing the displaced vertices of $Z \to \ell\ell$ or $Z \to jets$. In this thesis, we present a novel method to study the bino-like long-lived neutralino decaying into photons. The process is

$$\begin{aligned} p + p &\to \tilde{s}_1 \tilde{s}_2 + J \\ (\tilde{s}_{1,2} &\to \tilde{\chi}_1^0 + X_{1,2} \to \tilde{G} + \gamma + J_{1,2}) \\ &\to 2\tilde{G} + 2\gamma + J' \end{aligned} \tag{2.31}$$

where $\tilde{s}_1$, $\tilde{s}_2$ stand for generic sparticles and J, $J_{1,2}$, J' for SM particles. A schematic view of this process is illustrated in Figure 2.7.

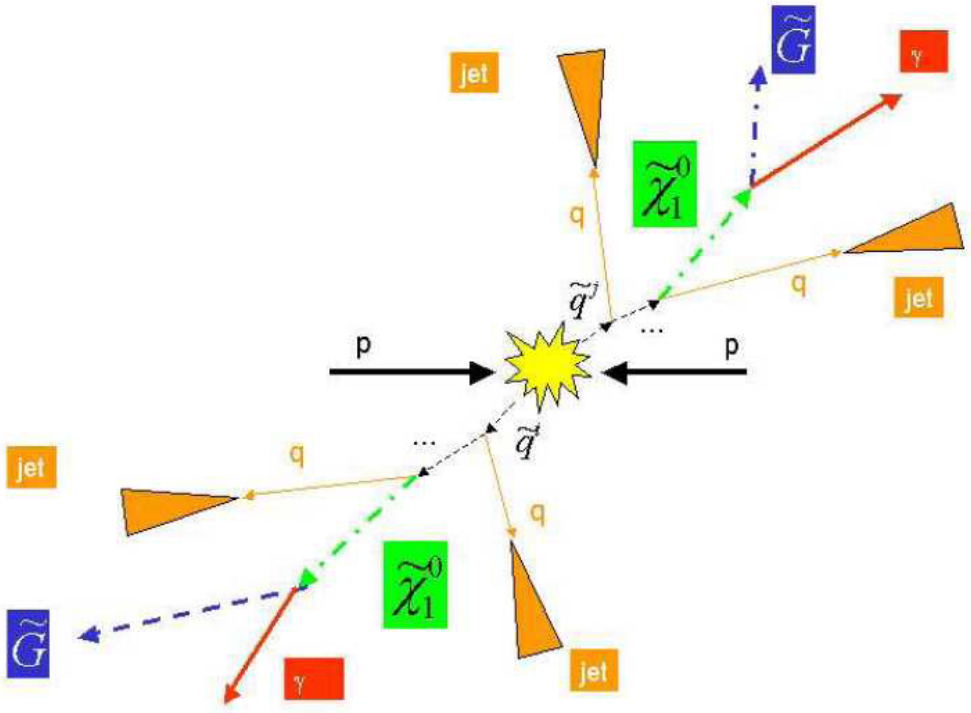

Figure 2.7: A schematic view of a GMSB event where the neutralino $\tilde{\chi}_1^0$ is the NLSP and decays into $\tilde{\chi}_1^0 \to \gamma + \tilde{G}$. A pair of generic squarks ($\tilde{q^i}$, $\tilde{q^j}$) is produced in a pp collision. Each of them starts a decay chain in which quarks q are generated. At the end, two NLSPs ($\tilde{\chi}_1^0$) from decays of the squarks both decay into a LSP ($\tilde{G}$) and a photon (γ).

Chapter 3

The Large Hadron Collider and the CMS Detector

Overall descriptions of the Large Hadron Collider (LHC) and the Compact Muon Solenoid (CMS) experiment are provided in this chapter.

3.1 The Large Hadron Collider

The Large Hadron Collider (LHC) [33, 34] at CERN is the largest and highest-energy particle accelerator in the world. It is a two-ring superconducting hadron accelerator installed into the existing 27 km long tunnel previously occupied by Large Electron Positron (LEP), as much as 175 meters beneath the French-Swiss border near Geneva, Switzerland. The LHC is capable of providing proton-proton collisions at a center-of-mass energy $\sqrt{s} = 14$ TeV, with a design luminosity of 10^{34} cm^{-2}s^{-1}. The schematic layout of the LHC is shown in Figure 3.1.

On September 10th, 2008, the proton beams were successfully circulated in the main ring of the LHC for the first time. Unfortunately only nine days later, operations

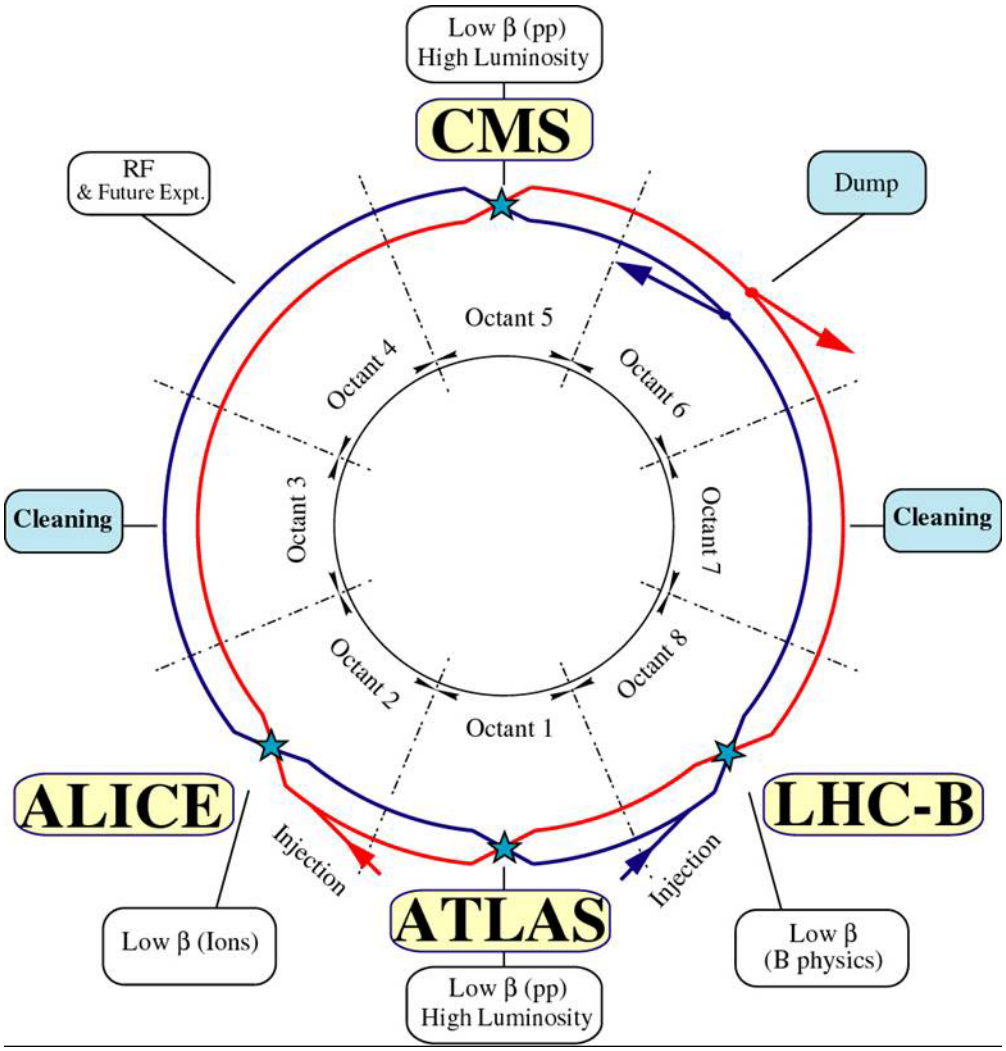

Figure 3.1: Schematic layout of the LHC (Beam 1 - clockwise, Beam 2 - counterclockwise)

were halted due to a serious accident that an electrical fault in the bus between magnets caused a rupture and a leak of six tones of liquid helium. A year later when the repair work was finished, the first proton-proton collisions were recorded on November 23rd, 2009, at the injection energy of 450 GeV per beam. On March 30th, 2010, the first planned collisions at $\sqrt{s} = 7$ TeV started. Collisions planned at $\sqrt{s} = 14$ TeV will be performed at the beginning of 2013.

The high luminosity of the LHC is obtained by a high frequency bunch crossing and a high number of protons per bunch: two beams of protons at an energy of 7 TeV, circulating in two different vacuum chambers, and each beam contains 2808 bunches. The bunches, with a nominal 10^{11} protons each, have a very small transverse spread ($\sigma_x \approx \sigma_y \approx 15\mu m$) and a longitudinal spread of 7.5 cm long in the beam direction at the interaction points. The bunches collide at the rate of 40 MHz, i.e. one collision each 25 ns.

The LHC can also accelerate and collide beams of ionized lead nuclei, such as Pb^{82+}, at 2.76 TeV to study the deconfined state of matter: the quark-gluon plasma. A summary of the main technical parameters of the LHC is given in Table 3.1. There are four interaction points: the two at high luminosity are devoted to the multi-purpose CMS [35] and ATLAS (A Toroidal LHC Apparatus) [36] experiments. The other two, at lower luminosity, are used by ALICE (A Large Ion Collider Experiment) and LHCb (LHC beauty), optimized respectively for heavy-ion physics and b quark physics.

The acceleration in colliders is performed on the high-density bunches of particles. The interaction rate is proportional to the luminosity $\mathcal{L}$, which can be calculated

Parameter	Value
Circumference [km]	27
Number of magnet dipoles	1232
Dipolar magnetic field [T]	8.33
Radio frequency [MHz]	400
Number of bunches	2808
Magnet temperature [K]	1.9
Nominal beam energy [TeV]	7
Nominal luminosity [cm^2s^{-1}]	10^{34}
Initial beam energy [TeV]	3.5
Protons per bunch	1.05×10^{11}
Bunch spacing [m]	7.48
Bunch time separation [ns]	25
RMS bunch length [cm]	7.5
Crossing angle [rad]	2×10^{-4}
Beam lifetime [h]	7
Luminosity lifetime [h]	10

Table 3.1: Main LHC technical design parameters

as:

$$\mathcal{L} = f \frac{n_1 n_2}{4\pi\sigma_x\sigma_y} \tag{3.1}$$

where n_1 and n_2 are the number of protons in each bunch, f is the collision frequency and σ_x, σ_y represent the Gaussian beam profile in the transverse plane. Figure 3.2 shows the performance of the luminosity delivery and recording in the CMS experiment, with about 90% efficiency for the CMS data taking [37, 38].

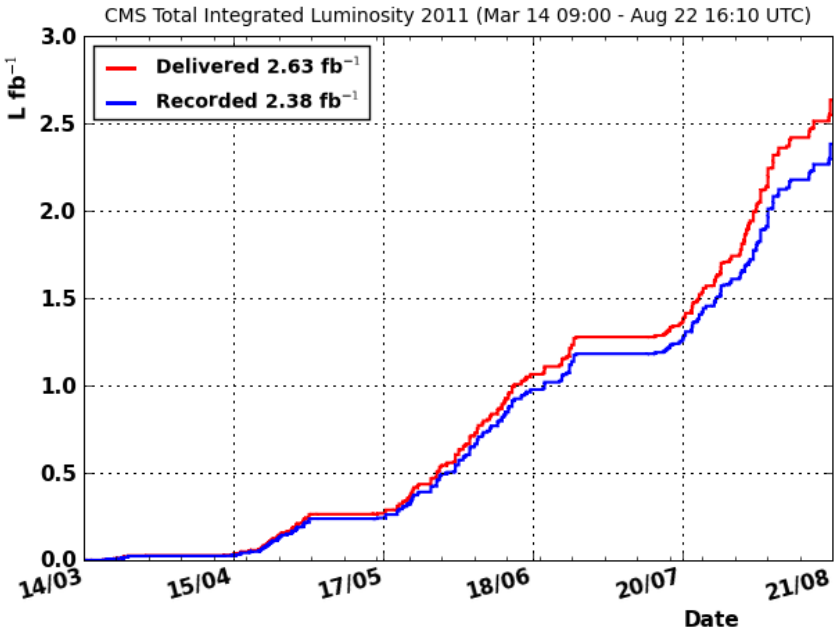

Figure 3.2: Integrated luminosity of the LHC in the CMS experiment for 2011 as a function of time, showing delivered (red) and recorded (blue) values.

In order to record the high frequency collisions of the LHC, the detectors should have a fast response time and a fine granularity. The detectors should also have good resistance in the high radiation environment. The following requirements should be satisfied:

- precise determination of charged particles momentum and impact point via an efficient tracking system;
- excellent reconstruction of high momentum photons and electrons;
- accurate reconstruction of hadronic activity from QCD processes and heavy particle decays;
- complete coverage to provide precise measurements of missing transverse energy and momentum.

The detector of the Compact Muon Solenoid experiment meets all these stringent requirements. A detailed description of the mechanical characteristics and performance of the CMS detector is provided in the next section.

3.2 The CMS Detector

The Compact Muon Solenoid (CMS) detector is designed to capture the ephemeral phenomena of the rich and diverse physics program at the LHC. The main feature of the CMS detector is a very strong magnetic field of 3.8 T generated by a superconducting solenoid, which allows for a compact design. A more detailed description of the technical design has been published [3]. The detector is designed for:

- a redundant efficient muon detection system;
- an excellent electromagnetic calorimeter;
- a high quality tracking system;
- a 4π hadron calorimeter.

3.2.1 The Coordinates

An overall view of the CMS detector is presented in Figure 3.3.

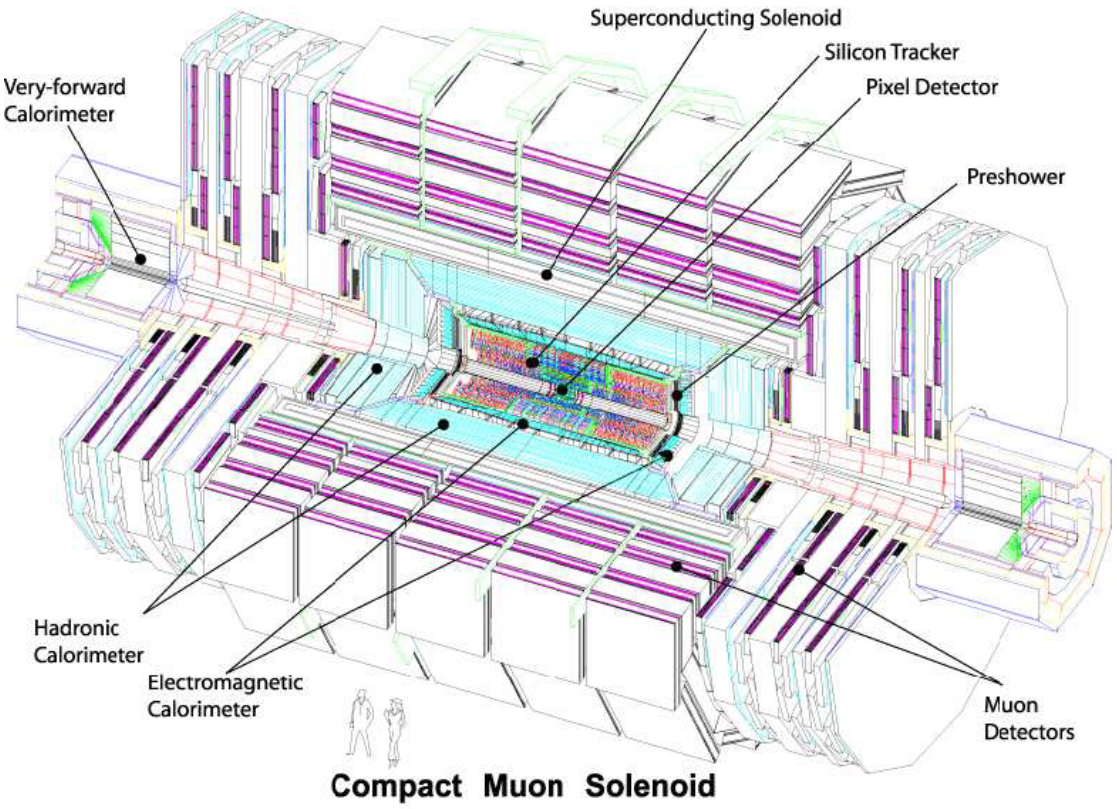

Figure 3.3: The complete CMS detector [3].

The CMS reference frame is centered at the Interaction Point of CMS (P5) at the LHC. The natural coordinate frame used to describe the detector geometry is a Cartesian system with:

- x axis pointing to the center of the LHC ring;
- y axis directed upwards along the vertical;
- z axis coincident with the CMS cylinder axis along the direction of the proton beam.

The cylindrical symmetry of the CMS design drives the use of a pseudo-angular reference frame. The pseudo-angular reference frame is given by the triplet (r, ϕ, η), where r is the distance from the z axis, ϕ is the azimuthal coordinate with respect to the x axis, and the pseudorapidity η, defined as:

$$\eta = -\ln \tan \frac{\theta}{2} \tag{3.2}$$

where θ is the polar angle with respect to the z axis.

In the following sections, a series of introductions to the different components of the detector will be presented individually. Particular attentions are paid on the CMS tracker and the electromagnetic calorimeter (ECAL), for the great importance of these two sub-detectors, which are vital to our studies involving long-lived particles decaying into high energy photons with photon conversions. The trigger system, used for the online event selection, and the software tools will also be discussed.

3.2.2 The Magnet of CMS

The choice of a compact design for the CMS detector imposes a strong solenoidal magnetic field, to give optimal resolution for the measurement of the momenta for charged tracks.

The magnet system provides a uniform magnetic field of 3.8 T using a 13 m long superconducting coil with a diameter of 5.9 m. The magnetic flux is returned via a 1.8 m thick saturated iron yoke. The solenoid is composed for the coil winding (divided into four parts) with its mechanical support, the thermal radiation shield and the vacuum tank. There is also a cooling system to ensure the security in case of sudden power failure.

As the biggest element of the CMS detector, the magnet system also provides

the principal supporting structure for all the barrel detector components, e.g. the muon system outside the coil, and the tracking system and the calorimeters inside.

The magnet system also includes the cryogenic system, power supply, quench protection, vacuum pumping, and control system.

3.2.3 The Tracker

3.2.3.1 The Pixel Detector

The pixel detector is the sub-detector system which is the closest to the interaction region. It is designed to deliver precise tracking points (hits) on charged particle trajectories in r - ϕ and z, with a spatial resolution in the range of 15-20 μm. It consists of three barrel layers, and two endcap disks on either end, as shown in Figure 3.4. The diameters of these three barrel layers are 4.4 cm, 7.3 cm and 10.2 cm, with identical lengths of 53 cm. The two end disks, from 6 to 15 cm in radius, are placed on each side at $|z| = 34.5$ cm and 46.5 cm. This design allows each track to have at least two points in the $|\eta| < 2.2$ region for tracks originating within $2\sigma_z$ from the central interaction point. The total number of channels is about 44 million, organized in about 16000 modules of 52 columns and 80 rows. The active area is close to 0.92 m^2. The presence of a high magnetic field causes a noticeable drift of the electrons (and a smaller drift for the holes) from the ionizing point along the track with a Lorentz angle of about 32 degrees. This leads to a charge sharing between pixels which, using an analog readout, can be exploited to considerably improve the resolution to about 10 μm. In the endcaps, the modules of the detector are arranged in a turbine-like shape with a tilt of 20 degrees, again in order to enhance charge sharing, as shown in Figure 3.4.

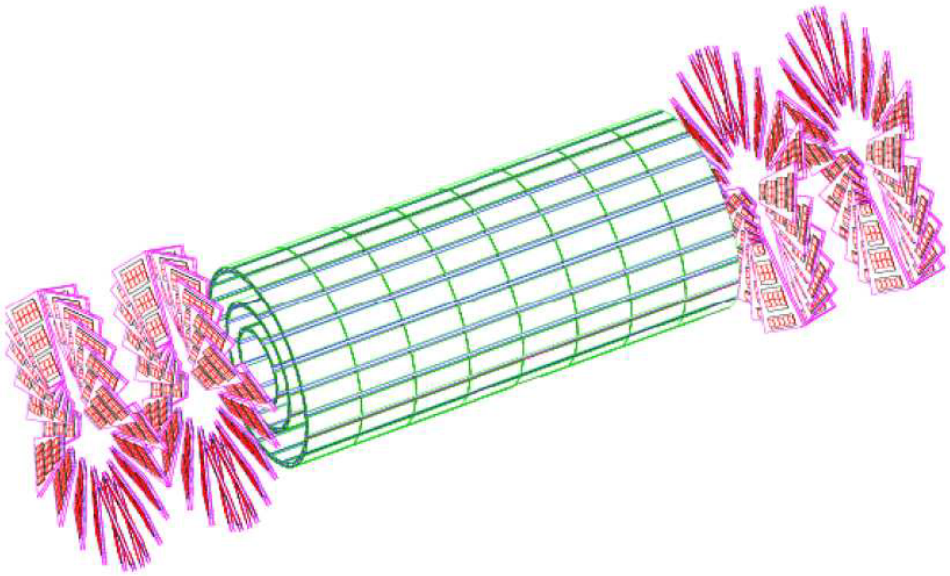

Figure 3.4: Three dimensional view of the silicon pixel detector of the CMS tracker [3].

3.2.3.2 The Silicon Strip Tracker

The inner and outer silicon strip tracker detector is shown in Figure 3.5. The sensors are based on silicon p+ strips on an n-type bulk 320 and 500 μm thick respectively for the inner and outer tracker. In the barrel the strips are parallel to the beam axis while for the endcaps they lie in a radial orientation.

The inner tracker consists of four barrel layers (Tracker Inner Barrel - TIB) and the endcaps (Tracker Inner Disks - TID) count three disks each end. The modules in the first two layers of the TIB carry a second module which is mounted back-to-back with a stereo angle of 100 mrad; we call these modules the "double-sided modules" (colored in red in Figure 3.5). The double-sided modules in layers 1 and 2 provide a single point resolution of 23 μm and 35 μm in the transverse $r - \phi$ plane, and the resolution of 230 μm in z axis. Each TID disk contains 3 rings of strip sensors with mean pitch varying from 100 μm to 141 μm, with the first two rings populated with double-sided modules.

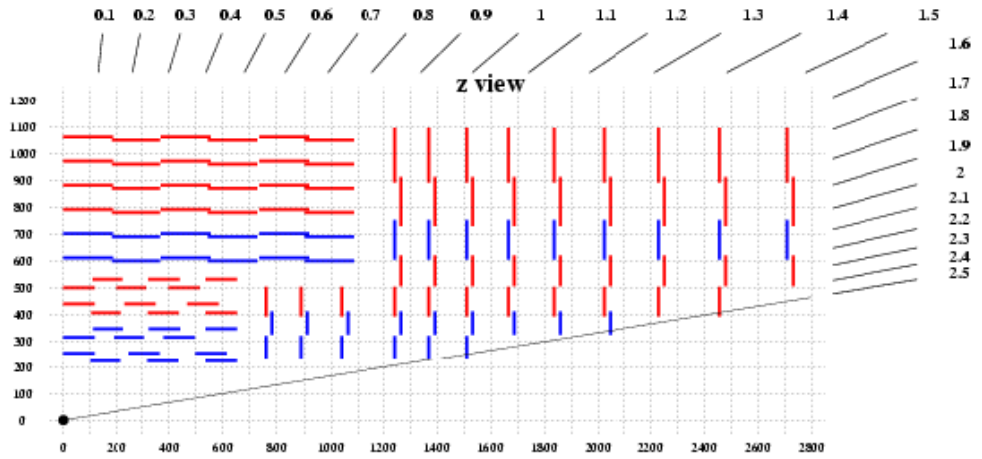

Figure 3.5: Schematic longitudinal view of a quarter of the silicon strip tracker layout (1/4 of the tracker). Red lines represent single modules, blue lines double-sided modules [3].

The outer tracker, placed surrounding the inner one, consists of Tracker Outer Barrel (TOB) and Tracker EndCaps (TEC). The TOB has six layers in the barrel and the innermost two layers are double-sided; the TEC are made of nine layers and the first, the second and the fifth are double-sided. The TOB covers the radial region between 55 cm and 116 cm and extends along the z axis between $\pm$118 cm. The TEC consist of two sections covering the region 124 cm $< |z| <$ 282 cm and 22.5 cm $< r <$ 113.5 cm; the section located in the positive (negative) z region is referred to as TEC+ (TEC-).

On the whole, the silicon strip tracker is made of about 10 million of channels, with an active area of about 198 m^2, enclosed in the cylindrical volume with a radius of 116 cm and a length of 540 cm; it provides a coverage for tracking up to $|\eta| < 2.5$.

The CMS Tracker operating in a 3.8-T solenoidal magnetic field was designed to provide robust and precise reconstruction of charged-particle momenta in the high occupancy environment of LHC collisions. This inevitably led to a substantial amount of Tracker material [39] (as shown in Figure 3.6). The direct consequence is that a

large fraction of photons convert into e^+e^- pairs while traversing the Tracker material, and the electrons and positrons have a large probability of emission of bremsstrahlung radiation along their trajectories, called "Photon conversions". The photon conversion reconstruction is discussed in Chapter 5.

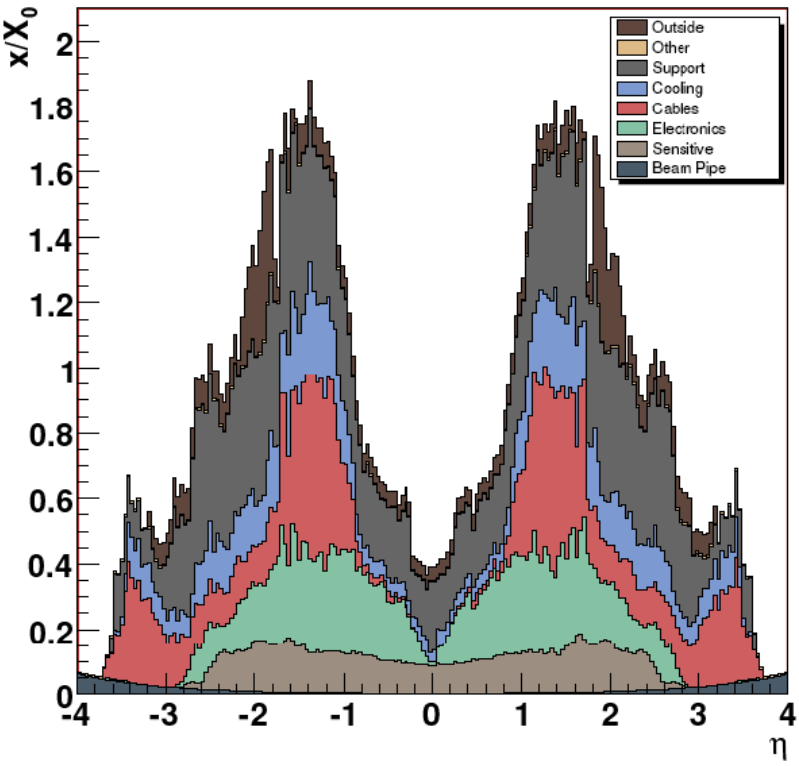

Figure 3.6: Tracker material as a function of η. The thickness is expressed in terms of radiation length (X_0). The peak around $|\eta| <= 1.5$ corresponds to the cables and services of the tracker [3].

3.2.4 The Electromagnetic Calorimeter

A high performance electromagnetic calorimeter (ECAL) is a fundamental requirement for precise measurements of electrons and photons in almost every general purpose of LHC experiment. The CMS collaboration has chosen a homogeneous calorimeter composed of segmented crystals of lead tungstate ($PbWO_4$), which is a radiation resis-

tant and chemically inert scintillator, suitable for the high-radiation environment of the LHC.

The CMS ECAL consists of a central part (barrel) and two caps (endcaps) to ensure the complete coverage. A three-dimensional presentation of the barrel and endcap electromagnetic calorimeter is shown in Figure 3.7. The principal design requirements are driven by the necessity of accurate measurement of electrons, photons and missing energy.

The engineering design aims in particular at minimizing the amount of material in front of the calorimeter, optimizing the interface with the tracking system, ensuring hermeticity by minimizing the gaps between adjacent crystals or in the barrel-endcap transition regions and stabilizing the crystal temperature within a tenth of a degree.

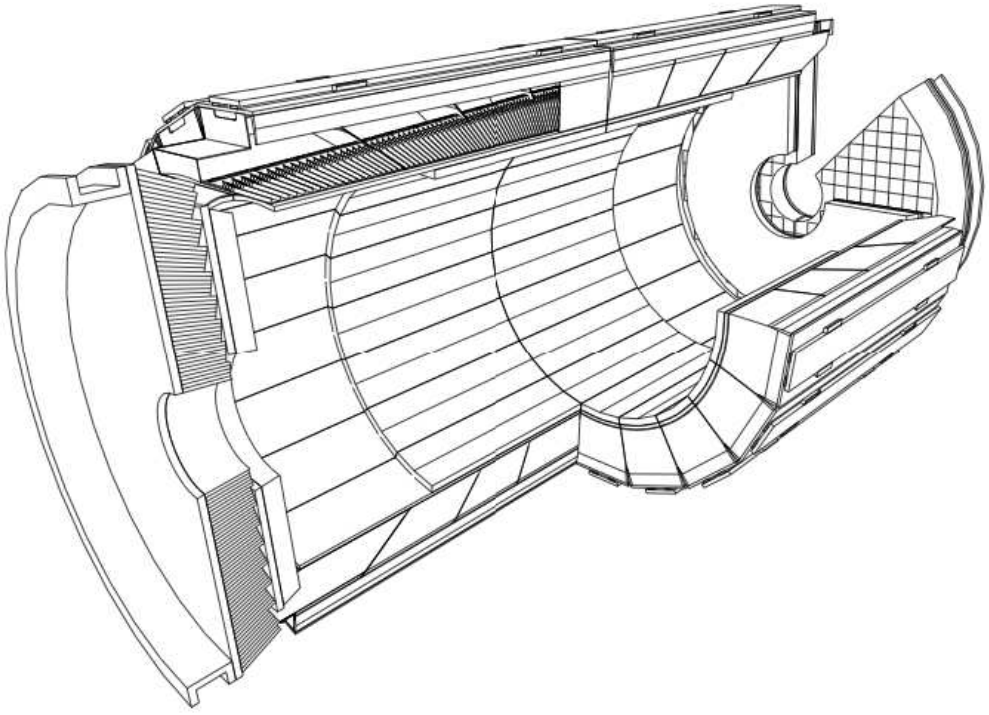

Figure 3.7: A three-dimensional view of the ECAL [3].

Figure 3.8 shows the longitudinal section of a quarter of the CMS ECAL. The barrel region covers a pseudorapidity range of $|\eta| < 1.479$. It consists of 2×18 supermodules, each of which contains 20 crystals in ϕ and 85 crystals in η. In both detector halves in η, each supermodule is divided into four supporting structures called modules. There are 17 different crystal types in the barrel: each crystal has a length of 230 mm, corresponding to 25.8 radiation lengths, and a front face area of approximately $22 \times 22\text{mm}^2$. The resulting granularity of the ECAL is $\Delta\eta \times \Delta\phi = 0.0175 \times 0.0175$. The crystals are tapered and their longitudinal axes have a constant off-pointing angle of 3° with respect to the nominal vertex position in both η and ϕ. This configuration increases the hermeticity of the structure because it avoids gaps that are pointing back to the interaction region.

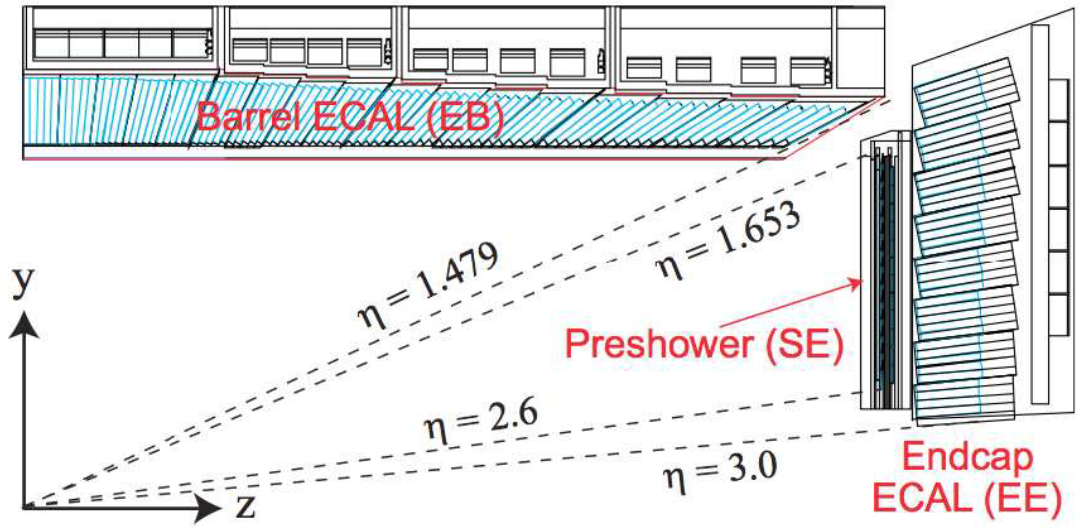

Figure 3.8: Longitudinal view of a quarter of the ECAL [3].

The ECAL endcaps provide accurate energy measurement in the pseudorapidity range of $1.48 < |\eta| < 2.6$. To further increase the ECAL hermeticity, crystals are installed up to $|\eta| < 3$. Endcap crystals with identical shape and dimensions are

grouped into 5×5 matrices of crystals ($2.6 \times 2.6 \times 22\text{cm}^3$). These matrices are called supercrystals. The crystals of the endcaps are shorter than the ones of the barrels due to the presence of a $3X_0$ thick preshower detector placed in front of the calorimeter.

The photon reconstruction using the ECAL will be discussed in Chapter 5.

3.2.5 The Hadronic Calorimeter

The hadron calorimeter (HCAL), which surrounds the ECAL, is used together with the ECAL to measure the energy and direction of hadronic jets coming from the fragmentation of quarks and gluons, the transverse energy (E_T) and the imbalance of it (E_T^{miss}). High hermeticity is required and proper thicknesses of material are required to contain the whole hadron shower.

The CMS HCAL is a sampling calorimeter made of the alternating layers of 3.7 mm thick active plastic scintillators and 5 cm thick brass plate absorbers. The signal is read out with the wavelength-shifting fibers. The CMS HCAL includes the HCAL Barrel (HB), the HCAL Endcaps (HE), the Outer Hadronic Calorimeter (HO) and the Forward Hadronic Calorimeter (HF). The barrel (HB) granularity is $\Delta\eta \times \Delta\phi = 0.087 \times 0.087$, matching the 5×5 crystals ECAL tower, which is sufficient to separate jets. A longitudinal view of HCAL is shown in Figure 3.9: the barrel ($|\eta| < 1.4$) and the endcap ($1.4 < |\eta| < 3.0$) with an overall thickness from 8.9 to 10 interaction lengths λ_I (16.42 cm) respectively. Since the barrel part of the calorimeter does not provide sufficiently containment for the very high energy showers and late initiated hadron showers, an additional tail-catcher, composed of scintillators tiles, is placed outside the magnet.

To improve the hermeticity, a very forward calorimeter (HF) is placed outside

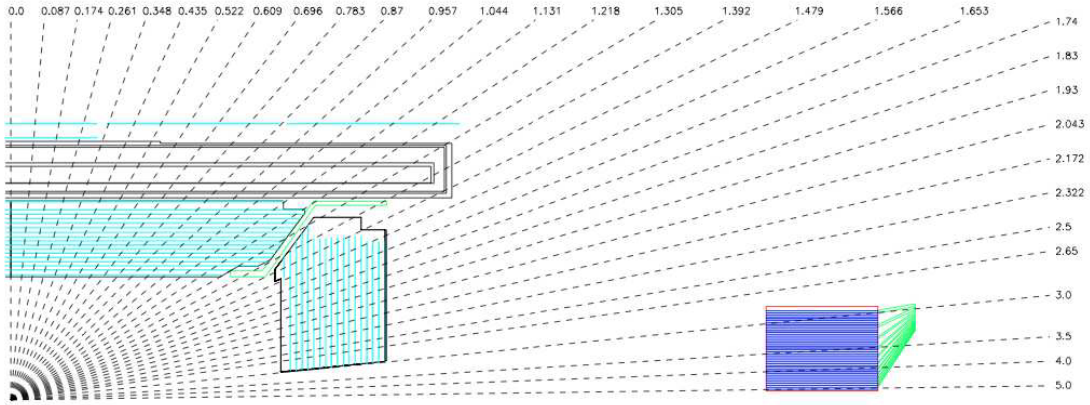

Figure 3.9: Longitudinal view of a quarter of the CMS hadron calorimeter, divided into barrel and endcap HCAL. It is placed inside the magnet coil, the outer barrel tail-catcher and the very forward calorimeter HF [3].

the magnet yoke, at ±11.2 m away along the beam direction from the nominal interaction point, covering $3 < |\eta| < 5$. Each HF is azimuthally subdivided into 18 wedges; each wedge is further subdivided into two halves. Quartz fibers are used as the active elements and are placed parallel to the beam pipe, interleaved into the steel plate absorbers which form the passive material. With this configuration, the HCAL has an overall depth of more than $11 \times \lambda_I$ of the entire coverage. The design hadronic energy resolution of the combined barrel HCAL and ECAL is [40]:

$$\frac{\sigma(E)}{E} = \frac{100\%}{\sqrt{E}} \oplus 4.5\% \tag{3.3}$$

where E is in GeV. The design resolutions of the HF are:

$$\frac{\sigma(E)}{E} = \frac{182\%}{\sqrt{E}} \oplus 9\%, \text{for hadrons} \tag{3.4}$$

$$\frac{\sigma(E)}{E} = \frac{138\%}{\sqrt{E}} \oplus 5\%, \text{for electrons} \tag{3.5}$$

3.2.6 The Muon System

The muon system is designed for muon identification, precise momentum measurement and triggering. Good muon momentum resolution and trigger capability are enabled by the high-field solenoidal magnet and its flux-return yoke. The latter also serves as a hadron absorber for the identification of muons. In the CMS experiment, the muon detectors are placed beyond the calorimeters and solenoid. Since the muon system consists of about 25000 m^2 of detection planes, the muon chambers have to be inexpensive, reliable and robust.

The layout of the muon system is shown in Figure 3.10. The muon system consists of three types of gaseous particle detectors: Drift Tubes (DT), Cathode Strip Chambers (CSC), and Resistivity Plate Chambers (RPC).

The 250 drift tube (DT) chambers in the barrel region cover the pseudorapidity region $|\eta| < 1.2$ and are organized into four stations interspersed with the layers of the flux return plates. The number of chambers in each station and their orientation are chosen to link together efficiently the muon hits from different stations together into a single muon track and also reject the background hits.

In the endcap regions of CMS, the cathode strip chambers (CSC) are used for the high rates, background levels of the muons, and the large, non-uniform magnet field. The CSCs identify muons between $0.9 < |\eta| < 2.4$. There are four stations of CSCs in each endcap, with chambers positioned perpendicular to the beam line and interspersed between the flux return plates. A crucial characteristic of the DT and CSC sub-systems is that they can trigger on the transverse momentum of muons with good efficiency and high background rejection, independent of the rest of the detector.

Because of the uncertainty in the ability of the muon system to measure the

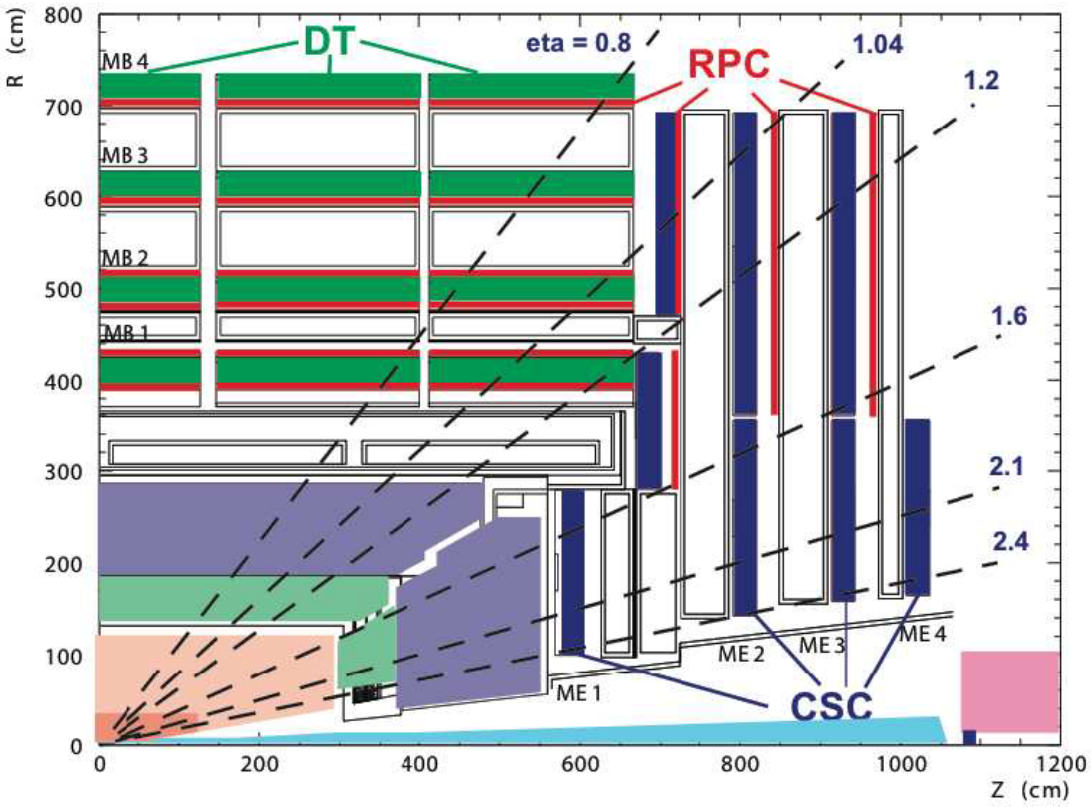

Figure 3.10: Layout of one quarter of the CMS muon system [3].

correct beam-crossing time when the LHC reaches the full luminosity, a complementary, dedicated trigger system consisting of resistive plate chambers (RPC) is added in both the barrel and endcap regions. The RPCs can provide a fast, independent and highly-segmented trigger with a sharp transverse momentum threshold over a large portion of the pseudorapidity range ($|\eta| < 1.6$ for the first period of data taking) of the muon system. The RPCs are double-gap chambers, operated in avalanche mode to ensure good operation at high rates.

3.2.7 The trigger system

At the nominal LHC luminosity, the LHC provides proton-proton collisions with a bunch crossing rate of 40 MHz, with an expected event rate of about 10^9 interactions per second. The data size of a typical raw event is approximate 1 MB. With current computer technology, recording such a huge amount of information can be challenging. In addition, the event rate is largely dominated by soft pp interactions with particles of low transverse momentum, which are not needed in the physics analysis. The CMS experiment uses a two-level online trigger system, a Level-1 Trigger (L1) and a High Level Trigger (HLT), aiming to keep events of interest while reducing the data rate to about 100 Hz due to limited storage and computing capacity.

3.2.7.1 The Level-1 trigger

The Level-1 trigger [41] reduces the rate of selected events to 50 (100) kHz for the low (high) luminosity running. The full data are stored in pipelines of processing elements, waiting for the trigger decision. The L1 makes the decision whether to keep or discard the data from a particular bunch crossing in 3.2 μs. If the L1 accepts the event, the data then will be transfered to the processing of the HLT, the next trigger

level. To deal with the high bunch crossing rate, the L1 trigger has to take a decision in too short a period of time to process the data from the whole detector, so it employs the calorimetric and muon information only. The tracker algorithm is not fast enough to meet the purpose. The process of L1 trigger has three steps (Figure. 3.11): a Calorimeter Trigger, a Muon Trigger, and the Global Trigger (GT), which makes the accept-reject decision based on the information collected from the previous two steps.

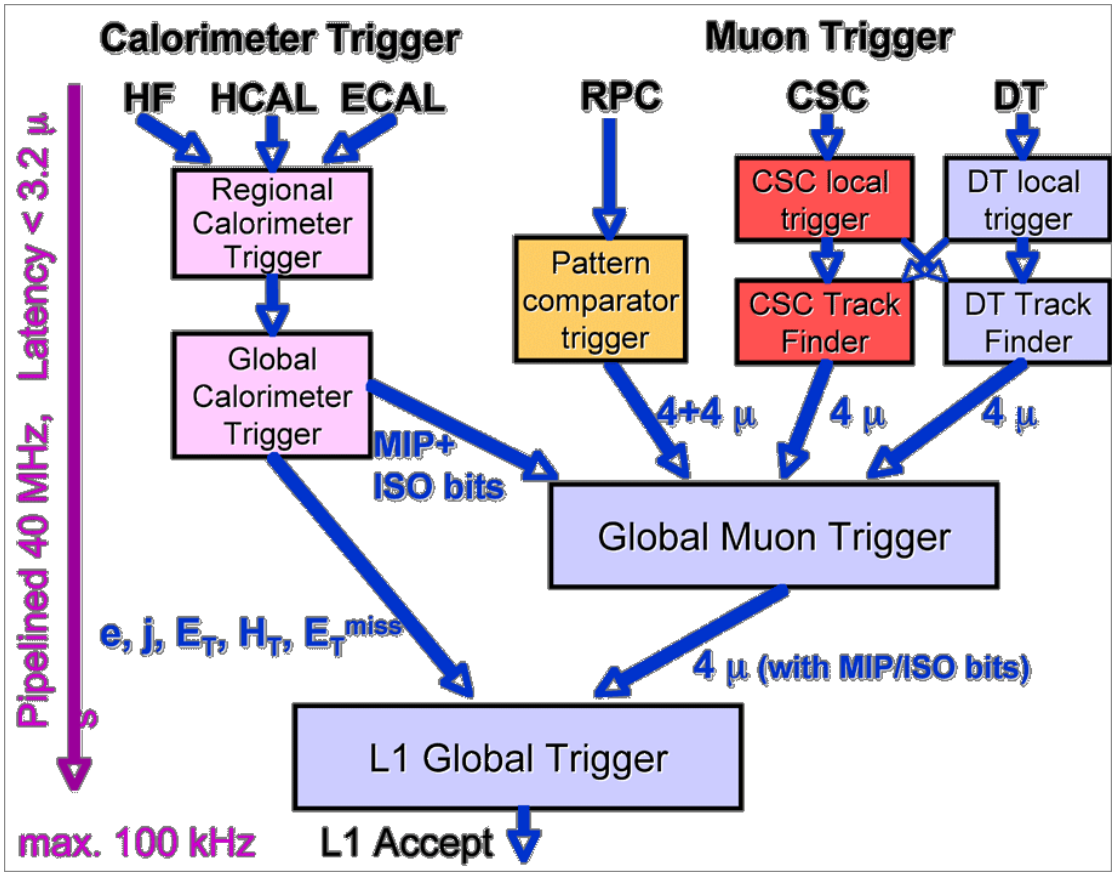

Figure 3.11: Architecture of the Level-1 (L1) Trigger [3].

The Calorimeter Trigger is based on trigger towers, the 5×5 matrices of the ECAL crystals, which matches to the granularity of the HCAL towers. The trigger towers are grouped in calorimetric regions of 4×4 trigger towers. The Calorimeter

Trigger identifies, based on the information collected from the calorimetric region, the best four candidates of each of the following classes: electrons and photons, central jets, forward jets and τ-jets identified from the shape of the deposited energy. The Muon Trigger is performed separately for each muon detector, using a similar procedure, to reconstruct and rank the muon objects above certain E_T or p_T thresholds.

After that, the Global Calorimeter Trigger (GCT) and Global Muon Trigger (GMT) select the highest-ranking calorimeter and muon trigger objects. Then, the four best candidates, together with the measured total and missing transverse energy, as well as the jet multiplicity above certain E_T or p_T thresholds from the GCT, will be transferred into the GT. The Global Trigger takes the accept-reject decision using information as both the characteristic of the single objects and of the combination of them.

3.2.7.2 The High Level Trigger

The HLT [42] is used to perform more sophisticated calculations and reduce the output rate. The HLT trigger software performs the regional reconstruction, which means only those objects in the useful regions are reconstructed. This leads to the development of three virtual trigger levels: at the first level only the full information of the muon system and of the calorimetry is used, in the second level the information from the tracker pixels is added and in the third and final level the full event information is available. The HLT can filter events according to several desired physics criteria and reduces the event rate from the L1 trigger by a factor of 10^3 to about 100 Hz.

3.2.8 CMS software components

The goals of the CMS software are to process end-selected events inside the HLT farm, to deliver the processed results to the experimenters within the CMS collaboration, and eventually to provide tools to analyze the processed information for physics results. The overall collection of software, now referred to as CMSSW [43], has an Event Data Model (EDM) [44] needed by the simulation, calibration and alignment and reconstruction models that process event data. The primary goal of the CMS Framework, which represents the code base of CMSSW and follows the bus model to execute modularized pieces of functionality, and Event Data Model (EDM) is to facilitate the development and deployment of reconstruction, and analysis software. The EDM is centered around the Event. It contains all data that were taken during a triggered physics event as well as all data derived from the data taking (e.g. calibration and alignment constants).

The physics and utility modules are written by detector groups and physics groups, such as the tracking group for charged particle track reconstruction and the E/γ group for photons, electrons and photon conversion reconstruction. The modules can be plugged into the CMSSW framework at run time, independently of the computing environment. The software is developed keeping in mind not only performance but also modularity, flexibility, maintainability, quality assurance and documentation. CMS has adopted an object-oriented development methodology, based primarily on the C++ programming language.

Chapter 4

Data Handling, Event Reconstruction and Monte Carlo Simulation

This chapter focuses on the following three topics: a brief review of data taking and handling, the outline of the object reconstruction in the relevant analysis, and the Monte Carlo simulation.

4.1 Data Taking and Handling

The CMS has a smooth operation of the data processing workflows from the detector to the end user analysis. It consists of

- online data taking
- high-level trigger chain
- offline reconstruction software

In this section, we discuss the online data taking and the high-level trigger chain. The event reconstruction is discussed separately in the next section.

4.1.1 Online Data Taking

The CMS trigger and data acquisition (DAQ) system is designed to collect and analyze the detector information at the LHC bunch-crossing frequency of 40 MHz. The first-level trigger (L1) is designed to reduce the incoming data rate to a maximum of 100 kHz, by processing fast trigger information coming from the calorimeters and the muon chambers and selecting events with some interesting signatures. The DAQ system must sustain a maximum input rate of 100 kHz, corresponding to a data flow of about 100 GB/s, from approximately 650 data sources from the different detector components. The DAQ system then reduces this rate by a factor of 1000 using a high-level trigger (HLT), a software filtering system running on a large processor farm.

4.1.2 High Level Trigger

The CMS high-level trigger algorithms are performed in a farm of computing nodes (the event filter farm) at CERN executing the HLT reconstruction and selection algorithm sequence in parallel. The HLT uses "menus" to specify the reconstruction and selection algorithms. An HLT menu consists of a set of trigger paths, each consisting of a sequence of reconstruction and selection modules. Each path is normally designed to select a specific physics signature (e.g. photon events).

Events accepted by the HLT are delivered to the storage manager system (SM) via the same network used for the event building. After that, the event data are stored into files in the SM by the definition of the output streams, which group events selected by specific HLT paths, e.g. primary "physics" stream, express stream, calibration

streams, etc. Within a stream, sets of paths selecting similar signatures (e.g. "photons", etc.) can be further grouped into primary datasets (PDs), defined as a subset of the stream consisting of the events satisfying a certain group of paths selected by that stream.

4.1.3 Data Handling Workflows and the Grid

The CMS computing system exploits a distributed infrastructure of Grid resources, services and toolkits, to satisfy the computing requirements for storage, processing, and analysis. It is based on building blocks provided by the Worldwide LHC Computing Grid project [45]. The worldwide distributed computing centers available in CMS are configured in a tiered architecture:

- The Tier-0 hosts the initial processing of data coming from the detector. It has about 20% of all computing resources available to CMS.
- The Tier-1 level takes care of subsequent processing and re-processing workflows. It has approximately 40% of the CMS computing resources available.
- The Tier-2 level hosts Monte Carlo (MC) simulation and analysis. It uses the remaining approximately 40% of all CMS computing resources.
- The Tier-3 level is located at individual universities and institutes for physics analysis purposes. The computing resources of Tier-3 are not counted in the overall Grid resources.

All streams defined by the online data taking system and the HLT are stored in a binary data format at Tier-0. A transfer system copies these files from the online systems at the detector site to the main CERN computing center. The system then

converts these files to a ROOT-based event data format (EDM) [44], splits them into PDs and stores them on tape. A first reconstruction is performed on these PDs and its output is stored in separate datasets.

The PDs are distributed to Tier-1 sites available to CMS for custodial storage and further processing. There are seven Tier-1 sites: France (T1_FR_IN2P3), Germany (T1_DE_FZK), Italy (T1_IT_CNAF), Spain (T1_ES_PIC), Taiwan (T1_TW_ASGC), the United Kingdom (T1_UK_RAL), and the United States (T1_US_FNAL).

Afterwards datasets stored at the Tier-1 sites are served to Tier-2 centers, where the final analysis to extract physics results is performed.

4.1.4 Data Sample

The data sample used in this analysis was collected with the CMS detector in the early 2011. During this period of time, the LHC operated at a center-of-mass energy of 7 TeV. The experimental signature in this thesis consists of photons, jets and missing transverse energy. Therefore, we are only interested in the PD that contains data samples with at least one photon, i.e., the "photon" PD. The following datasets are used in CMSSW_4_2_3. At least one photon is required in these datasets.

- `/Photon/Run2011A-May10ReReco-v1/AOD` (Run 160404-163869)
- `/Photon/Run2011A-PromptReco-v4/AOD` (Run 165088-167913)
- `/Photon/Run2011A-05Aug2011-v1/AOD` (Run 170249-172619)
- `/Photon/Run2011A-PromptReco-v6/AOD` (Run 172620-173692)

The combined integrated luminosity is 2.1 fb^{-1}. The uncertainty due to the measurement of the total integrated luminosity is about 4.5% [37].

4.2 Analysis Object Reconstruction

In this section, the relevant analysis objects are described. The reconstruction starts with the basic objects such as tracks, vertices and energy clusters, based on which higher level physics analysis objects are built, such as muons, electrons, jets and the missing transverse energy. The photon conversion reconstruction is discussed in the next chapter. For more technical details, one can review the published Technical Design Report for CMS [3].

4.2.1 Track Reconstruction

One of the key features of the CMS software is the reconstruction of particle trajectories with accurate position and momentum measurements, refer to as "track reconstruction" or "tracking." The track reconstruction consists of several steps:

- local reconstruction,
- seed finding,
- trajectory building,
- final track fit.

4.2.1.1 Process of Tracking

- **Local Reconstruction** The track reconstruction uses the experimental raw data of electronic signals, the "digis," deposited by charged particles traversing the tracking detectors. The digis consist of clustering adjacent pixel or strip digis. They are taken as the input to the local reconstruction to give the reconstructed "hit" positions with uncertainties.

- **Seed Finding** The starting point of a track (the "seed") is formed from either a triplet of hits in the tracker or a pair of hits with an additional constraint from the beamspot or a pixel vertex. It provides an initial estimate of the trajectory and its uncertainty.

- **Trajectory Building** The seed propagates outward in a search for the compatible hits ("inside-out"). Compatible hits are found, and added to the trajectory, then the track parameters and their uncertainties are updated. This search will continue until either no more compatible hits are found or the trajectory reaches the boundary of the tracker. An additional search is performed starting from the outermost hits and then propagates inward ("outside-in"). In case two tracks share a significant number of hits, the one with fewer hits is discarded to prevent double counting.

- **Final Track Fit** In the final step, the collection of hits is fit to obtain the best estimate of the track parameters with accurate position and momentum measurements [46].

4.2.1.2 Iterative Tracking

The tracking software in CMS is a series of combined algorithms, called "iterative tracking." Each iteration uses a unique seeding method. It follows the pattern recognition and the final track fit steps as mentioned before. After each iteration, the hits assigned to this iteration are excluded from further iterations.

The first tracking iteration is dedicated to find tracks which originate near the primary vertex because these are easiest to reconstruct. It seeds the tracks with pairs or triplets of hits from the pixel tracker, which provides high resolution 3D position

measurements. It then extrapolates these seeds outwards and assigns to the track additional hits from the pixel or the strip trackers using the Kalman filter algorithm [47]. Hits assigned to these tracks are excluded from further searches, which simplifies the task for the subsequent iterations. Five iterations are used in total. Some of the additional iterations are dedicated to the reconstruction of very low momentum tracks, in the mean time, the others are dedicated to find highly displaced tracks. The reconstruction of very displaced tracks uses seeds produced from the hits in pairs of the strip tracker stereo layers. Then similar procedures of the pattern recognition step and the final track fit step are performed.

4.2.2 Jet Reconstruction

The quarks and gluons from the pp collisions cannot be observed individually due to color confinement in QCD. They fragment into final state particles through the spontaneous creation of quark-antiquark pairs, the "hadronization" or the "fragmentation." As a result, there are bunches of hadrons, the "jets," which are collimated in the same direction as the initial partons. Most of the jet reconstruction algorithms exploit a clustering technique in which the energy deposits close to a high E_T "seed" tower are summed together to form a jet.

There are three major types of jet reconstruction algorithms in CMSSW using the anti-k_T clustering algorithm [48] with a cone size parameter $\Delta R = 0.5$:

- **Calo jets [49]:** Calo jets are reconstructed using only the calorimeter information.
- **Jet-plus-track (JPT) jets [50]:** JPT jets include the momenta of the associated charged particles. This algorithm improves the p_T response and the resolution of Calo jets.

- **Particle-flow (PF) jets [51]:** PF jets include a list of particles from all the CMS subdetectors in the particle flow method.

4.2.3 Missing Transverse Energy

Some physics processes have one or more weakly interacting particles (e.g. neutrinos) that escape from the detector without leaving a trace. This gives an apparent imbalance of the measured transverse momentum, referred to as the missing transverse momentum ($\overrightarrow{E_T^{miss}}$), and its magnitude as the missing transverse energy (E_T^{miss}) [76].

$\overrightarrow{E_T^{miss}}$ is calculated in terms of

$$\overrightarrow{E_T^{miss}} = -\sum_i (E_i \sin\theta_i \cos\phi_i \hat{x} + E_i \sin\theta_i \sin\phi_i \hat{y}) \tag{4.1}$$

where the index i covers all the input objects of the algorithm, e.g. the energy deposit in the calorimeter towers for $E_{T\ calo}^{miss}$ and the reconstructed particles in the particle flow method for $E_{T\ PF}^{miss}$.

4.2.4 Electron Reconstruction

The electron reconstruction follows a three-step workflow similar to the track reconstruction: seed finding, trajectory building and final track fit.

- **Seed Finding** When an electron travels through the CMS detector, it leaves a track in the CMS tracker, as well as an electromagnetic cascade (shower) as bremsstrahlung in the ECAL. The seeding algorithm starts with the reconstruction of ECAL "superclusters," which is a collection of the ECAL clusters extended in ϕ. It then matches the supercluster with the electron track seeds (pairs or triplets of hits) in the inner tracker layers and builds electron trajectories from these track seeds.

- **Trajectory Building** In the trajectory building step, the normal track reconstruction uses the Kalman filter algorithm. However, the electron tracks have bremsstrahlung and energy loss, which leads to an non-Gaussian distribution of the measurement errors and invalidates the Kalman filter [47]. Therefore, the electron track reconstruction uses a Bethe Heitler modeling [52] of the electron losses and a Gaussian Sum Filter (GSF) [53] in the trajectory building. In the GSF filter, the distribution of the track parameters is a mixture of Gaussians [54]

$$f(x) = \sum_{i=1}^{n} p_i \phi(x; \mu_i, V_i), \;\; \sum_{i=1}^{n} p_i = 1 \tag{4.2}$$

  and is implemented by parallel Kalman filters. If the predicted density $f(x)$ has n components, and measurement density has m components, the updated density has $m \times n$ components. For electron tracks in the CMS detector, the energy loss distribution is approximated by a mixture of six Gaussians for a fast implementation.

- **Final Track Fit** In the final step, the collection of hits is fit to obtain the best estimate of the track parameters with accurate position and momentum measurements. The electron energy is deduced from a weighted combination of the corrected supercluster energy and tracker momentum measurements.

4.2.5 Photon Reconstruction

Photon showers deposit their energy in several crystals in the ECAL. A collection of adjacent ECAL crystals, which is used to reconstruct the energy and the direction of a particle, is commonly referred to as cluster. Approximately 94% of the incident energy of a single photon is contained in a 3×3 cluster and 97% in a 5×5 cluster. By summing and measuring the energy in the clusters, we can achieve the best

reconstruction performance for photons.

However, the presence of material in front of the calorimeter results in bremsstrahlung and photon conversions. Furthermore, because of the strong magnetic field, the energy of photons reaching the calorimeter is spread in the ϕ direction. Due to these effects, in order to recover the entire energy of the incoming photon, a dynamic cluster algorithm is a must. So far, there are many different cluster algorithms [55] being used in the CMSSW framework. According to the analysis in this thesis, the Hybrid algorithm, using only the ECAL barrel photons, is the one to be discussed in the following context.

4.2.5.1 Hybrid algorithm

The Hybrid algorithm uses the $\eta - \phi$ geometry of the barrel crystals to exploit the knowledge of the ECAL shower shape in the η direction, while dynamically searching for the energy in the ϕ direction. The basic principles of the Hybrid algorithm are shown in Figure 4.1.

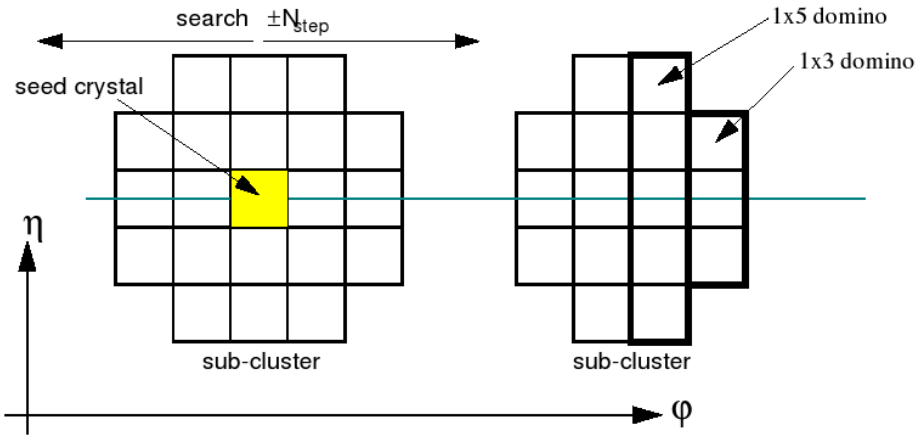

Figure 4.1: Illustration of Hybrid algorithm

Starting from a crystal with transverse energy $E_T > E_T^{hyb}$, $1_\phi \times 3_\eta$ crystal

dominoes are made, each with the central crystal aligned in η with the seed crystal, which has the highest energy deposit (colored in yellow in Figure 4.1). If the energy of the central crystal of a domino exceeds a certain threshold E_{wing}, a 1×5 domino (instead of a 1×3) is used. The same procedure is repeated N_{step} times, in both the ϕ directions from the original seed. Once the $\eta-\phi$ scan is finished, dominoes with $E < E_{th}$ are removed and the cluster is reconstructed. To distinguish a new disconnected subcluster, a central domino with $E > E_{seed}$ is required. The parameter values used in the standard reconstruction procedure are listed in Table 4.1:

Parameter	Value
E_T^{hyb}	1 GeV
N_{step}	10
E_{wing}	1 GeV
E_{th}	0.1 GeV
E_{seed}	0.35 GeV

Table 4.1: Parameter values for supercluster reconstruction

When all the clusters in the event have been reconstructed, a so-called supercluster is formed by the group of these clusters under specific rules. The most energetic cluster is identified as associated with the other clusters inside a fixed $\eta-\phi$ region. The search region is much larger along ϕ than that in η, because the ϕ direction is along the direction in which all the charged particles inside the electromagnetic shower are bent, due to the effect of the magnetic field. A schematic view of the supercluster reconstruction algorithm is shown in Figure 4.2.

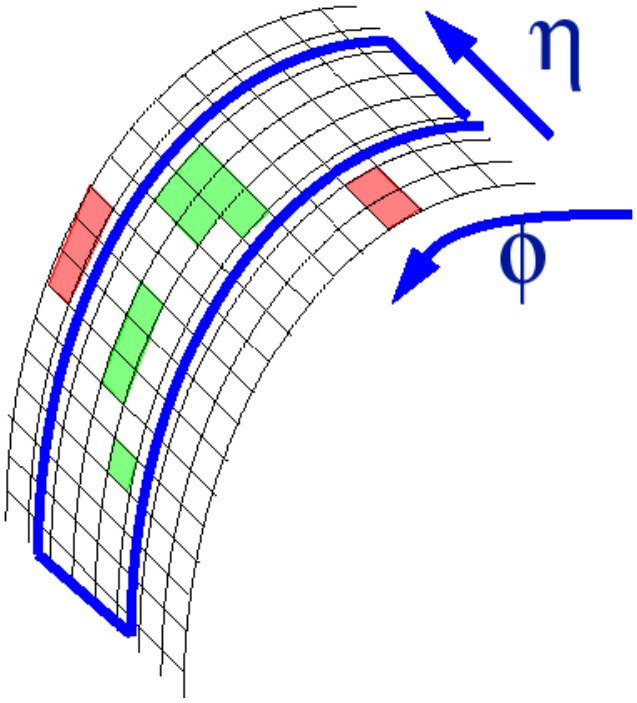

Figure 4.2: Supercluster reconstruction algorithm.

4.2.5.2 Energy corrections

The simplest way to reconstruct the total energy of a photon is to sum up the contributions from all the crystals that form a cluster. However, corrections must be made for the different sources of variations in the clustered energy, which are listed below:

- The fraction of energy in a fixed array varies as a result of the shower position with respect to the cluster boundary;
- Large losses due to rear leakage for showers close to the barrel inter-module and inter-supermodule borders, due to the cracks containing negligible material, causing a considerable reduction of the effective depth of the ECAL;
- The spread of energy due to showering in the tracker material and the performance

of the supercluster algorithms;

- e^+e^- track pairs for photon conversions.

The overall impact of these effects on the reconstructed energy can be estimated with high accuracy, with simple corrections applied during the reconstruction step.

4.2.5.3 Position measurement

The measurement of the shower position [55] can be obtained by calculating the energy-weighted mean position of the crystals in the cluster. Because of the quasi-projective geometry of the ECAL, the lateral position of the crystal axis depends on the depth, which can be parametrized as $A[B + log(E))]$, where E represents the energy and A, B are the two parameters depending on the nature of the incoming particles.

Since the energy density decreases almost exponentially with the lateral distance from the shower core, an unbiased estimate of cluster position can be obtained by taking a weighted mean using the logarithm of the crystal energy[56]:

$$x = \frac{\sum x_i \cdot W_i}{\sum W_i} \tag{4.3}$$

where x_i is the position of i-th crystal and W_i is the logarithmic weight defined as:

$$W_i = \max[\mathrm{W_0} + \log(\frac{\mathrm{E_i}}{\sum \mathrm{E_j}}); 0] \tag{4.4}$$

4.2.5.4 Photon Isolation

In order to maintain the purity of the photon signal selections, the photons are required to be isolated with no electromagnetic or hadronic activity (as specified below)

within a radius $\Delta R = \sqrt{(\Delta\eta)^2 + (\Delta\phi)^2} = 0.4$ of the photon. There are three isolation algorithms by the subdetectors:

- **ECAL isolation:** ECAL recHits are summed in a cone centered on the the electron or photon ECAL supercluster, with a footprint removal region to remove electrons consisting of a strip of specified η width and an additional circular region (i.e. inner veto cone).

- **Track isolation:** The p_T of the tracks is summed in a cone centered on the electron or photon ECAL supercluster, with a footprint removal region to remove electron as in the ECAL isolation. The track isolation cone differs from the ECAL isolation cone by the width of the η strip (0.03) and the radius of the central hole (0.04), optimized to exclude reconstructed tracks in $Z \to ee$ events.

- **HCAL isolation:** CaloTower HCAL sections are summed in a cone centered on the electron or photon ECAL supercluster position, with an inner footprint removal region of radius 0.15.

The isolation cones used in this analysis are shown in Figure 4.3 [57].

- ECAL E_T in the ECAL isolation cone $< 0.006 \cdot E_T + 4.2$ GeV;

- HCAL E_T in HCAL isolation cone $< 0.0025 \cdot E_T + 2.2$ GeV;

- $H/E < 0.05$;

- E_T of the tracks in the track isolation cone $< 0.001 \cdot E_T + 2.0$ GeV;

- $\sigma_{i\eta i\eta} < 0.011$;

where H/E is the ratio of hadronic energy in the tower directly behind the ECAL supercluster divided by its energy. The H/E ratio is determined by the E_T in the ECAL

and HCAL cones shown in Figure 4.3. $\sigma_{i\eta i\eta}$ is the log energy weighed width (σ) of the extent of the shower in the η dimension based on the core 5x5 matrix of crystals of the supercluster.

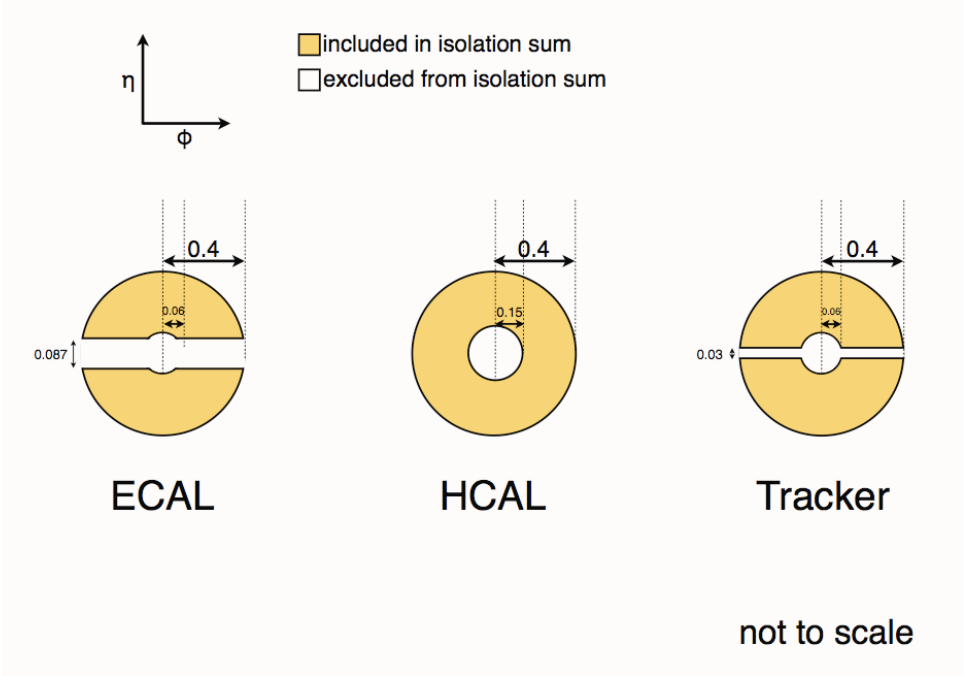

Figure 4.3: Sketch illustrating the isolation cones for the ECAL and HCAL E_T deposits [4].

4.3 Monte Carlo Simulation

Monte Carlo methods are a collection of well developed mathematical techniques which solves a problem by generating suitable random numbers and observing that fraction of the numbers obeying some property or properties [58]. The simulation for the CMS physics studies involves two main steps. First, the "event generation" simulates the physics process of interest using a dedicated Monte Carlo approach to generate the random inputs, e.g. the flavor and kinematic information about the initial partons involved in the hard scattering, using a random number generator. It then calculates

the probability of certain physics outcomes, using a specific theory model over the domain of possible inputs and provides kinematic information for the final state particles. The generated events are then weighted according to various probability distribution functions involved in this method. Second, the "detector simulation" models how these final state particles travel through the detector and leave the distinguishable signatures, using the similar Monte Carlo methods.

4.3.1 Event Generation

High energy physics event generation can be performed typically following these four steps:

- **Matrix Element calculation**: The matrix element calculation involves the leading order of the tree level Feynman diagrams of the parton-parton hard scattering; the momenta, the spins and the color connections of the final state partons (quarks, gluons, leptons and photons) are assigned based on the expected distributions from the theory.

- **Parton Shower**: The parton shower formulation is used to connect the final state partons and the experimental observables, such as mesons, baryons, leptons and photons.

- **Underlying Event modeling**: The underlying events, which consist of the "beam remnants" and the particles arising from the soft or the semi-soft multiple parton interactions, are modeled by the generator as well.

- **Hadronization**: The process by which partons evolve to produce hadrons is referred to as hadronization or fragmentation, which cannot be calculated using

perturbative QCD. Instead, several hadronization models are available as alternatives to describe such processes.

There are many software packages available in the high energy physics community for Monte Carlo simulation. In this thesis, PYTHIA [59] is used to generate the signal datasets. It is a multi-purpose Leading Order (LO) generator which can calculate the hard scattering process using the tree level Feynman diagrams. It is fully equipped with the functionalities such as the parton shower packages, the underlying event modeling packages and the hadronization packages. The main hadronization option in PYTHIA is the "Lund" string scheme [60], which involves the stretching of a color "string" across the quarks and the gluons, and then breaking it into the final state hadrons.

There are also other software packages, such as ALPGEN [61] and MADGRAPH [62] for other purposes.

4.3.2 Detector Simulation

The CMS detector simulation is based on GEANT4 [63]. It is fully integrated within the CMSSW framework. It describes the detector geometry and materials and uses the information about the magnetic field. It also simulates the detector response, the effects of energy loss, and the multiple scattering and the showering in the detector materials when the generated particles traverse the CMS detector.

Chapter 5

The Reconstruction of Photon Conversions

This chapter gives a detailed description of the photon conversion reconstruction methods.

5.1 Photon Conversion Reconstruction

The CMS tracker based on silicon technology is designed to provide robust and precise reconstruction of charged-particle momenta in the high occupancy environment of LHC collisions, with an inevitably substantial amount of Tracker material. The direct consequence is that a large fraction of photons convert into e^+e^- pairs while traversing the Tracker material (known as the "photon conversions").

Reconstructing the conversion electron pair assumes special relevance in many applications, ranging from the determination of the Tracker material to physics discovery channels. Specifically, these applications range from the reconstruction of very low energy photons produced in Minimum Bias events (non-diffractive events, with no bias

from restricted trigger conditions), to the reconstruction of high-energy photons that can arise from the decay of the Higgs boson or supersymmetric particles. A robust method for reconstructing high-energy converted photons using the ECAL for trajectory seed finding has already existed [64] for many years. However, thanks to the recent developments in the field of tracker-only seeding methods and iterative tracking, the capability of conversion reconstruction has been greatly improved, which makes it possible to search for conversions of very low transverse energy, instead of only for isolated photons. The combination of all conversion reconstruction algorithms is also discussed in the following context.

5.2 Strategy of Conversion Reconstruction

The basic idea of tracker-seeded conversion reconstruction is to find conversion track pairs in the tracking system using the conversion signatures.

With the iterative tracking, track candidates are formed using seed hits in the Pixel Tracker layers and the Silicon Strip Tracker double-sided layers, using the Kalman Filter method. Every seed is extrapolated to the neighboring tracker layers, whose trajectory is updated with compatible hits found in these layers, assuming consistency with the hypothesis of a particle with p_T exceeding a specified value and originating near the detector origin to within a specified distance. After track building, several track candidates are typically produced from each seed. Track trajectories are then fitted using the Kalman Filter. In the first iteration all reconstructed hits are used. The hits associated with the tracks which satisfy the tightest requirements are locked. Further iterations then use less restrictive requirements applied only to the remaining hits.

After that track cleaning is performed to cancel the fake tracks. In this way tracks with very low p_T and large impact parameter can be reconstructed with a low level of fake tracks [65].

The goal of the tracker-seeded conversion finding algorithm is to provide a conversion selection method which is independent of the ECAL. In this way, it is possible to reconstruct soft conversions which do not even reach the calorimeter, while on the other hand providing a sample of conversions that can be matched with the ECAL "a posteriori", e.g. to perform studies on ECAL-based electron identification variables.

The conversion finder we implemented is very straight-forward: it takes default track collections from the tracking system as the input, applies some track quality criteria, focuses on opposite-charge track pairs, and then finally it exploits the kinematic mechanism of a conversion pair to disentangle genuine from fake pairs. Overall, the default selection we implemented in the finder (it is however fully configurable) aims at achieving the largest possible efficiency while maintaining a reasonably high purity and the lowest p_T possible. Ultimately a conversion object is created (according to the data format available in CMSSW for this kind of object and shared by the ECAL-seeded conversions), which stores the momentum, the reconstructed conversion vertex, and the tracks and their parameters.

5.3 Signatures

Before going into details in this section, we define the quantities used to characterize a converted photon and discriminate between genuine electron-positron pairs and combinatoric background, e.g. from charged pions. The signature is mainly formed by the physical facts as followed:

- due to the zero mass of the photon, the electron tracks from a conversion are parallel at the production vertex, and they bend only in the transverse plane under the effect of the magnetic field;

- vertices can be very displaced because the photons can convert in the entire tracker volume;

5.3.1 Charge-signed impact parameter

Photon conversion vertices are displaced with respect to the beam spot since conversions may occur anywhere in the tracker. Therefore the electron tracks can have large transverse impact parameter (d_0) which is measured with respect to the best position measurement of the primary vertex as reconstructed from the Pixel triplets. Because e^+e^- track pairs lie on opposite sides with respect to the photon direction, the charge-signed impact parameter ($Q \cdot d_0$) of both tracks must be positive. For tracks from the interacting point of pp collisions (background tracks), instead, this quantity is symmetrically distributed around zero because these tracks are not associated with any photon conversion. The comparison of the $Q \cdot d_0$ distribution for genuine conversions and tracks from the background is shown in Figure 5.1.

5.3.2 Distance of Minimum Approach

Tracks evolving in the CMS magnetic field are in fact helices, projected as ring patterns in the transverse view. We consider the distance of minimum approach between the two e^+e^- tracks (two rings) in the transverse plane, defined as

$$d_m = d_{o1-o2} - (R_1 + R_2), \tag{5.1}$$

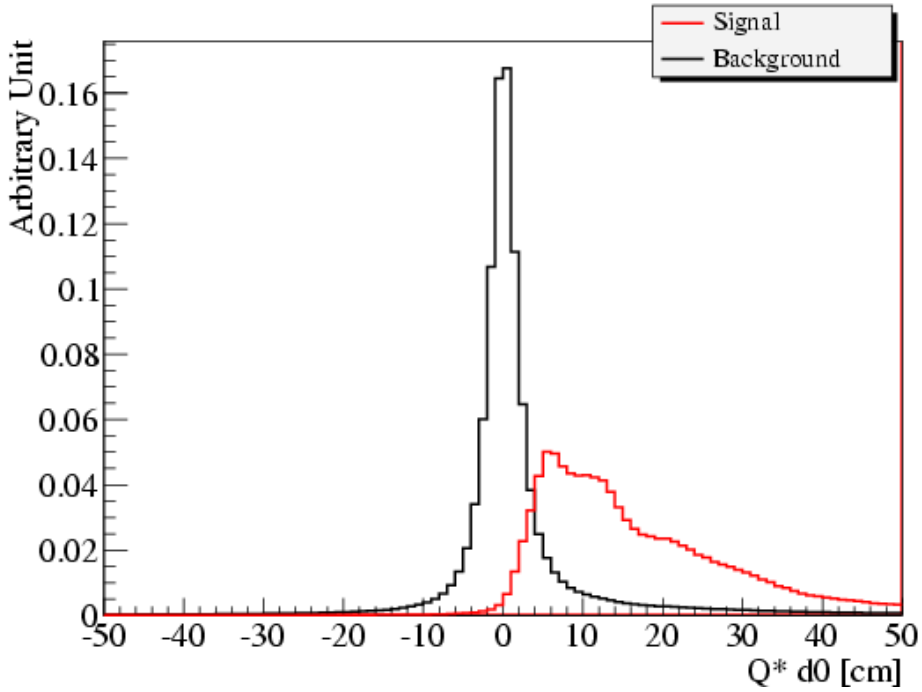

Figure 5.1: Charge-signed impact parameter for photon conversions compared with background tracks from QCD events. The Monte Carlo truth is checked to separate conversions from background.

where d_{o1-o2} is the distance between the centers of the two rings with R_1 and R_2 as their radii. The distance d_m is a negative value if the rings intersect(Figure 5.2 (a)), zero if the rings are tangent, and positive if they are disjoint (Figure 5.2 (b)). As described at the beginning of this section, for conversions we expect d_m to be ≥ 0, as observed for genuine conversions (Figure 5.3). For the background track combinations, instead, d_m is expected to be mostly negative as they come mainly from the interaction point. In this case, the track pairs (rings) necessarily share at least one point (the primary vertex within errors) and they can be at most tangent, but never disjoint.

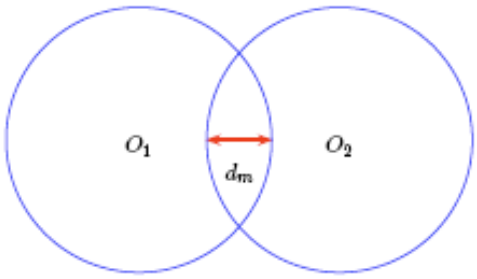

(a)

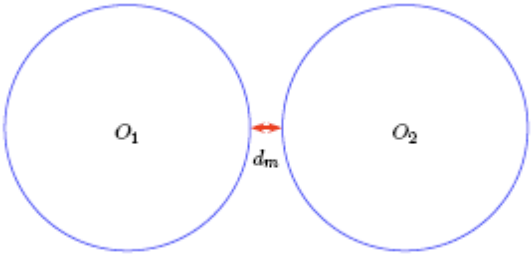

(b)

Figure 5.2: Minimal distance at the approaching point: (a) negative for intersecting rings, (b) zero or positive for disjoint rings.

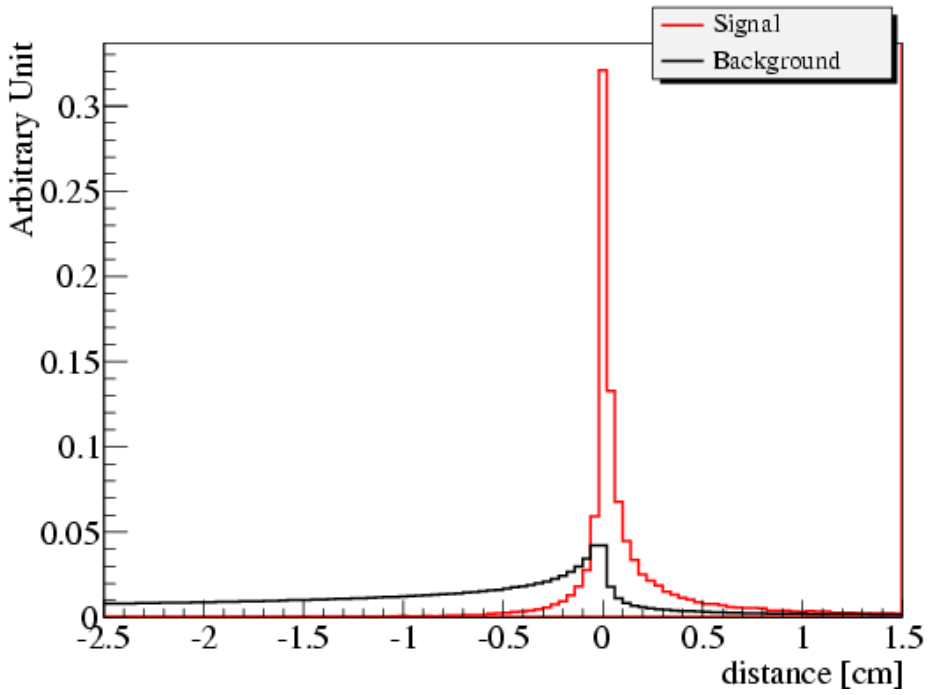

(a)

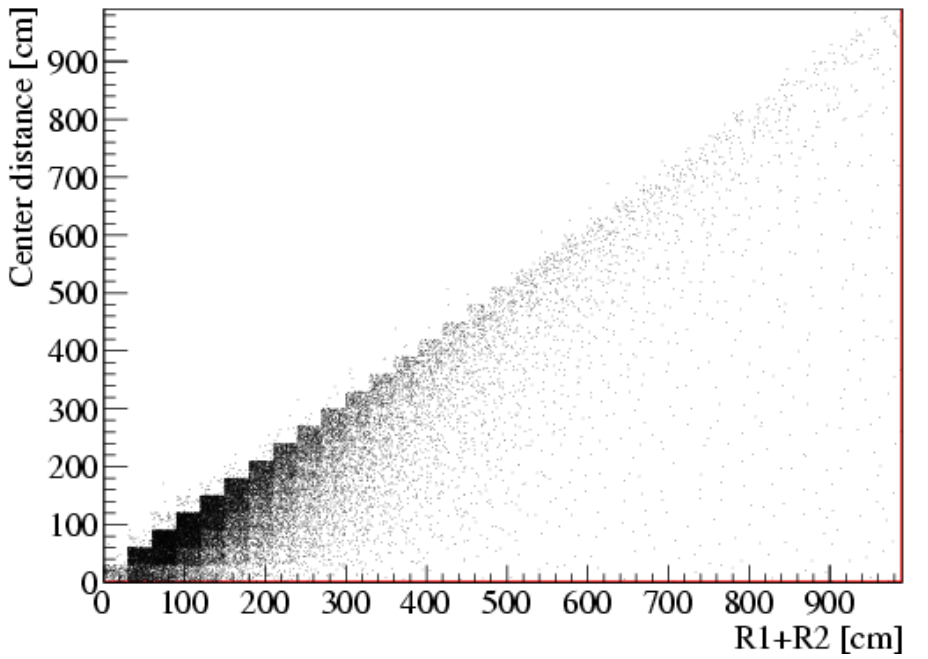

(b)

Figure 5.3: (a) Minimal distance at the approaching point; (b) Ring relations $d_m = d_{o1-o2} - (R_1 + R_2)$. Background tracks are from the collision interaction point.

5.3.3 Opening Angles

As mentioned earlier, electrons from conversions remain parallel in the longitudinal plane due to the photon masslessness, that is to say their opening angle, usually measured as $\Delta \cot \theta$, has a value close to zero. For background combination pairs, instead, the range of $\Delta \cot \theta$ is expected to be very broad. Ideally, $\Delta \cot \theta$ should be zero; however, the angle is affected by the precision of track reconstruction, which degrades for short tracks such as those reconstructed by the last step of the iterative tracking. The resolution for $\cot \theta$ for single tracks (about ± 0.02) is shown in Figure 5.4 (a), which leads to the track pair opening angle resolution of ± 0.04 with long tails (Fig 5.4 (b)) arising from the shortest tracks. The $\Delta \cot \theta$ distribution for the background sample is shown on the same plot.

5.3.4 Distance between the PCA and the interaction vertex

The radius of the point of closest approach (PCA) of conversion tracks measured with respect to the interaction point (R_{PCA}) gives a quick estimate of the conversion vertex position. The difference between R_{PCA} and the radius of the simulated conversion is shown in Figure 5.5. For genuine conversions R_{PCA} is always greater than about 2 cm from the interaction point (i.e. first conversions can only happen in the beam pipe located at a radius of 2.9 cm). The R_{PCA} distributions for both background and genuine conversions are shown in Figure 5.6 in the sample of QCD events with p_T between 30 and 50 GeV.

R_{PCA} is affected by the tracker alignment resolution. Thus, in the real collision data, the alignment resolution should be considered to avoid loss of signal. Practically,

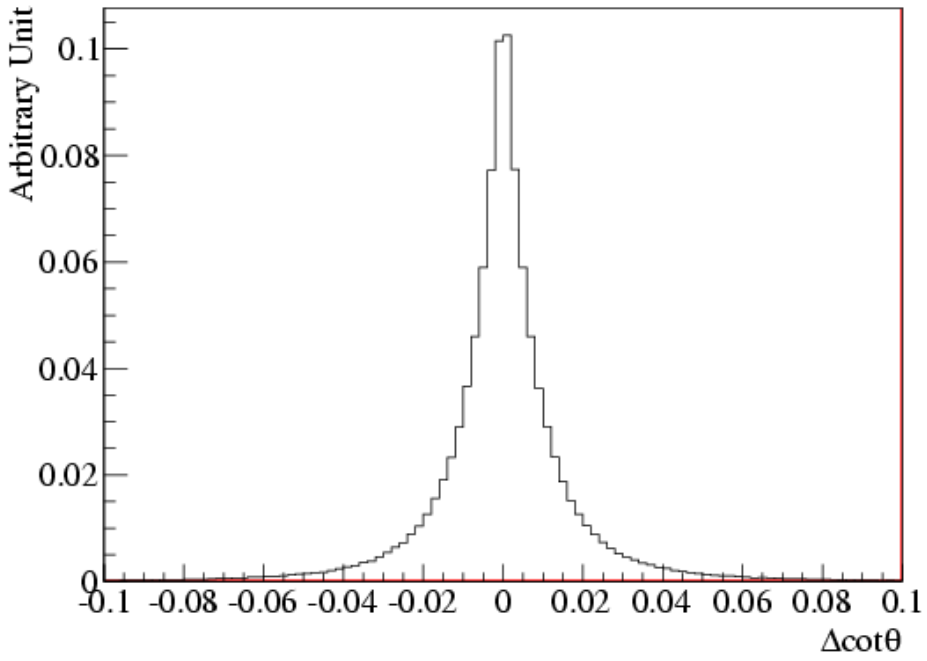

(a)

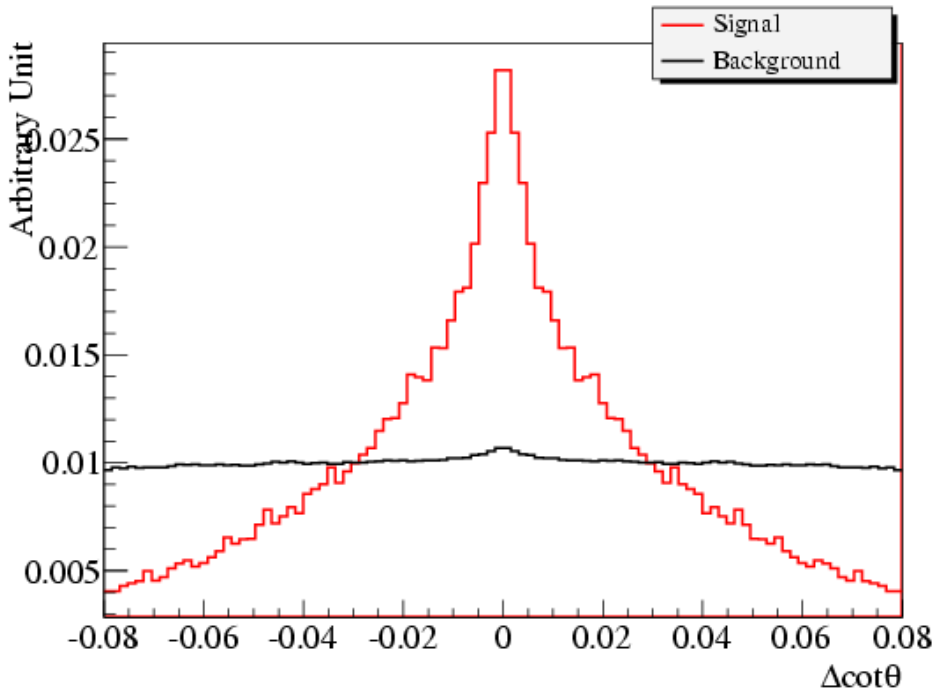

(b)

Figure 5.4: a) $\cot\theta$ resolution for single reconstructed tracks; b) Track pair $\Delta\cot\theta$.

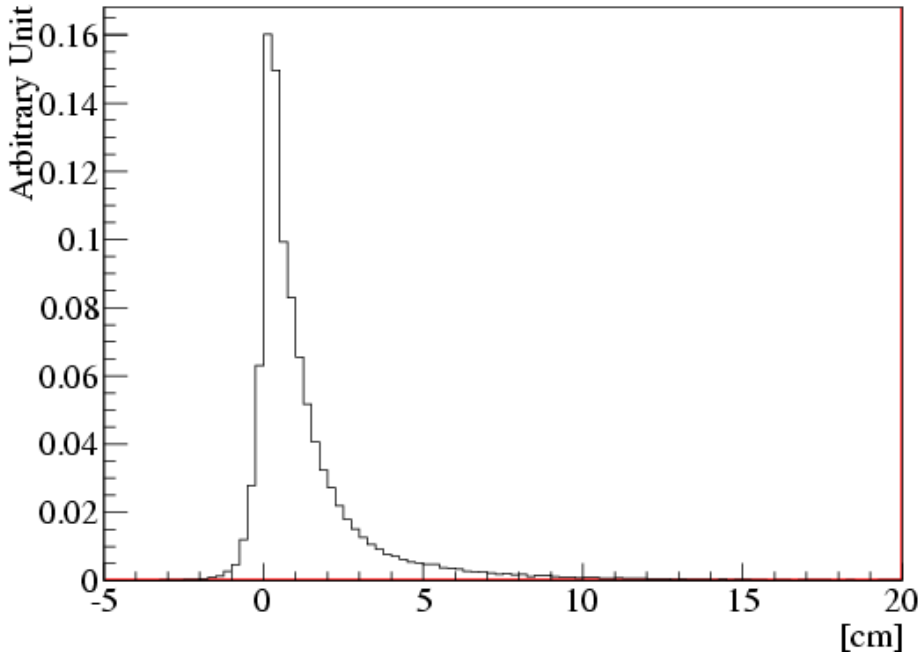

Figure 5.5: Difference between the radius of the PCA and the radius of the simulated conversion vertex.

R_{PCA} is set to 1 cm, in order to eliminate the random combinations of tracks from the interaction point.

5.3.5 Track-to-ECAL cluster matching

If electrons from conversions are energetic enough to reach the ECAL, the directions and momenta measured from the tracks should match the energy deposit. Conversion tracks are extrapolated to the ECAL cylinder and only the cluster closest to the track impact point is chosen. We can then measure the distance between the track impact point and the closest ECAL cluster we have chosen in the η-ϕ view, $\Delta\eta$ (Figure 5.7 (a)) $\Delta\phi$ (Figure 5.7 (b)), as well as the E/p matching (Figure 5.8).

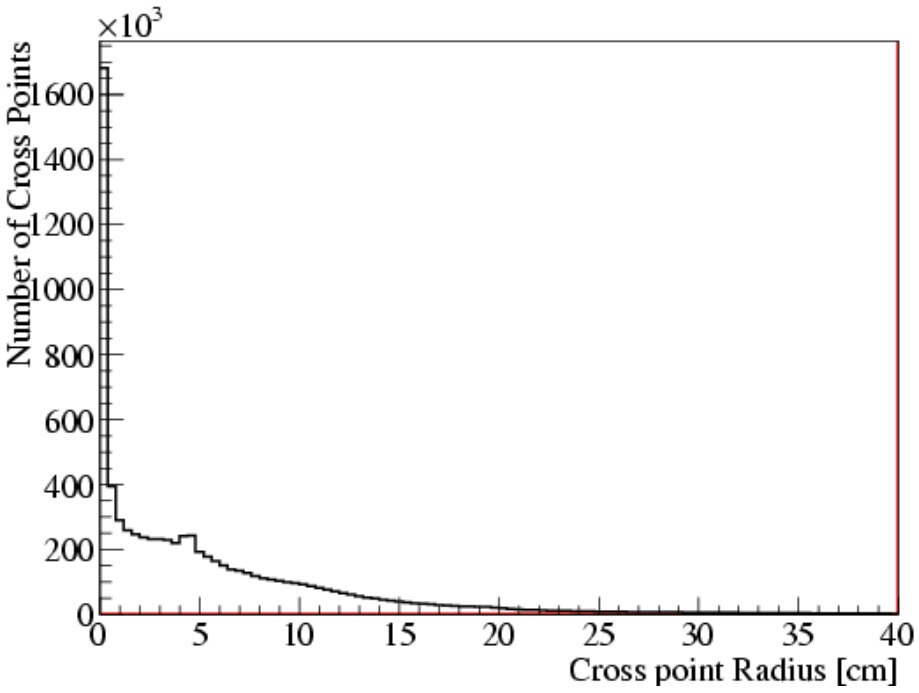

(a)

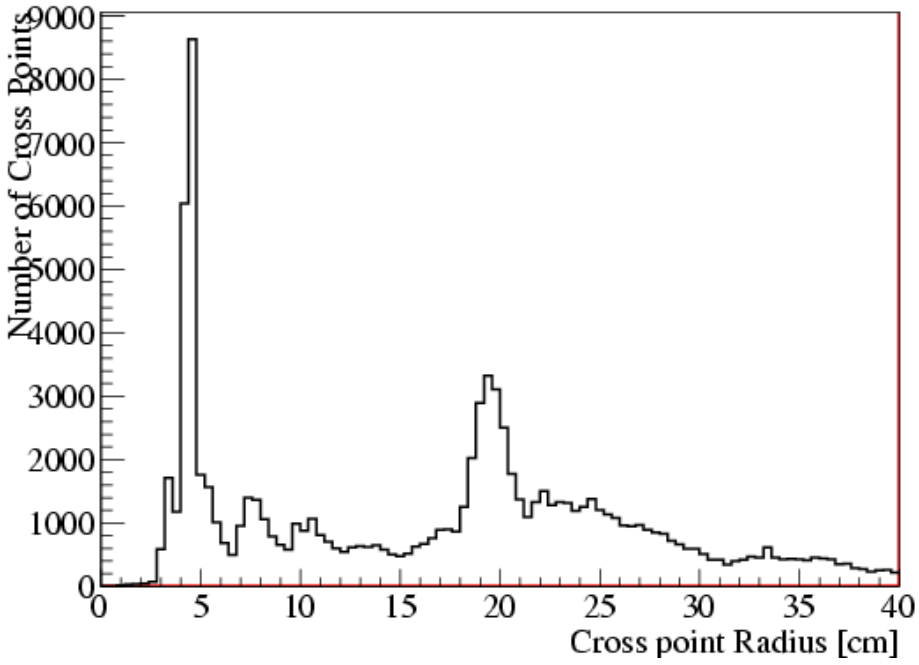

(b)

Figure 5.6: Distribution of the PCA cross point radius: (a) background track pairs in QCD events with p_T between 30 and 50 GeV; (b) genuine conversion track pairs in QCD events with p_T between 30 and 50 GeV.

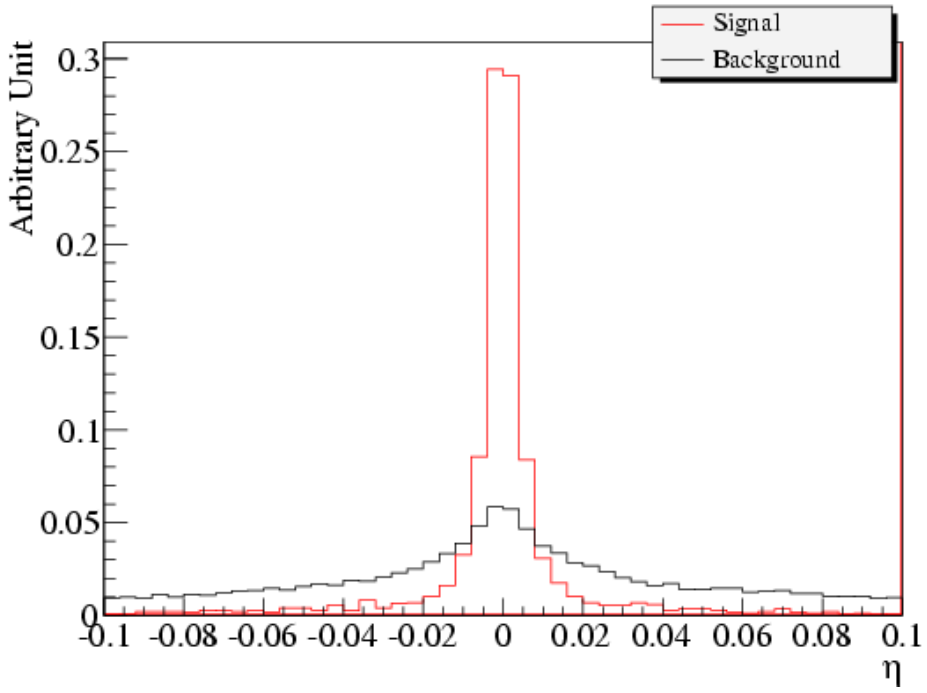

(a)

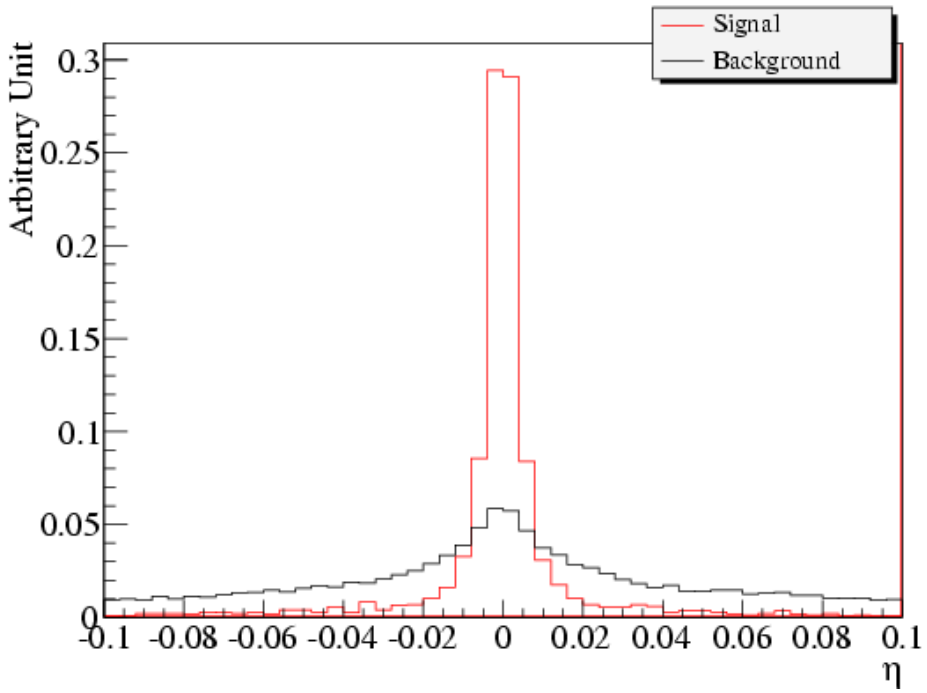

(b)

Figure 5.7: (a) Track-Cluster $\Delta\eta$; (b) Track-Cluster $\Delta\phi$.

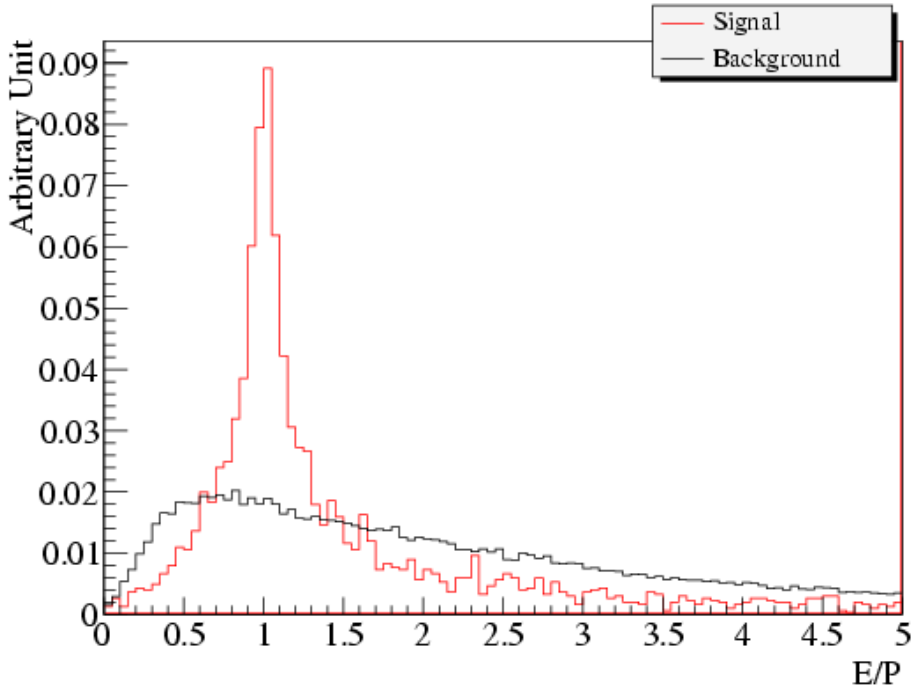

Figure 5.8: E/p: E is the energy of the ECAL basic cluster closest to the track impact point and p is the track momentum.

5.4 Conversion Selection Criteria

The default selection criteria are listed below:

- Two tracks with opposite charge;
- One of the tracks with at least 5 hits and the other track with at least 3 hits;
- Tracks charge-signed impact parameter, $Q \cdot d0 > 0$ cm ;
- Distance of minimum approach, $d_m > -0.25$ cm;
- Radius of the point of minimum approach, $R_{PCA} > 2.9$ cm;
- $\Delta\phi$ between tracks < 0.2 radians;
- $|\Delta \cot\theta| < 0.1$;

5.5 Vertex fitting

Once the conversion track pairs are selected, they are fitted to a common vertex in order to determine the conversion vertex position. We use a kinematic constrained vertex fitting library [66] available in CMSSW. This fitting algorithm requires two steps: a Kalman Vertex fit and a 3D geometrical constraint, imposing the two tracks to be parallel.

The basic idea of the constraint vertex fitting is to describe the kinematic system in terms of its Hamiltonians. For example, in the quasi-cartesian frame, the conversion vertex should have $H_\phi = 0$ and $H_\theta = 0$ due to the parallelism of the conversion tracks.

$$H_\phi = \frac{1 - \frac{dx}{\sqrt{dx^2+dy^2}}}{\frac{dy}{\sqrt{dx^2+dy^2}}} - \frac{1 - \frac{px}{\sqrt{px^2+py^2}}}{\frac{py}{\sqrt{px^2+py^2}}} = 0 \tag{5.2}$$

$$H_\theta = \frac{1 - \frac{\sqrt{dx^2+dy^2}}{\sqrt{dx^2+dy^2+dz^2}}}{\frac{dz}{\sqrt{dx^2+dy^2+dz^2}}} - \frac{1 - \frac{\sqrt{px^2+py^2}}{\sqrt{px^2+py^2+pz^2}}}{\frac{pz}{\sqrt{px^2+py^2+pz^2}}} = 0 \tag{5.3}$$

where $dx = x_s - x_p$, $dy = y_s - y_p$, $dz = z_s - z_p$. (x_s, y_s, z_s, p_x, p_y, p_z, m) is the parameter set of the particle at the secondary vertex (conversion vertex), (x_p, y_p, z_p) shows the position of the primary vertex and (d_x, d_y, d_z) is the vector pointing from the primary to the secondary vertex.

The fitting procedure is to converge the H_ϕ and H_θ to the minimum at the same time using Least Means Squared minimization (LMS) with Lagrange multipliers. The fitting algorithm performs an iterative procedure, and search in the phase space of (x, y, z , p_x, p_y, p_z, m) to converge the H_ϕ and H_θ to 0. If both H_ϕ and H_θ are converged to the minimum simultaneously, the fitting returns a valid vertex. Only the conversion candidate with a valid vertex is considered.

5.6 Conversion Merging and Duplication Removal

Three reconstruction algorithms are used in the CMS software: the "tracker-only" [46, 67], the "Gaussian Sum Filter" (GSF) electron [53], and the "ECAL-seeded" [64]. The tracker-only algorithm, known as the tracker-seeded algorithm, selects conversion track pairs from all reconstructed tracks under the kinematic constraint, and then fits the conversion vertex. The GSF electron algorithm follows a similar procedure to the tracker-only algorithm but uses GSF electrons (electron tracks reconstructed using Gaussian Sum Filter algorithm) to find conversion track pairs. The ECAL-seeded algorithm uses the energy deposit of conversion tracks in the ECAL as seeds and then extrapolates back to the tracker to fit the conversion tracks and the conversion vertices.

The conversions from these three algorithms are merged and the duplication is removed: in all duplicated conversion tracks from the three algorithms, the conversion track with the largest number of hits is kept only if its χ^2 probability is not significantly worse than the others (χ^2 probability should be greater than 10^{-6}); otherwise, the track with the highest χ^2 probability is kept, and the other duplicated tracks are removed.

5.7 Performance in Minimum Bias Events

5.7.1 Conversion Reconstruction Efficiency

The conversion finding efficiency is measured in Minimum Bias simulation events. The efficiency as a function of the conversion radius, pseudorapidity η and p_T is presented in Figs. 5.9, 5.10 and 5.11.

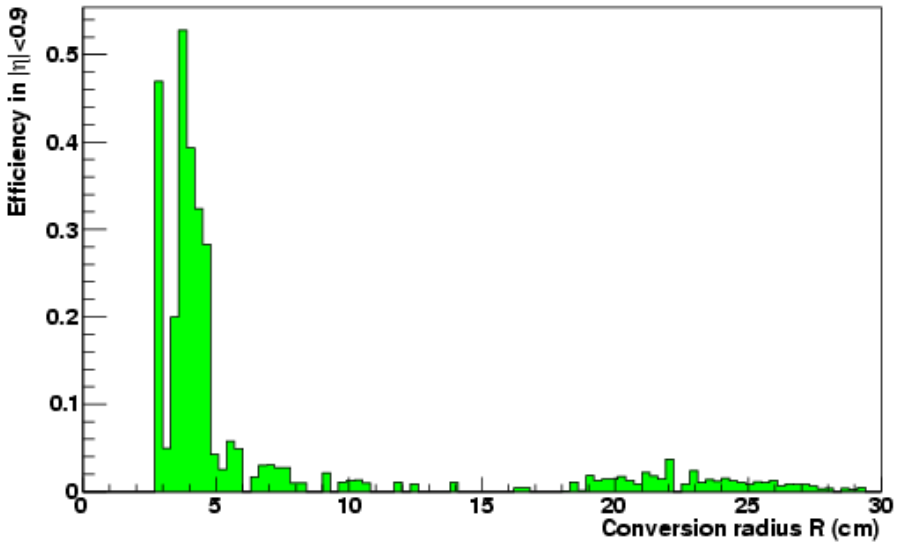

Figure 5.9: Conversion finding efficiency estimated from the simulated sample of Minimum Bias events at 7 TeV as a function of conversion radius for $|\eta| < 0.9$.

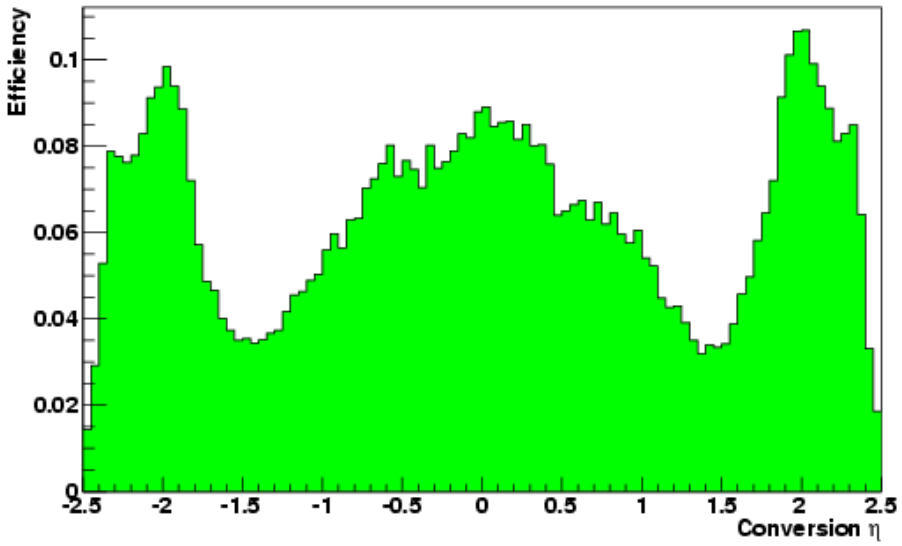

Figure 5.10: Conversion finding efficiency estimated from the simulated sample of Minimum Bias events at 7 TeV as a function of η.

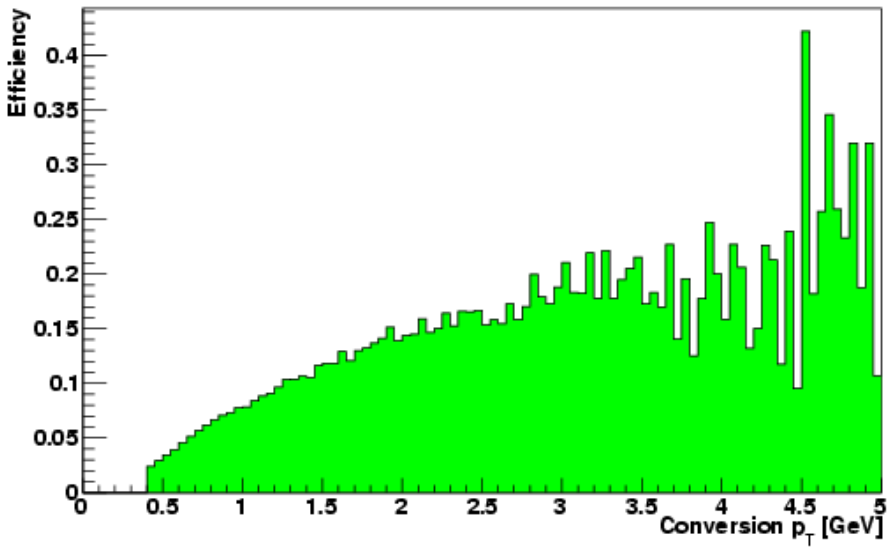

Figure 5.11: Conversion finding efficiency estimated from the simulated sample of Minimum Bias events at 7 TeV as a function of p_T.

5.7.2 Conversion Selection Properties

Figure 5.12, 5.13 and 5.14 [67] show a very good agreement between data and Minimum Bias Monte Carlo events for the conversion selection variables discussed before. In all of the plots, the normalization is to the number of conversions in data after the cuts.

The χ^2 probability of the final constrained vertex fit is shown in Figure 5.15 [67] after applying all cuts, including the one on the probability itself.

The reconstructed conversion pseudorapidity (η) and azimuthal angle (ϕ), measured from the direction of the track-pair momentum for the whole tracker, are shown in Figs. 5.16(a), 5.16(b) [67] respectively. The ϕ distribution is shown in Figure 5.17(a) [67] for the pixel barrel ($|z| < 26$ cm, $R < 19$ cm) where the structure of the Pixel detector cooling pipes is clearly visible. The ϕ distribution of the Inner Silicon barrel ($|z| < 73$cm

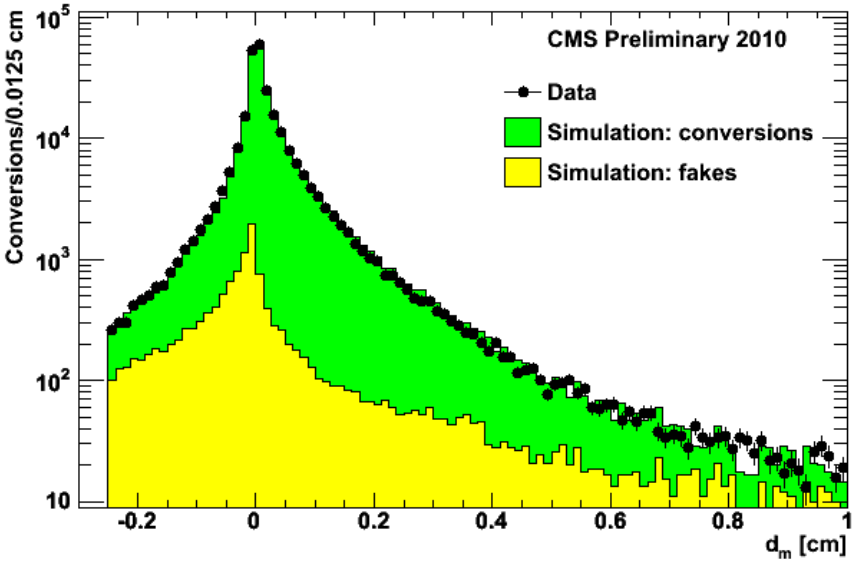

Figure 5.12: Distance of minimum approach, d_m, between the two photon conversions tracks in Minimum Bias events

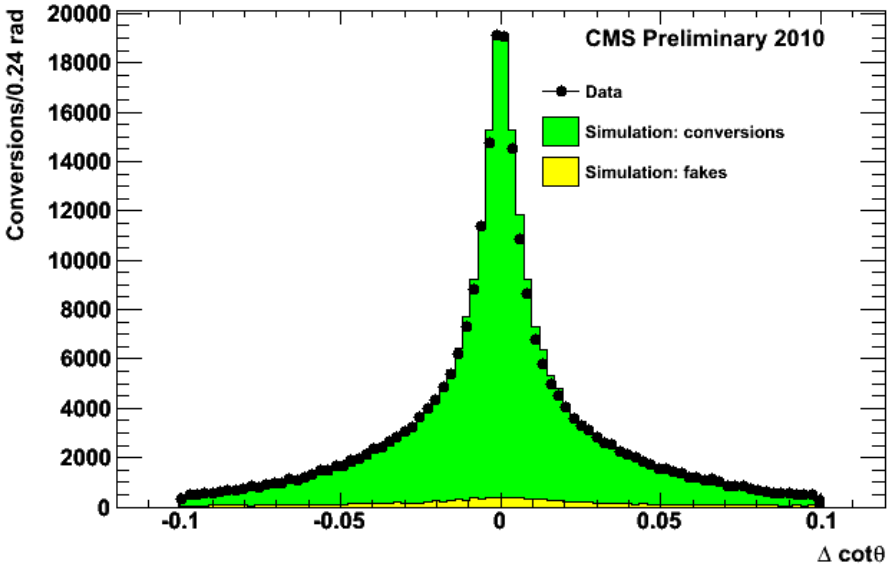

Figure 5.13: Angular separation in the longitudinal plane, $\Delta \cot \theta$, of tracks in Minimum Bias events

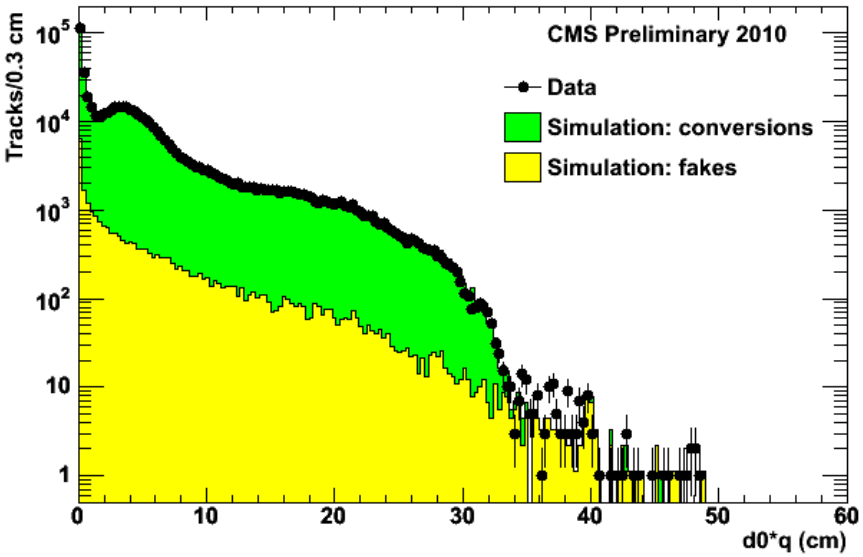

Figure 5.14: Charge-signed transverse track impact parameter of tracks, $Q \cdot d_0$ in Minimum Bias events

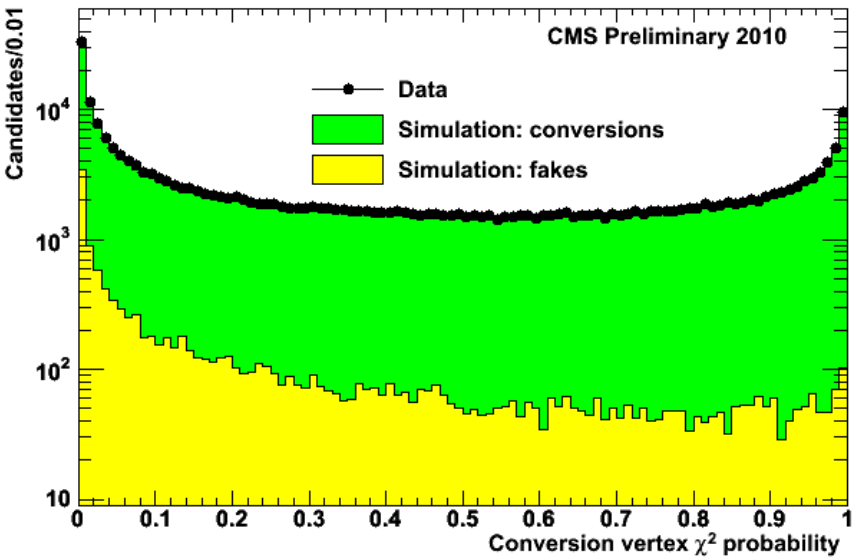

Figure 5.15: Distribution of the vertex χ^2 probability in Minimum Bias events, with all selection cuts applied.

and $R > 22$cm) is shown in Figure 5.17(b) [67]. The shape of the distribution reflects the structure of the material, as well as a small number of non-working modules.

The radial position of conversions is shown in Figure 5.18(a) [67] (selecting $|z| < 26$ cm) i.e. integrating on the very central part of the barrel; the beam pipe, three Pixel layers and the four inner barrel strip layers are clearly illustrated. In data the vertex position is calculated with respect to the center of the Pixel barrel detector in order to take into consideration the overall shift between the tracker and the nominal reference frame ($x = -0.147$ cm, $y = -0.378$ cm, $z = -0.485$ cm). The longitudinal coordinate is shown in Figure 5.18(b) [67] selecting the Pixel detector (3.5 cm $< R <$ 19 cm). In general, the distributions are very well described by the Monte Carlo simulation, with only limited localized discrepancies.

5.7.3 Tracker Material Map

Conversion vertices are reconstructed with an excellent precision: the angular resolution is about 1 mrad while the radial resolution varies in a range of about 0.2 cm to about 0.5 cm, primarily as a function of pseudorapidity.

The position of conversion vertices reconstructed in data is shown in the (x, y) plane in Figure 5.19 [67]. In Figure 5.19(a) [67] the very center part of structure is the Pixel detector, surrounded by the shell and rails supporting it, four layers of the Inner Tracker and the first layer of the Outer Tracker. The beam pipe is clearly visible as off-centered with respect to the Pixel detector, when restricting the (x, y) view to $\pm$ 12 cm (Figure 5.19(c) [67]).

The (z, R) view of conversion vertices reconstructed in data is finally shown

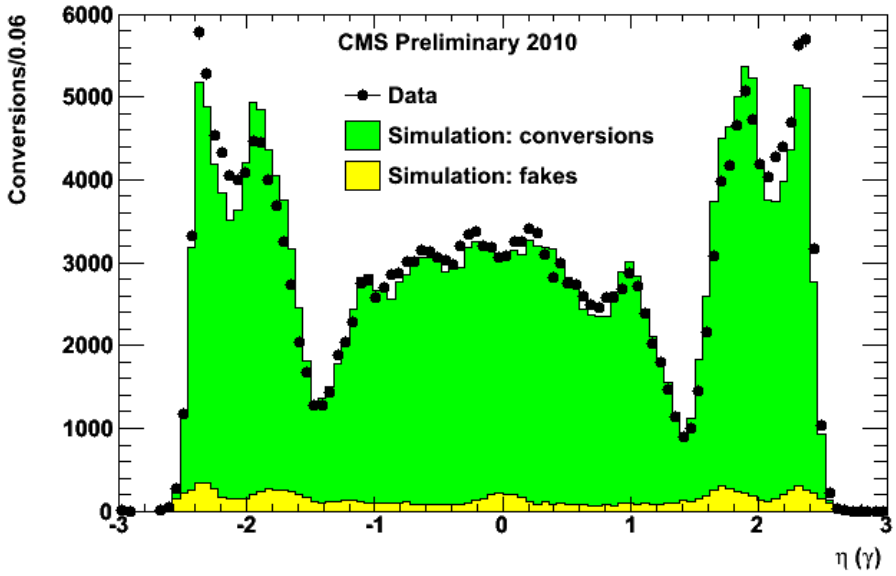

(a)

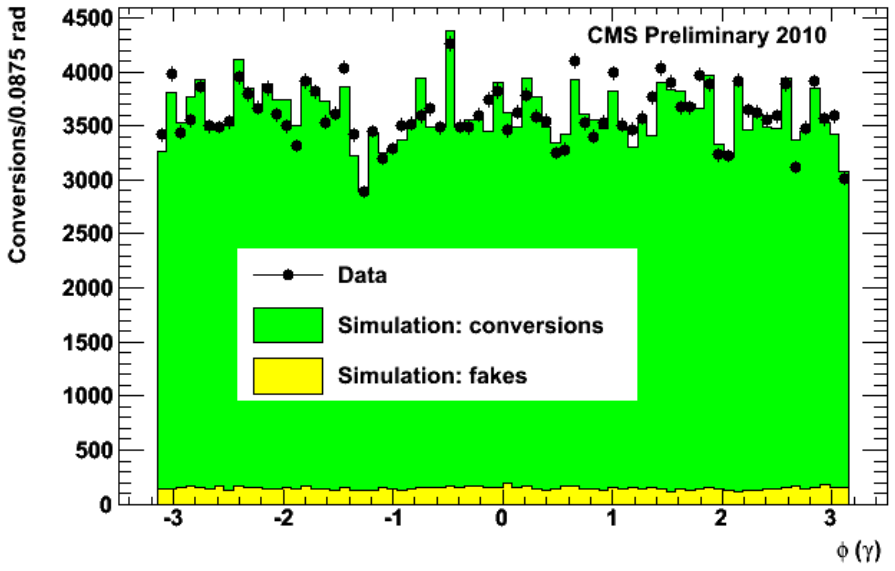

(b)

Figure 5.16: Pseudo-rapidity distribution (a) and ϕ distribution (b) for all conversion candidates in Minimum Bias events, as reconstructed from the track-pair momentum. The contribution expected from fakes is shown in all plots.

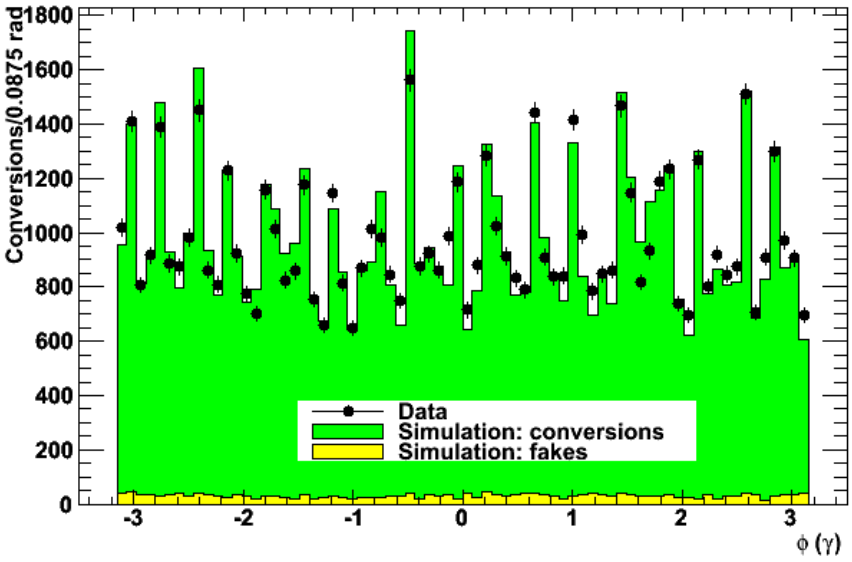

(a)

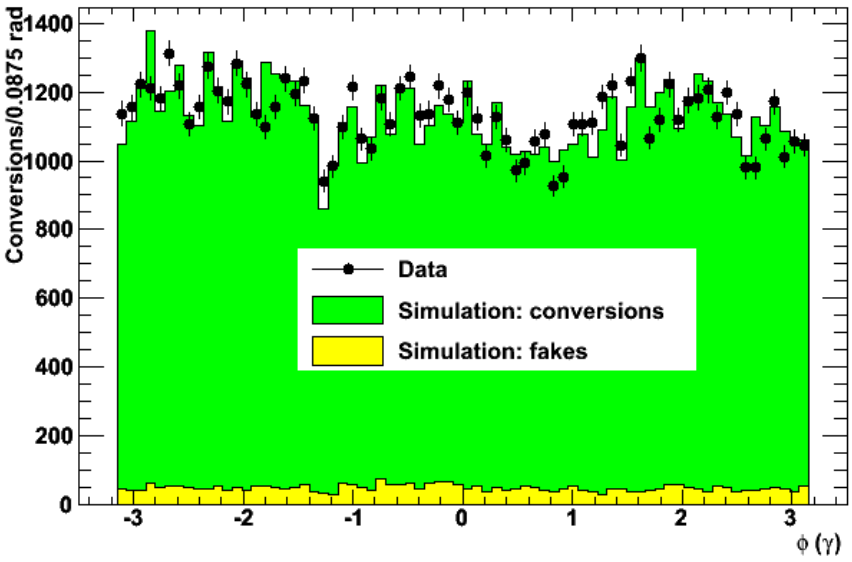

(b)

Figure 5.17: The ϕ distribution for candidates selected in the Pixel barrel with $|z| < 26$ cm and $R < 19$ cm (a) and in the Inner Strip barrel with $|z| < 73$ cm and $R > 22$ cm (b). The contribution expected from fakes is shown in all plots.

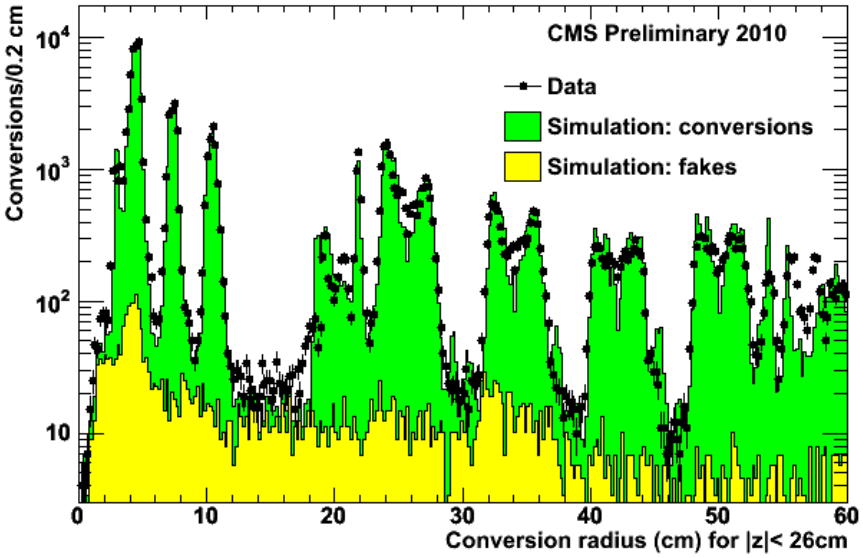

(a)

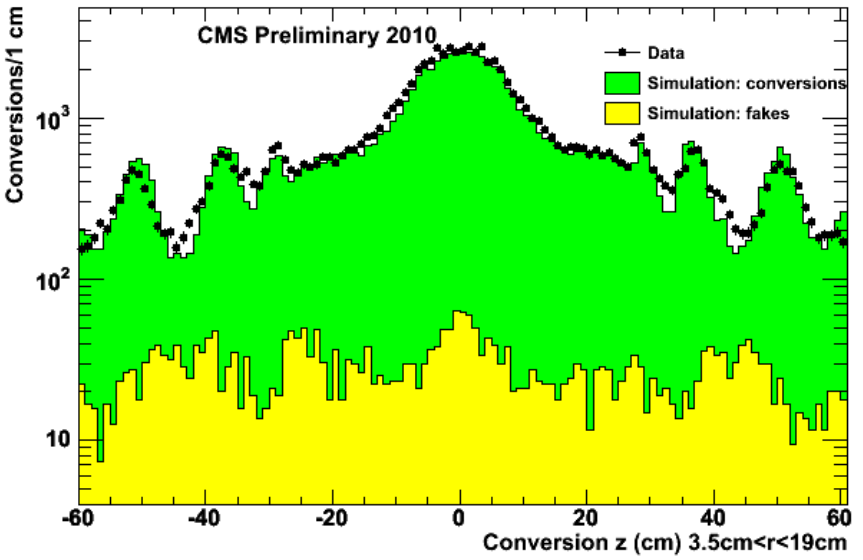

(b)

Figure 5.18: Conversion vertices: distributions of the radial position for $|z| < 26$ cm, i.e. the central portion of the tracker barrel (a), and longitudinal position for 3.5 cm $< R <$ 19 cm, i.e. Pixel Detector, (b). In data the radius is calculated with respect to the centre of the Pixel detector.

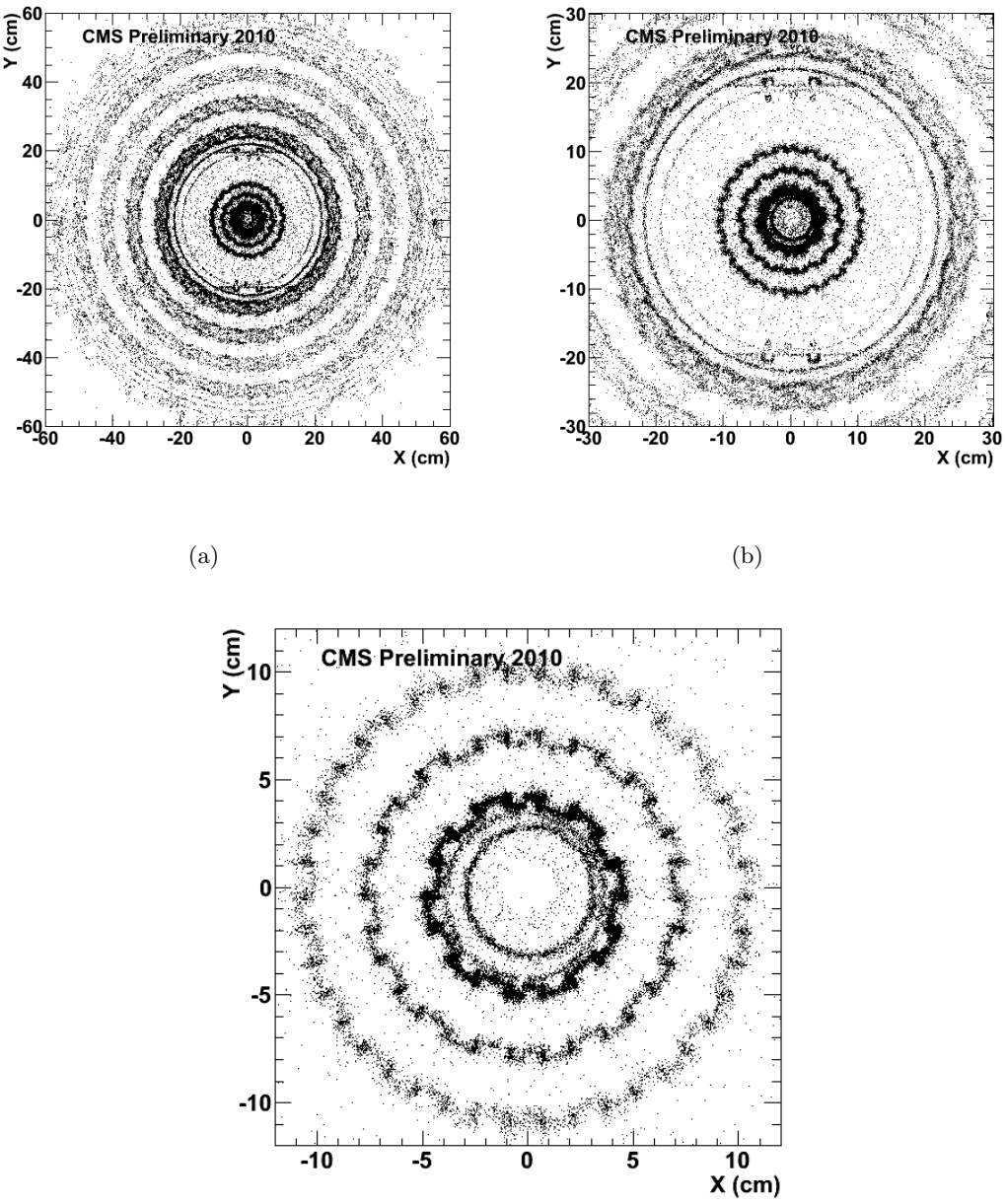

(a) (b)

(c)

Figure 5.19: Conversion vertices in data in the (x, y) plane for $|z| < 26$ cm; zoom increases from (a) to (c).

in Figure 5.20 [67]. The less populated areas (around $|\eta| \sim 1.2$) are also present in simulation, corresponding to transition regions between the tracker barrel and endcap sub-components.

5.8 Systematic Uncertainty of Conversion Reconstruction Efficiency

In the Minimum Bias events, the photons have low momentum and the low momentum conversion reconstruction efficiency has been studied in the previous section. To study the efficiency and the systematic uncertainty of high energy photon conversions, we use the radiative leptonic Z decays of $Z \to \mu\mu\gamma$ to study the conversion reconstruction uncertainties. We select $Z \to \mu\mu\gamma$ events in data and Monte Carlo samples, and compare the conversion-photon ratio to determine the uncertainties.

5.8.1 Datasets

Data samples: Di-muon skim with luminosity of 2.2 fb^{-1}

- `/DoubleMu/Run2011A-May10ReReco-v1/AOD` run 160404-163869
- `/DoubleMu/Run2011A-PromptReco-v4/AOD` run 165088-167913
- `/DoubleMu/Run2011A-05Aug2011-v1/AOD` run 170249-172619
- `/DoubleMu/Run2011A-PromptReco-v6/AOD` run 172620-173692

Monte Carlo samples:

- `/DYToMuMu_M-20_CT10_TuneZ2_7TeV-powheg-pythia/Summer11-PU_S4_START42_V11-v1/AODSIM`
- `/WJetsToLNu_TuneZ2_7TeV-madgraph-tauola/Summer11-PU_S4_START42_V11-v1/AODSIM`

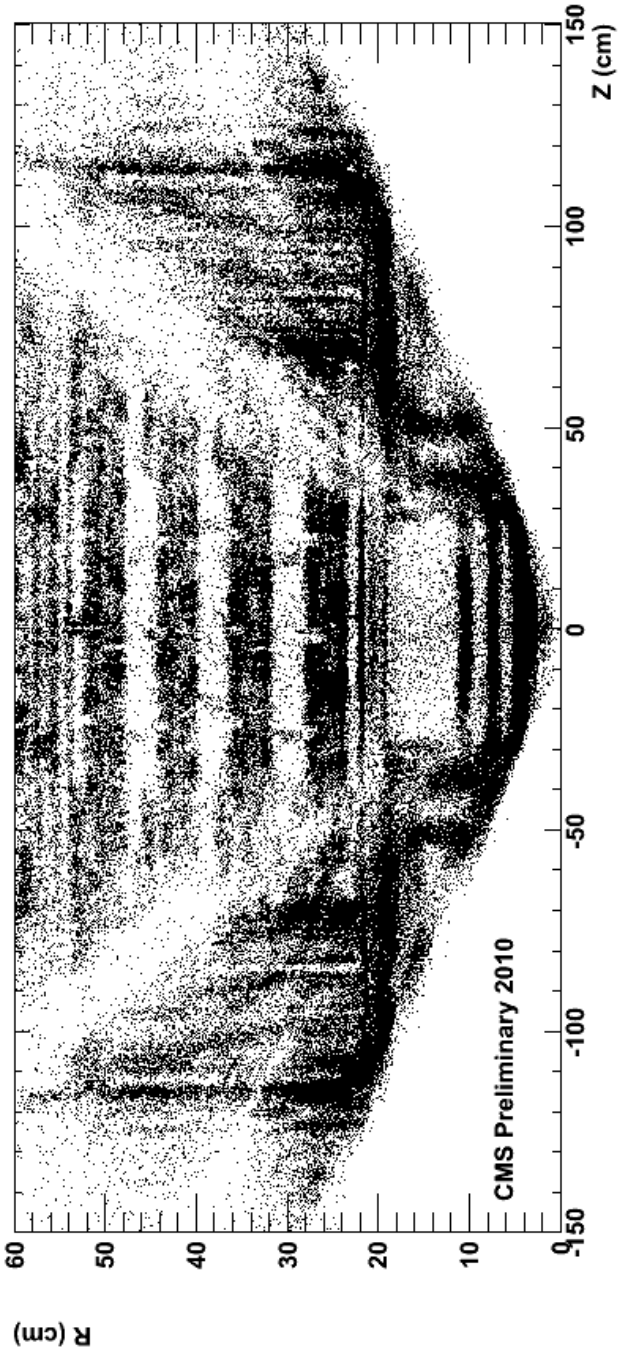

Figure 5.20: Conversion vertices in data the (z, R) plane.

- /TTJets_TuneZ2_7TeV-madgraph-tauola/Summer11-PU_S4_START42_V11-v2/AODSIM
- /QCD_Pt-20_MuEnrichedPt-10_TuneZ2_7TeV-pythia6/Summer11-PU_S3_START42_V11-v2/AODSIM

5.8.2 Selections

The $Z \to \mu\mu\gamma$ selection criteria, for the μ selection,

- Global muon and tracker muon
- $p_T > 10$ GeV
- Closest distance of the inner track to (0,0,0), $|d_{XY}(0)| < 2$ cm
- Di-muon with opposite charges
- Di-muon invariant mass [40, 80] GeV
- At least one μ $p_T > 20$ GeV
- Quality selection as in https://twiki.cern.ch/twiki/bin/viewauth/CMS/ZToLLGamma.

For the γ selection,

- In the ECAL barrel
- $p_T > 10$ GeV
- Photon isolation selection criteria as in Section 4.2.5.4.

Also, the photon conversion should geometrically match with one selected photon, with momentum-energy matching $0.8 < p_T/E_T < 1.3$.

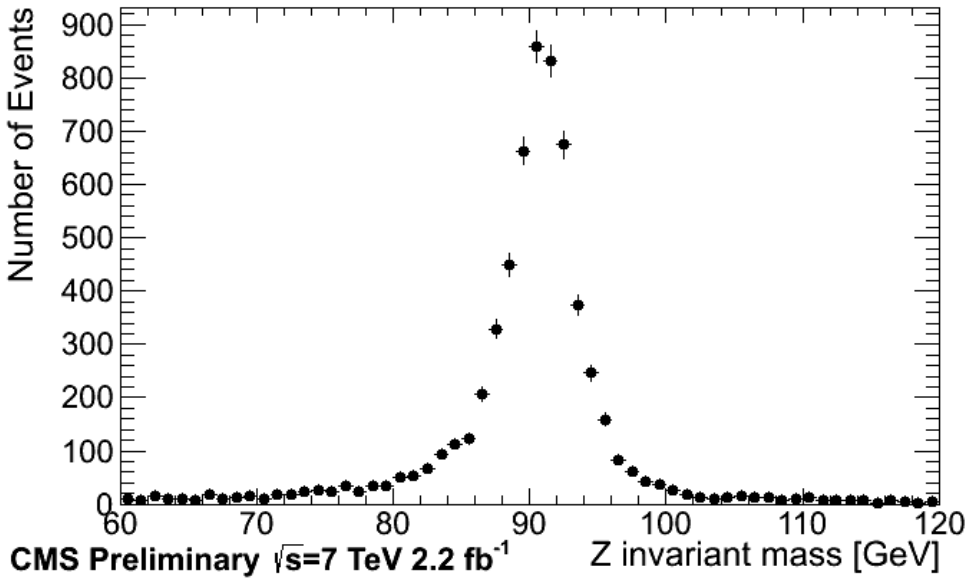

(a)

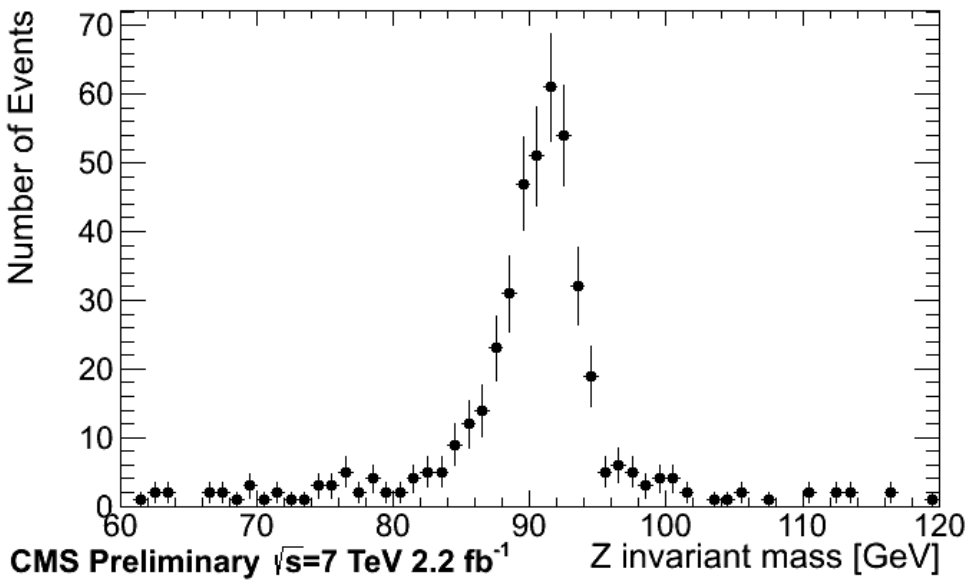

(b)

Figure 5.21: Z invariant mass in data samples (a) 6067 events with photons (b) 449 events with photons and matched conversions.

5.8.3 Reconstruction Efficiency Uncertainty

In the Z loose mass window $60 < M_Z < 120$ GeV, 6067 events of $Z \to \mu\mu\gamma$ are observed in data, among which 449 events have reconstructed conversions (Figure 5.21).

In the Monte Carlo samples, only Drell-Yan to di-muon samples can have $Z \to \mu\mu\gamma$, and the selection criteria listed before cut out all the events from the QCD, $t\bar{t}$ and $W \to \mu\nu$. In the Z loose mass window $60 < M_Z < 120$ GeV, 7197 events of $Z \to \mu\mu\gamma$ are observed in Drell-Yan to di-muon Monte Carlo samples and 541 of them have conversions (Figure5.22).

To determine the uncertainty of the conversion reconstruction efficiency, the numbers of conversions are compared by normalizing the number of photons in the $Z \to \mu\mu\gamma$ events from Monte Carlo simulation to data. For photons with $E_T > 20$ GeV, the Monte Carlo predicts 163.0 converted photons over a total of 2329 photons from $Z \to \mu\mu\gamma$, and 141 events are observed in data. A scale factor Data-MC of 0.87 with the error of 8.4% is obtained. Therefore, in the region of interest for the signal search for photons of high E_T, the Monte Carlo and data are consistent, and the Data-MC scale factor for conversion reconstruction is 0.87 ± 0.08 for the signal region of interest.

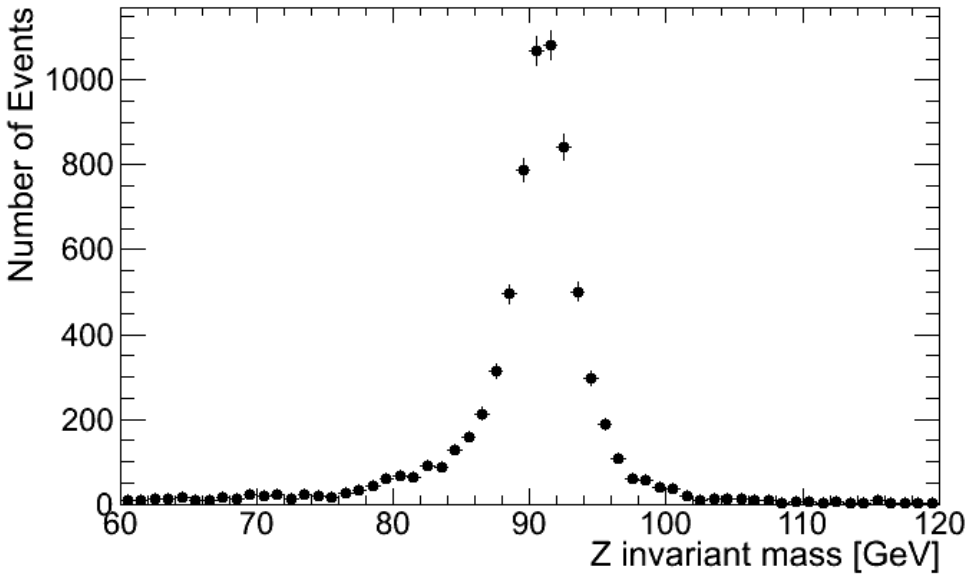

(a)

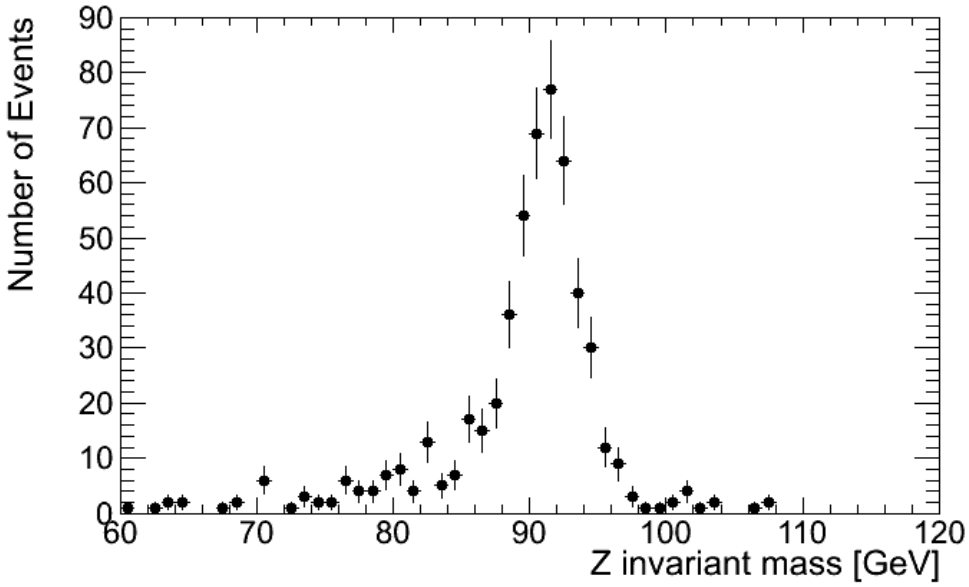

(b)

Figure 5.22: Z invariant mass in Drell-Yan Monte Carlo samples (a) 7197 events with photons (b) 541 events with photons and matched conversions.

Chapter 6

Search for new physics with long-lived particles decaying to photons and missing energy

New heavy particles with long lifetimes are predicted in many models of physics beyond the Standard Model (SM), like Hidden Valley [68] or supersymmetry (SUSY) with gauge-mediated breaking [69, 70, 71, 2, 29, 31]. Such particles may be neutral and decay into photons and invisible particles. Their lifetime is essentially a free parameter of the model. For sufficiently high decay lengths $\mathcal{O}(1\text{ m})$, measurement of shower direction [72] or time-of-flight [73] with the electromagnetic calorimeter can be used to identify such decays.

We devise a new method which is sensitive to much shorter lifetimes for decay lengths of $\mathcal{O}(1\text{ cm})$. Capitalizing on the large amount of material in the CMS tracker, we use photons that undergo conversion into e^+e^- pairs. The tracks of the electrons can be precisely reconstructed and used to calculate the photon trajectory and, in particular,

the impact parameter of the photon with respect to the interaction point.

6.1 Strategy of Search

We search for a signature of a photon with significant impact parameter in association with missing transverse energy. As a signal benchmark, we use the classic gauge-mediated SUSY model SPS8 [74, 4]. Figure 6.1 shows a typical production diagram. Assuming R-parity is conserved, SUSY particles are produced in pairs and decay into SM particles and the lightest neutralino ($\tilde{\chi}_1^0$). The neutralino decays into a photon and a gravitino, which is the lightest SUSY particle in this model, which escapes the detector, leading to apparent missing transverse energy E_T^{miss}. Moreover, in all relevant models, the $\tilde{\chi}_1^0$ is produced in association with high p_T jets. We consider neutralino decay lengths between $c\tau = 2$ cm and $c\tau = 25$ cm, corresponding to the lifetime in the range of $\mathcal{O}(0.1$ ns) to $\mathcal{O}(1$ ns).

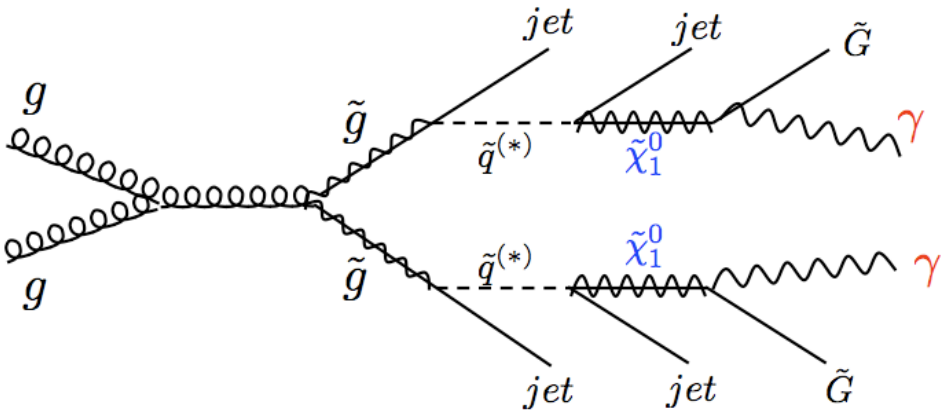

Figure 6.1: Feynman diagram of $\tilde{\chi}_1^0$ pair production and $\tilde{\chi}_1^0 \to \gamma + \tilde{G}$ decay

The data is collected by the CMS detector at the LHC for pp collisions at a center-of-mass-energy of 7 TeV in early 2011, corresponding to an integrated luminosity

of 2.1 fb^{-1}. The analysis strategy is to start with a diphoton final state, then to examine the impact parameter of every single photon for the displaced photon signal. E_T^{miss} and the presence of jets are also required. The background is estimated using a low E_T^{miss} control sample. The results of upper limits on the cross section for pair-production of $\tilde{\chi}_1^0$s, each of which decays into a photon and invisible particles, will be set as the function of $\tilde{\chi}_1^0$ lifetime.

6.2 Monte Carlo samples

6.2.1 Sample Generating

To calculate acceptance times efficiency for signal events, we use a minimal GMSB (Gauge-Mediated Supersymmetry Breaking [19]) generator based on a benchmark model [74]. The PYTHIA6 event generator [59] is used to generate the SUSY GMSB signal datasets in CMSSW_4_2_3. The GMSB parameters are listed in Table 6.1.

- M_m is the messenger scale that defines the mass scale at which MSSM sparticles obtain their masses via gauge interactions with the massive messenger fields;
- N is the number of messenger generations;
- $\tan\beta$ is the ratio between the two MSSM Higgs vacuum expectation values (VEV);
- Signμ is the sign of Higgs and Higgsino SUSY mass parameter μ;
- Λ sets the mass scale for the SUSY breaking in the observable sector, the $\tilde{\chi}_1^0$ mass and the production cross section, where $\Lambda \sim \mathcal{O}(100$ TeV), for example, $\Lambda = 100$ TeV gives a $\tilde{\chi}_1^0$ mass of 140 GeV and $\Lambda = 120$ TeV a $\tilde{\chi}_1^0$ mass of 168 GeV;
- C_{grav} is the ratio between the fundamental scale of SUSY breaking and the scale of

SUSY breaking felt by the messenger particles, which controls both the gravitino mass and the $\tilde{\chi}_1^0$ lifetimes.

According to our strategy mentioned before of search for new physics with long-lived particles, only the $\tilde{\chi}_1^0$ lifetime, determined by the parameter C_{grav}, is strongly related to our analysis, and the other parameters can be considered as irrelevant. The signal selection efficiency is not entirely independent from the $\tilde{\chi}_1^0$ mass, but shown to be a negligible effect in Section 6.5.2.

M_m	N	$\tan\beta$	signμ	Λ	C_{grav}
2-Λ	1	15	+1	free	free

Table 6.1: GMSB Monte Carlo Parameters

The simulation is used to model the final state of two $\tilde{\chi}_1^0$s each decaying to a photon and a gravitino. In the GMSB model, the parameter Λ determines the branching ratio for $\tilde{\chi}_1^0 \to \gamma + \tilde{G}$ and $\tilde{\chi}_1^0 \to Z + \tilde{G}$. We only select those events in which both $\tilde{\chi}_1^0$'s decay to a photon and a gravitino.

In the Monte Carlo samples, the Summer 11 pile-up condition is used and the pile-up has a flat + Poisson tail distribution.

We use Monte Carlo samples with $\tilde{\chi}_1^0$ lifetimes $c\tau$ set to four points: 2 cm, 5 cm, 10 cm and 25 cm. The parameter Λ, which determines the $\tilde{\chi}_1^0$ mass, is set to five different values, 100 TeV, 120 TeV, 140 TeV, 160 TeV and 180 TeV, to examine the mass dependence of the acceptance times efficiency. The value $\Lambda = 100$ TeV is chosen as the standard and the datasets are listed in Table 6.2.

Dataset	$c\tau$ [cm]
/GMSB_Lambda-100_CTau-20_7TeV_pythia6_cff/Summer11-PU_S4_START42_V11-v1	2
/GMSB_Lambda-100_CTau-50_7TeV_pythia6_cff/Summer11-PU_S4_START42_V11-v1	5
/GMSB_Lambda-100_CTau-100_7TeV_pythia6_cff/Summer11-PU_S4_START42_V11-v1	10
/GMSB_Lambda-100_CTau-250_7TeV_pythia6_cff/Summer11-PU_S4_START42_V11-v1	25

Table 6.2: Minimal GMSB Monte Carlo Dataset

In the Monte Carlo simulation, signal photons are found to be mainly in the ECAL barrel region with high transverse energy E_T. The decay model also predicts multiple reconstructed high energy jets, as well as a large value of missing transverse energy E_T^{miss}. We take a particular point of the MC sample, $c\tau$= 5 cm, to illustrate the characteristics of the Monte Carlo samples in Figs. 6.2, 6.3 and 6.4, and these characteristics will be used for the event selection. Because there is no strong dependence on the $\tilde{\chi}_1^0$ lifetime for the E_T and η of photons and the jets, the other GMSB Monte Carlo sample points have similar distributions.

If the $\tilde{\chi}_1^0$ has a non-zero lifetime, the decayed photons can originate in the Tracker volume rather than at the primary vertex and will point away. Quantitively, these photons can have non-zero impact parameters. This non-zero impact parameter (IP) can be the signature of the long-lived $\tilde{\chi}_1^0$ signal, as shown in Figure6.5.

6.2.2 Pile-up reweighting

The Monte Carlo samples have been generated with a flat + Poisson tail distribution for the number of pile-up interactions to match the average number of multiple interactions present in the data and mimic the 2011 data taking conditions. The distribution is as in Figure 6.6 [75]: the red histogram is a Poisson distribution with a mean of ten interactions. The other histogram (blue) in the plot is a distribution that would be obtained with a peak luminosity corresponding to 10 interactions per crossing, decreasing linearly to 5 interactions per crossing during a fill. A comparison of various 2011 distributions is shown in Figure 6.7 [75], where "Current 2011" refers to the early 2011 7 TeV data (2.5 fb^{-1}).

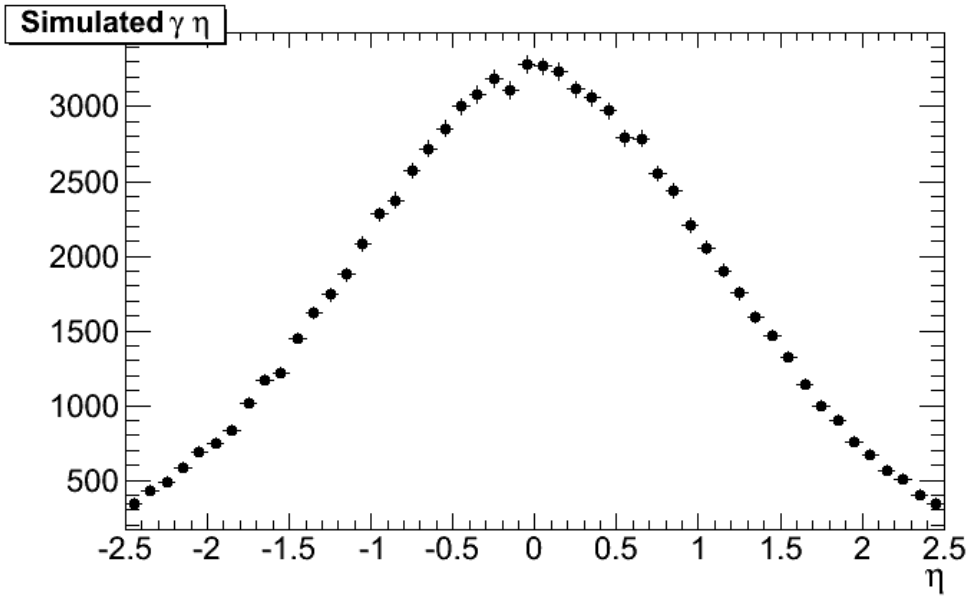

(a)

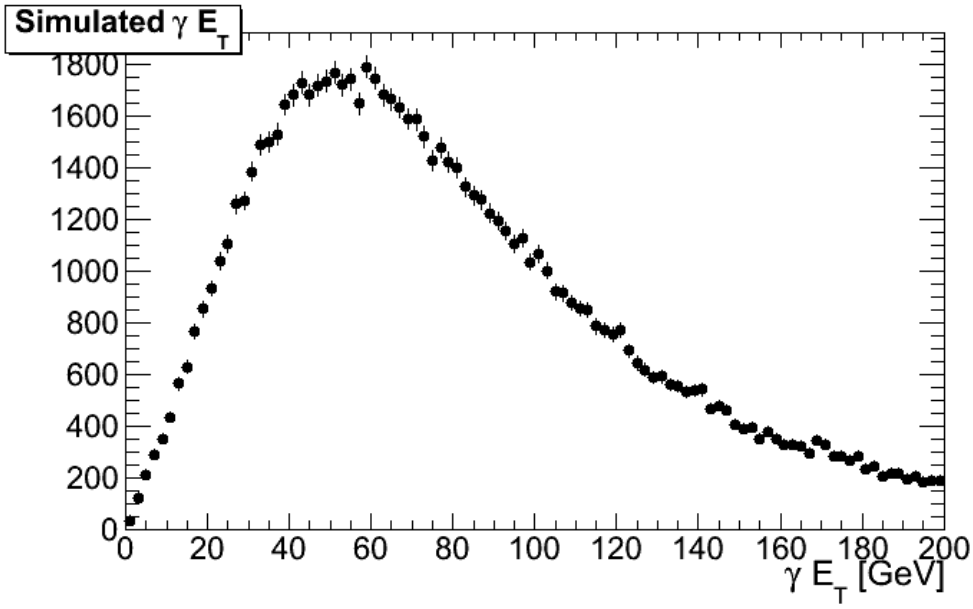

(b)

Figure 6.2: Simulated photon (a)η and (b) E_T distributions from long-lived $\tilde{\chi}_1^0 \to \gamma + \tilde{G}$ where both $\tilde{\chi}_1^0$s decay to photon + $\tilde{G}$.

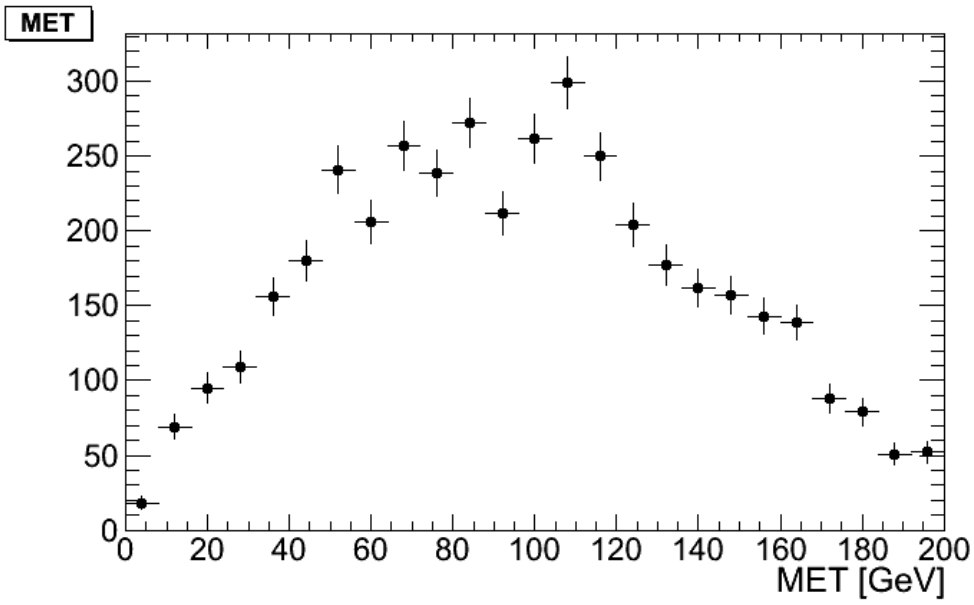

(a)

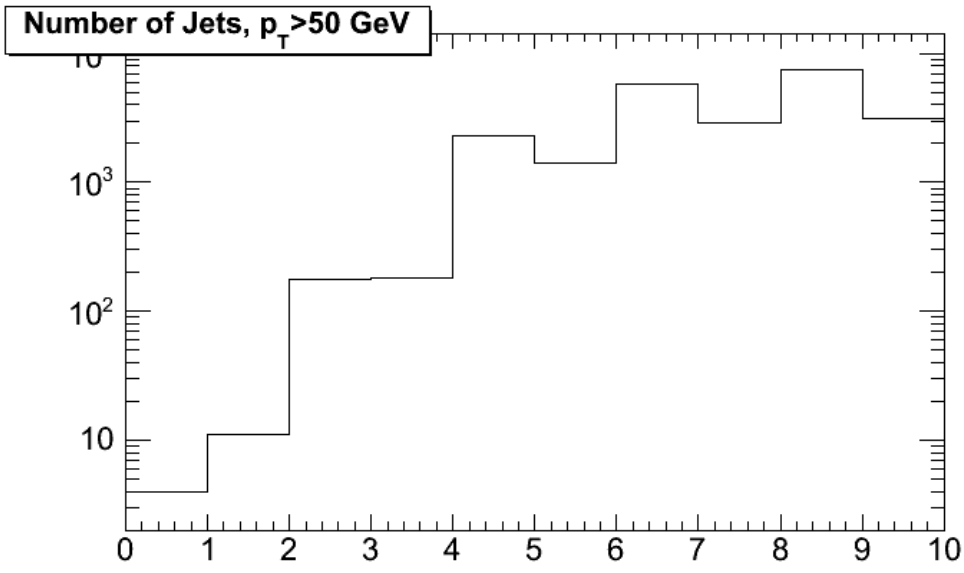

(b)

Figure 6.3: (a) Reconstructed E_T^{miss} using track-corrected E_T^{miss} (b) number of jets with $p_T > 50$ GeV in GMSB MC samples from long-lived $\tilde{\chi}_1^0 \to \gamma + \tilde{G}$ where two $\tilde{\chi}_1^0$ from pair-production with jets and both $\tilde{\chi}_1^0$s decay to photon + $\tilde{G}$.

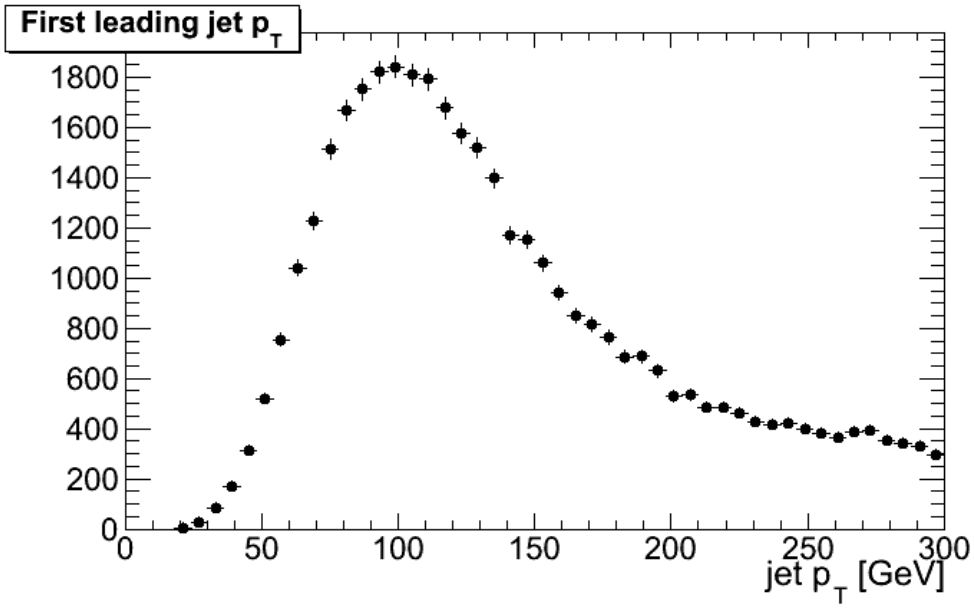

(a)

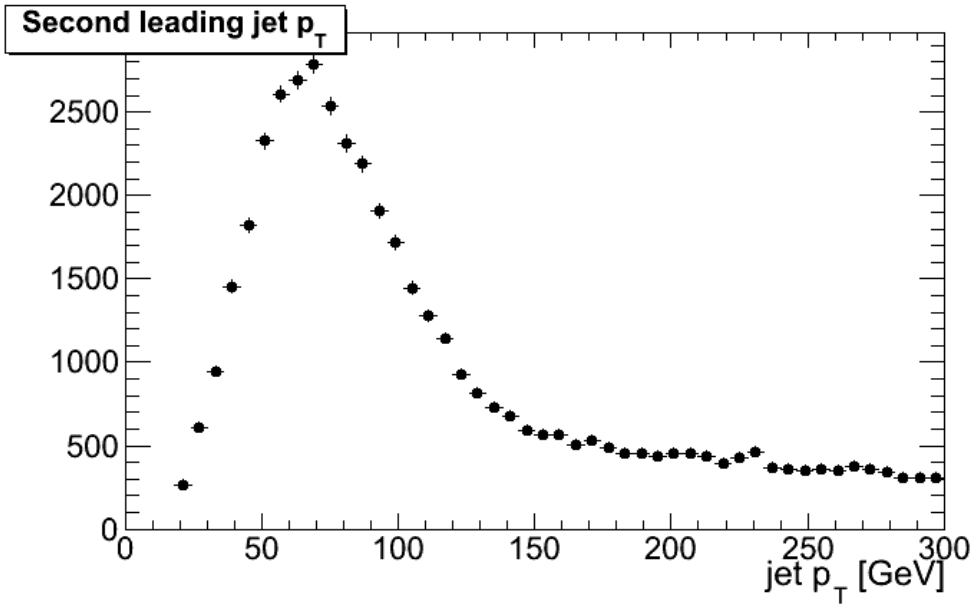

(b)

Figure 6.4: Reconstructed jets using JPT algorithm, (a) first leading jet p_T (a) second leading jet p_T in GMSB MC samples with two $\tilde{\chi}_1^0$'s from pair-production with jets both $\tilde{\chi}_1^0$s decay to photon + $\tilde{G}$.

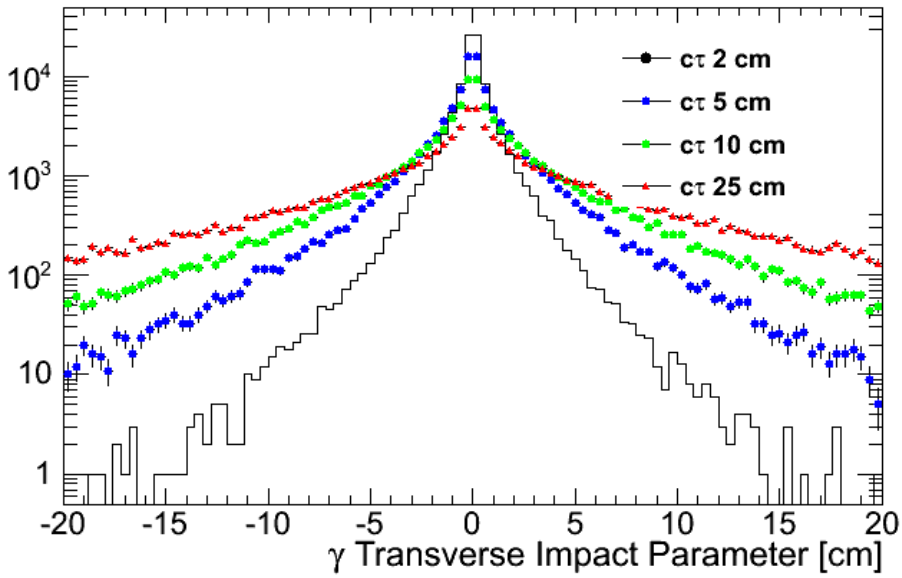

(a)

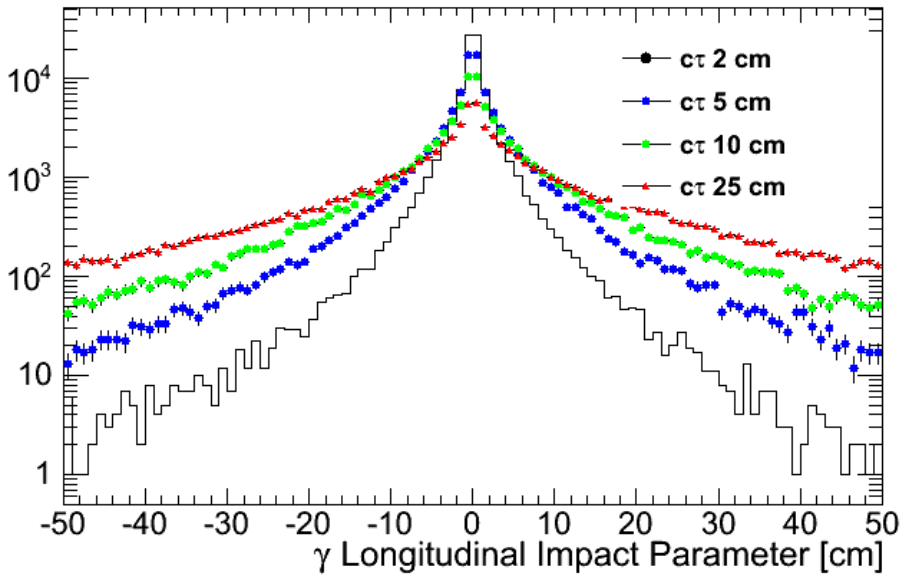

(b)

Figure 6.5: Simulated γ impact parameter from long-lived $\tilde{\chi}_1^0 \rightarrow \gamma + \tilde{G}$ decay, (a) transverse (b) longitudinal.

The pile-up conditions will affect the trigger and conversion reconstruction efficiency; therefore we reweight the number of pile-up interactions of the Monte Carlo truth to match the average data distribution.

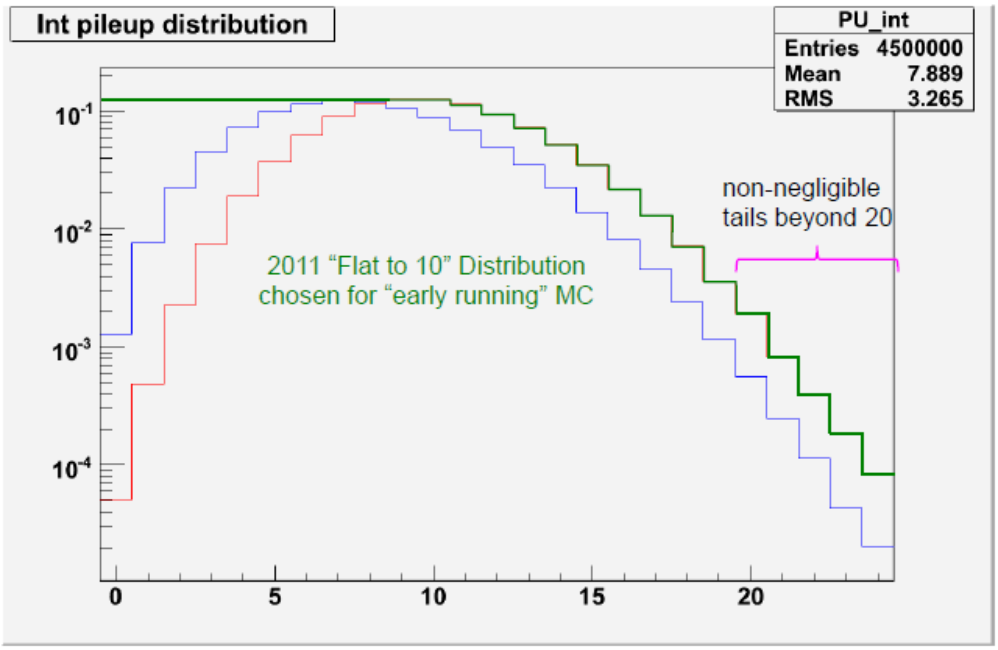

Figure 6.6: Pile-up scenarios of Monte Carlo samples with a flat + Poisson tail distribution for the number of pile-up interactions.

6.3 Event Selection

A search for long-lived $\tilde{\chi}_1^0$'s is performed in the final state of γ's plus jets plus E_T^{miss}. A large impact parameter is also expected for the displaced photon signal.

6.3.1 Trigger

To search for $\tilde{\chi}_1^0$s from pair-production, each of which decays into a photon and invisible particles, at least two photons are required in the final state. Because of the high E_T photons (Figure 6.2(b)) from pair-production $\tilde{\chi}_1^0$s in the signal events,

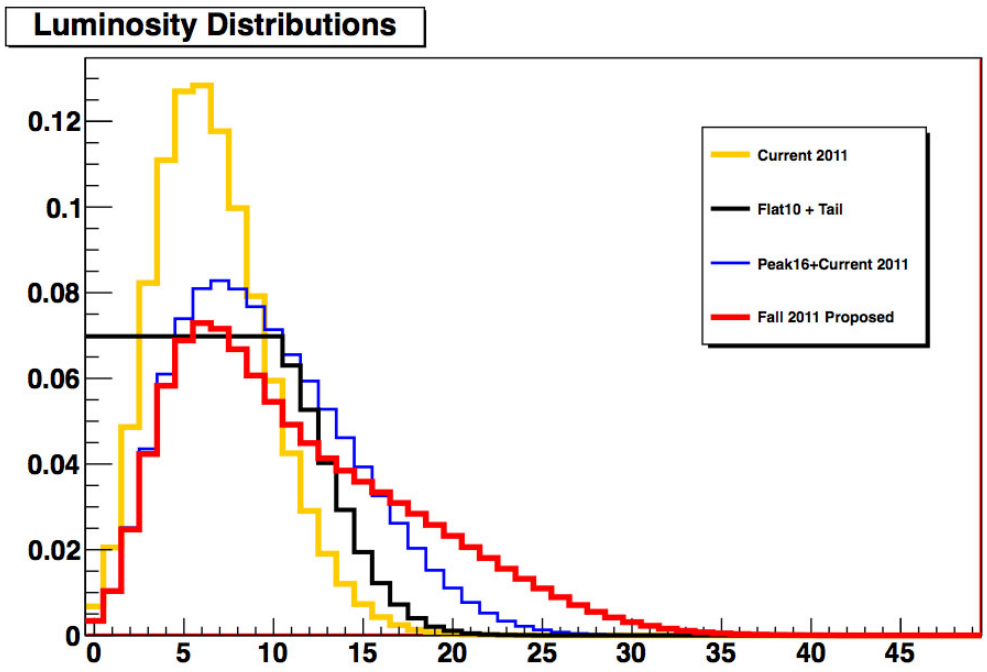

Figure 6.7: Comparison of various 2011 pile-up scenarios.

the data are skimmed using a set of triggers which require at least two photons with asymmetric E_T thresholds to maximize the photon selection efficiency. All triggers use spike-cleaning. The triggers applied in data and Monte Carlo samples are based on the E/γ photon selection trigger menu, and on an OR of the diphoton triggers.

- `HLT_Photon32_CaloIdL_Photon26_CaloIdL_v1(2)(3)`
- `HLT_Photon36_CaloIdL_Photon22_CaloIdL_v1(2)(3)(4)`
- `HLT_Photon40_CaloIdL_Photon28_CaloIdL_v1(2)(3)`

The performance of the triggers has been studied in Ref [4]. The denominator is the number of all the events in the dataset, and the events passing the trigger of interest (e.g. Photon40_CaloIdL_Photon28_CaloIdL) form the numerator for the efficiency determination. The trigger turn-on curve for the Photon40_CaloIdL_Photon28_CaloIdL

trigger is shown for the leading photon on the left-hand side in Figure 6.8 [4] where we require for the sub-leading photon $E_T > 32$ GeV (4 GeV above the 28 GeV threshold) to ensure that the trailing photon is far enough from the corresponding trigger threshold. The right-hand side of Figure 6.8 displays the trigger turn-on for the sub-leading photon where the leading photon has to have $E_T > 44$ GeV (again 4 GeV above trigger threshold).

Similar trigger turn-on curves are shown in Figure 6.9 and 6.10 [4] for the other two triggers used:

- `HLT_Photon32_CaloIdL_Photon26_CaloIdL_v1(2)(3)`
- `HLT_Photon36_CaloIdL_Photon22_CaloIdL_v1(2)(3)(4)`

In both cases we use a Photon22_Photon18 trigger to form the denominator and apply E_T cuts of 4 GeV above the respective leading or sub-leading photon thresholds when determining the efficiencies. The trigger curves for those two triggers plateau at correspondingly lower photon p_T.

To stay on the plateau of trigger efficiency, the offline analysis requires at least two photons with $E_T > 45$ GeV (30 GeV) for the the leading (sub-leading) photon in the event.

In the single photon data samples, it is possible that one or more energetic photons exist (Figure 6.11(a) and 6.12), as well as one or more energetic jets per event (Figure 6.11(b) and 6.13) in every selected event. Therefore, a search for the final state of γs and jets can be performed.

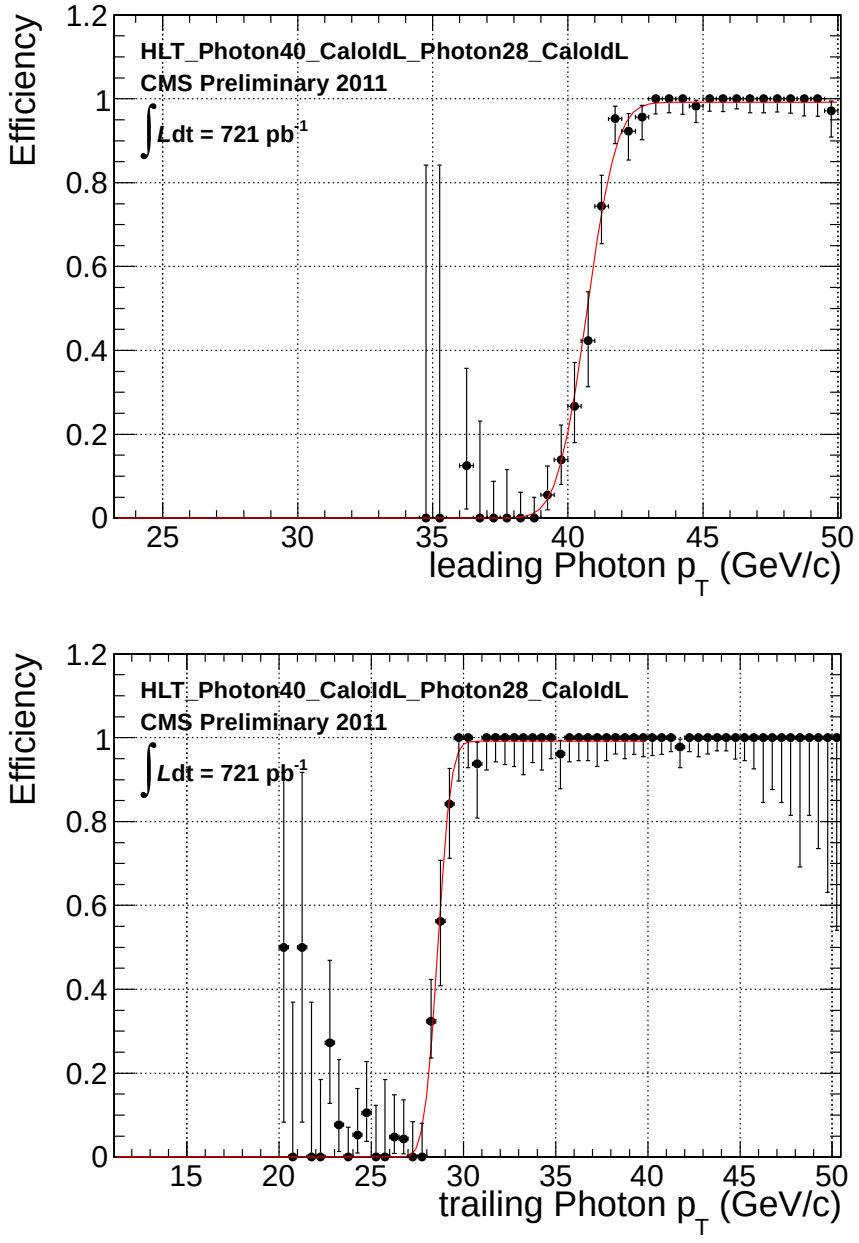

Figure 6.8: Trigger turn-on curve for HLT_Photon40_CaloIdL_Photon28_CaloIdL for the leading photon (top) and the sub-leading photon (bottom).

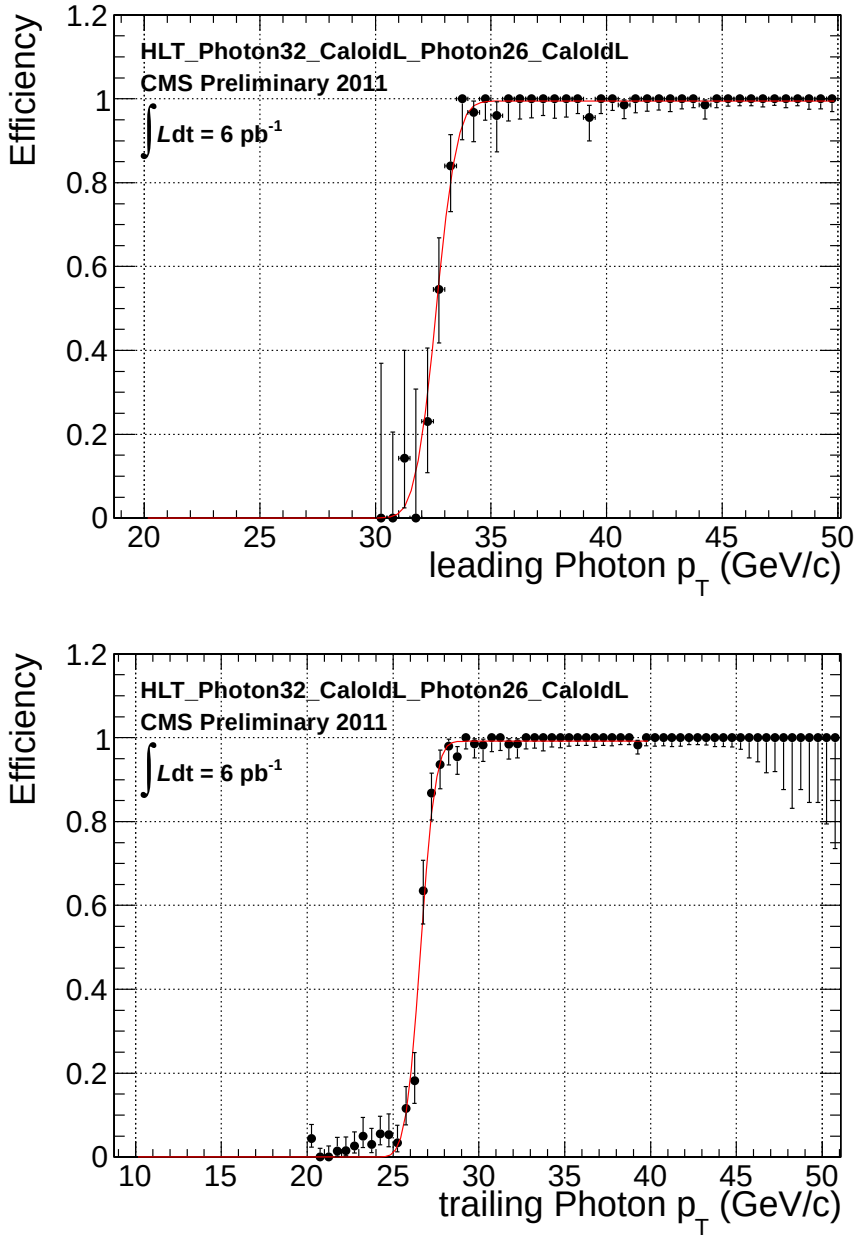

Figure 6.9: Trigger turn-on curve for HLT_Photon32_CaloIdL_Photon26_CaloIdL for the leading photon (top) and the sub-leading photon (bottom).

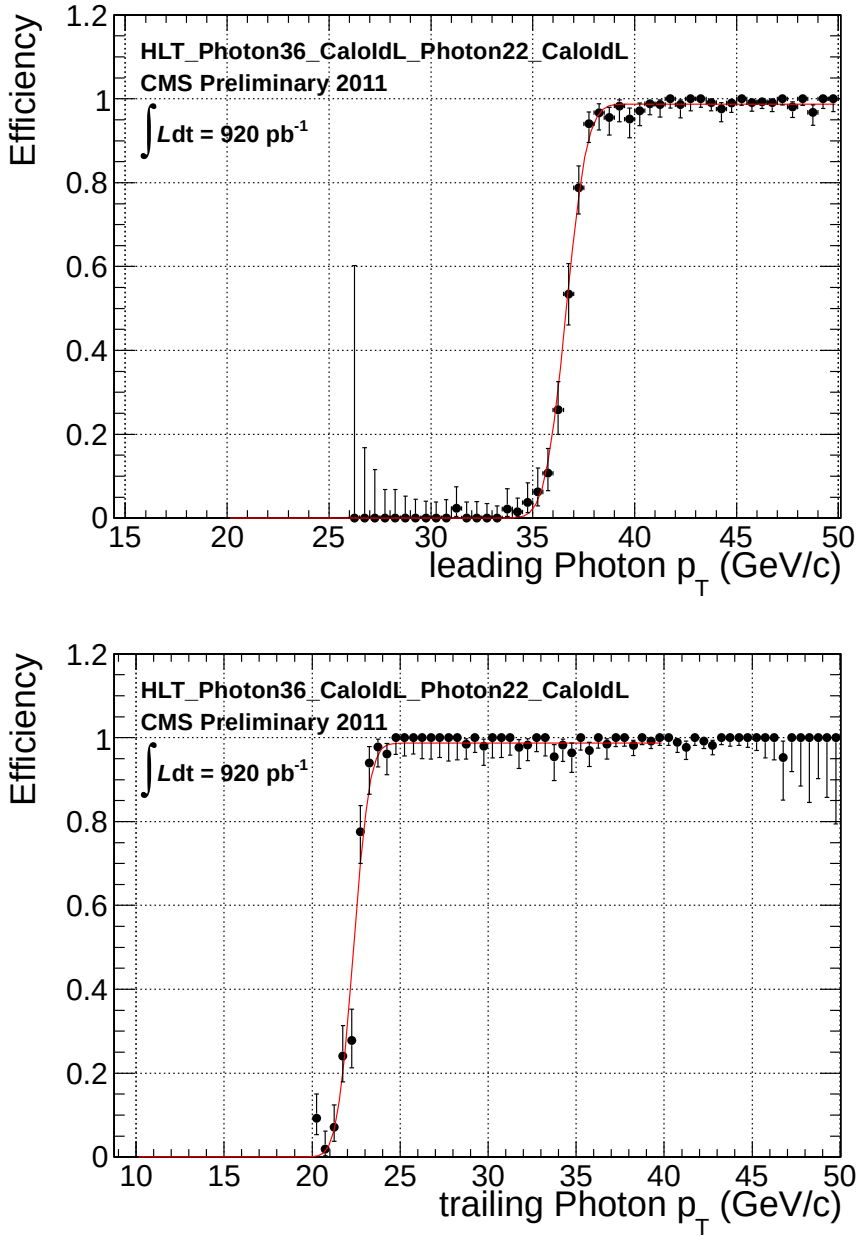

Figure 6.10: Trigger turn-on curve for HLT_Photon36_CaloIdL_Photon22_CaloIdL for the leading photon (top) and the sub-leading photon (bottom).

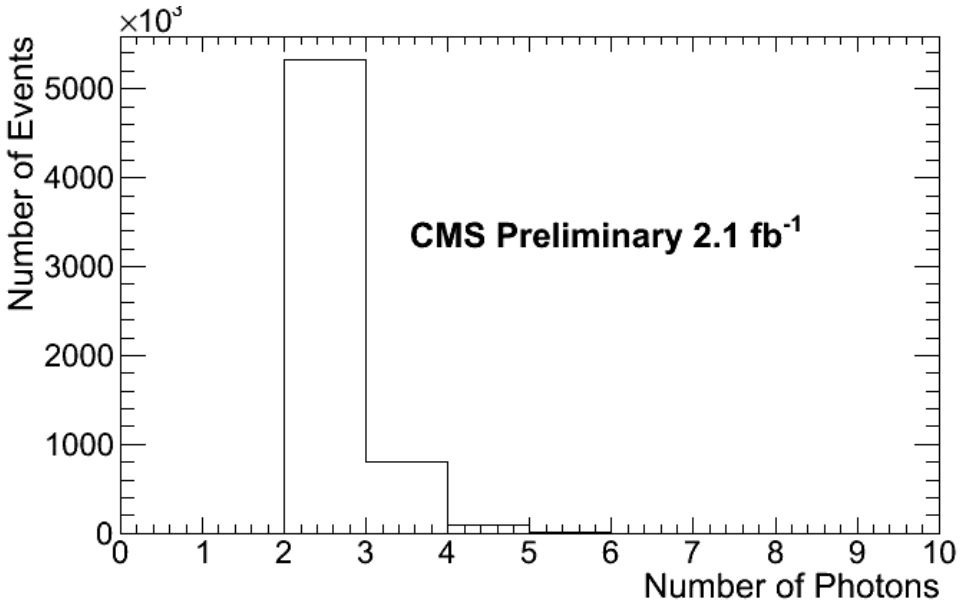

(a)

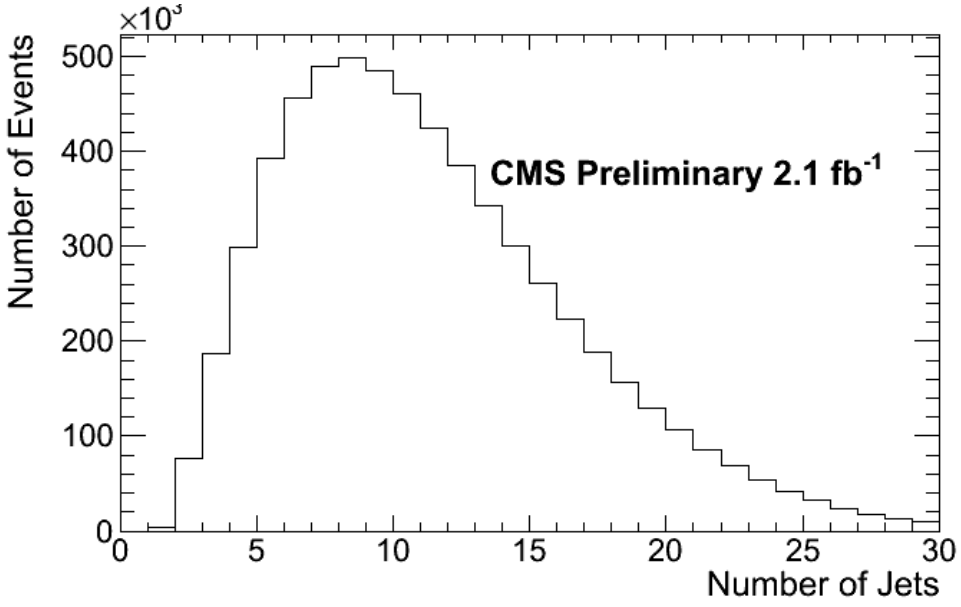

(b)

Figure 6.11: (a) Number of reconstructed photons after diphoton trigger, no E_T cut. (b) Number of reconstructed jets using JPT algorithm after diphoton trigger, no p_T cut, in 2011 7 TeV collision data.

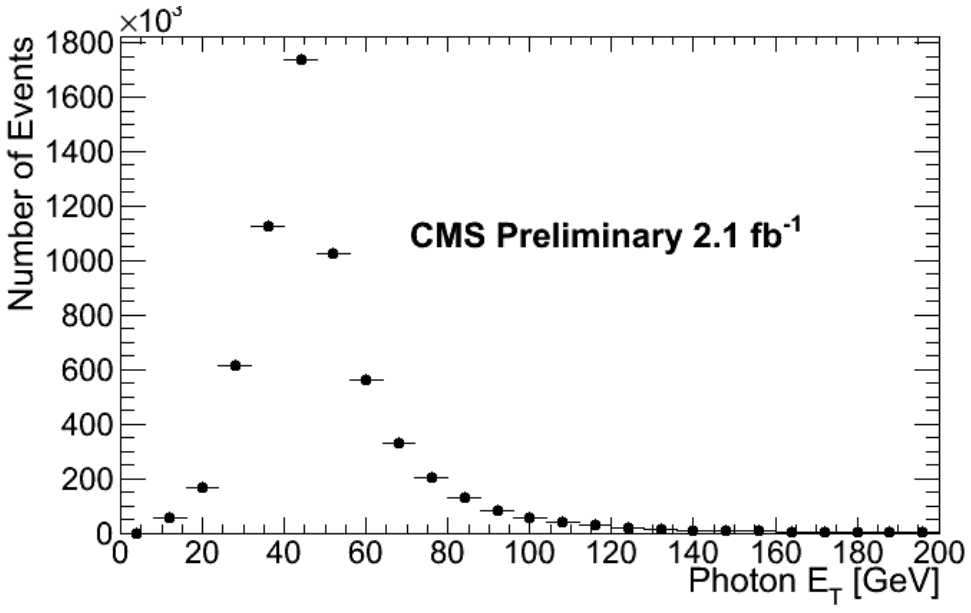

(a)

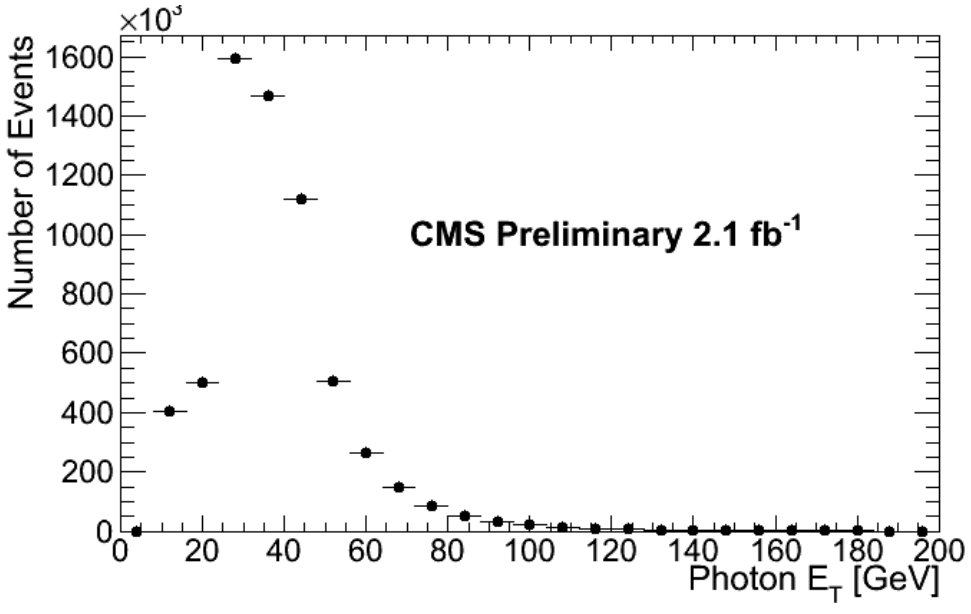

(b)

Figure 6.12: Reconstructed photons after diphoton trigger, no E_T cut. (a) first leading photon E_T (a) second leading photon E_T in 2011 7 TeV collision data.

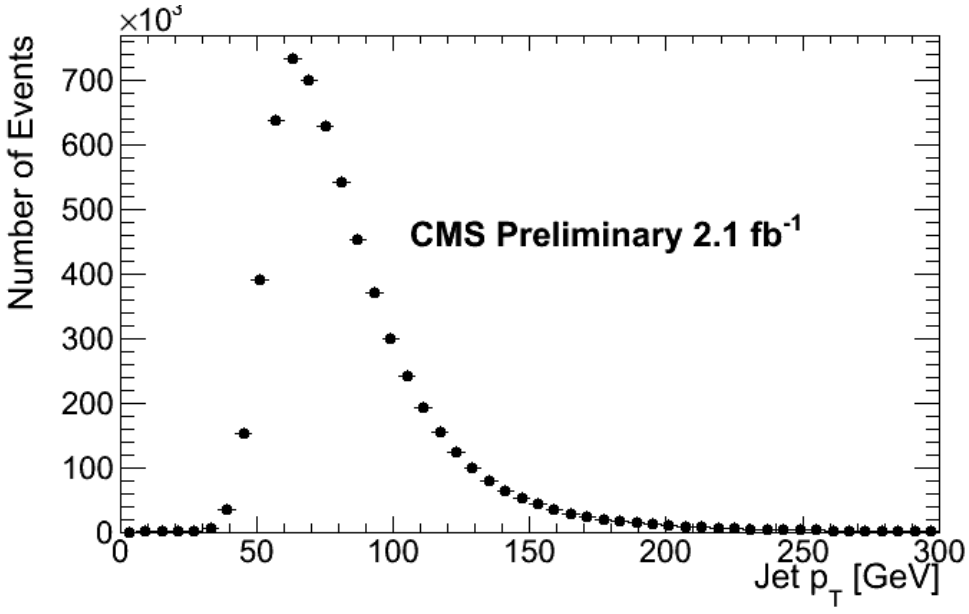

(a)

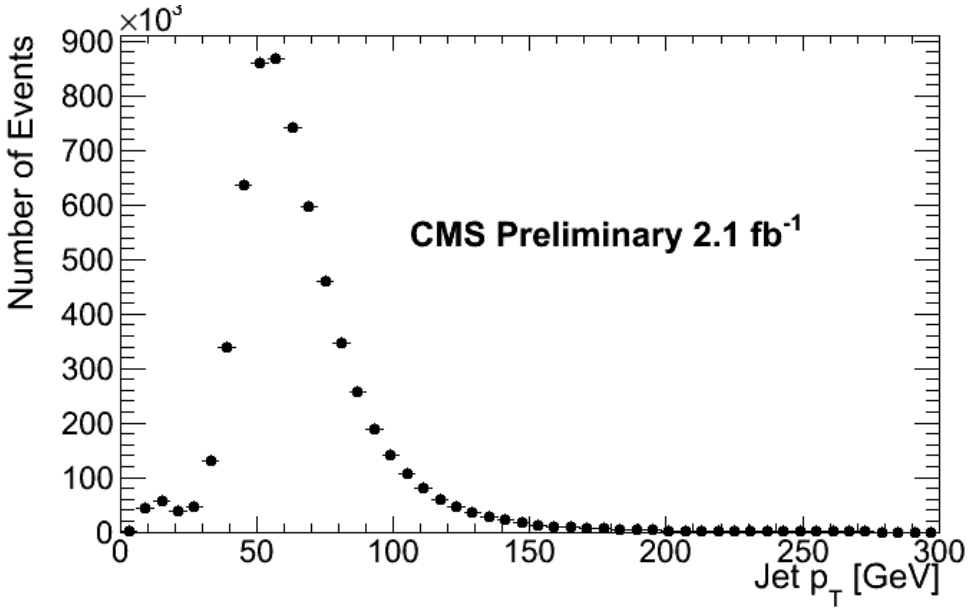

(b)

Figure 6.13: Reconstructed jets using JPT algorithm after diphoton trigger, no p_T cut. (a) first leading jet p_T (b) second leading jet p_T in 2011 7 TeV collision data.

b

6.3.2 Photon Identification

The photon selection requires at least one photon per event in the ECAL barrel with $E_T > 45$ GeV, to have a flat efficiency after the trigger selection in the previous step. The following isolation criteria are applied to select the "good photons":

- ECAL $E_T > 45$ GeV;
- In the ECAL barrel;
- ECAL E_T in the ECAL isolation cone $< 0.006 \cdot E_T + 4.2$ GeV;
- HCAL E_T in HCAL isolation cone $< 0.0025 \cdot E_T + 2.2$ GeV;
- $H/E < 0.05$;
- E_T of the tracks in the track isolation cone $< 0.001 \cdot E_T + 2.0$ GeV;
- $\sigma_{i\eta i\eta} < 0.011$;

The photon isolation criteria have been studied in Section 4.2.5.4. The electron veto is also applied in the photon selection, by rejecting electrons associated with a pixel-seeded photon object but NOT associated with any conversion objects, in order to keep photon conversions from the GSF algorithm. Converted photons are recovered by requiring the pixel matched electron to be consistent with a conversion.

The isolation sums above are not corrected for pile-up effects, which has been studied [4].

6.3.3 Jet Selection

Jets are reconstructed from energy deposits in the calorimeters using the anti-k_T clustering algorithm [48] as described in Section 4.2.2. The energies of these jets are corrected for the p_T of the charged tracks reconstructed in the tracker [49]. At least two jets are required with $p_{T1} > 80$ GeV and $p_{T2} > 50$ GeV and $|\eta| \leq 2.6$.

In the ideal situation, 4 jets are expected for neutralino pair-production as illustrated in Figure 6.1. However, considering the jet reconstruction efficiency and energy resolution, at least two jets with $|\eta| \leq 2.6$ are required, as motivated by Figure 6.3(b), with $p_T > 80$ GeV and $p_T > 50$ GeV, as motivated by comparing the jets momenta in Monte Carlo samples (Figs. 6.4(a) and 6.4(b)) and data (Figs. 6.13(a) and 6.13(b)), to keep signal efficiency and reduce background. The transverse momentum thresholds of the jets ($p_T > 80$ GeV and $p_T > 50$ GeV) are optimized for signal efficiency, as demonstrated in Section 6.5.1 Table 6.3.

6.3.4 E_T^{miss} Selection

Because the $\tilde{G}$ from the $\tilde{\chi}_1^0$ decay is the Lightest Supersymmetric Particle and escapes undetected, E_T^{miss} is expected. The E_T^{miss} is calculated from calorimeter energy deposits and corrected using tracking information. The missing energy E_T^{miss} is corrected for the incomplete calorimeter measurements of muons and charged hadrons energies, called the "tcMET," especially for these soft tracks that do not reach the calorimeters [76]. In Figure 6.14, after the above selections, E_T^{miss} in data shows a peak at about 20 GeV. The background of this analysis is mainly from QCD multijets and γ-plus-jets with no true E_T^{miss}, indicating that the low E_T^{miss} part is mostly from background. There is another selection signature of photon IP to incorporate with

E_T^{miss}, so a relatively low E_T^{miss} cut is sufficient to reduce background, and the low E_T^{miss} cut holds the advantage to examine some neutralino decay models with relatively low E_T^{miss} rather than the GMSB model.

To distinguish the signal from the background, we set a cut of $E_T^{miss} > 30$ GeV for the signal selection, to eliminate most of the background and maintain the signal efficiency, as motivated by comparing Figure 6.3(a) for the Monte Carlo samples and Figure 6.14 of data. The E_T^{miss} threshold of 30 GeV is optimized for signal efficiency.

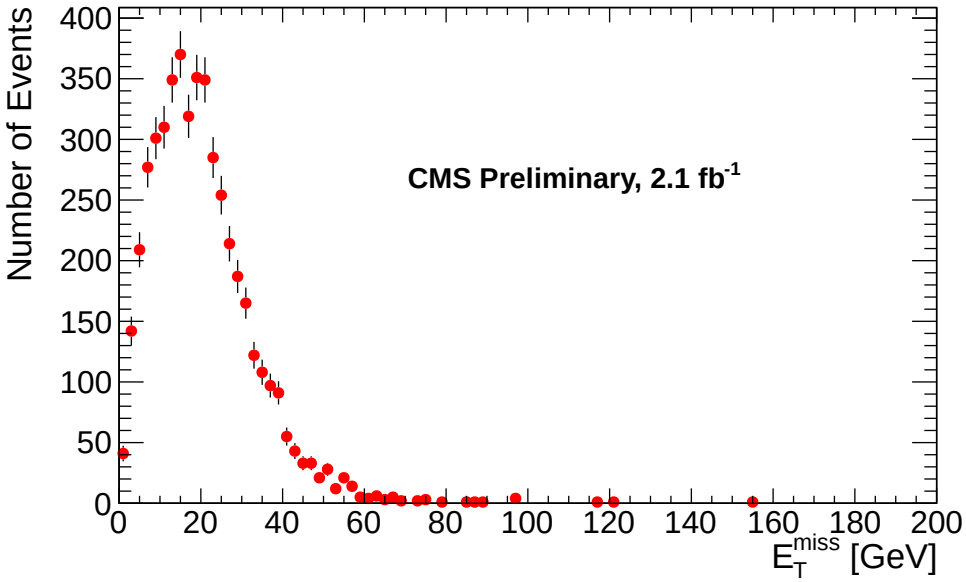

Figure 6.14: E_T^{miss} distribution of data after diphoton trigger, photon selection and jet selection.

6.4 Photon Conversion Method

The detailed studies of photon conversion reconstruction are performed in the previous chapter.

Conversion reconstruction has already been used so far in several physics applications [77, 78]. Not only to recover the missed signal of photons, photon conversions

can also provide a physics measurement that the regular photon reconstruction cannot: the photon direction.

Considering the case that photons from $\tilde{\chi}_1^0$ convert into e^+e^- pairs in the CMS tracker, the photon conversion reconstruction can obtain the photon directions from the e^+e^- pairs, as well as the positions of the conversion vertices. By extrapolating along the momentum direction from the conversion vertex back to the beam line, we can calculate the impact parameter of the displaced photons (Figure6.15) [79].

The transverse impact parameter d_{XY} is the distance of closest approach of the photon trajectory to the beamline in the transverse plane. The longitudinal impact parameter d_Z is the distance from chosen primary vertex and Z position where d_{XY} is calculated (Equation 6.1). The photon trajectory is defined as a straight line from conversion vertex along the conversion momentum.

$$\begin{aligned} d_{XY} &= -L_X \cdot \sin\phi + L_Y \cdot \cos\phi \\ d_Z &= L_Z - \frac{L_X \cdot p_X + L_Y \cdot p_Y}{p_T} \cdot \frac{p_Z}{p_T} \end{aligned} \tag{6.1}$$

In equation 6.1, the L is the vector between the conversion vertex and the primary vertex, and the ϕ angle is the polar angle of the conversion momentum vector p in azimuth, which is calculated by the vector summation of e^+e^- pair momenta at the conversion vertex.

In high luminosity conditions, multiple collisions give multiple primary vertices [80, 81]. The true primary vertex has a large deviation in the longitudinal direction but much less uncertainty in the transverse direction. To be robust against the pile-up conditions, the transverse IP (d_{XY}) w.r.t the transverse position of the beam line is used in this analysis. In Figure 6.16(a), by comparing with the simulation truth in GMSB MC samples, the position resolution of the primary vertex in the transverse plane is

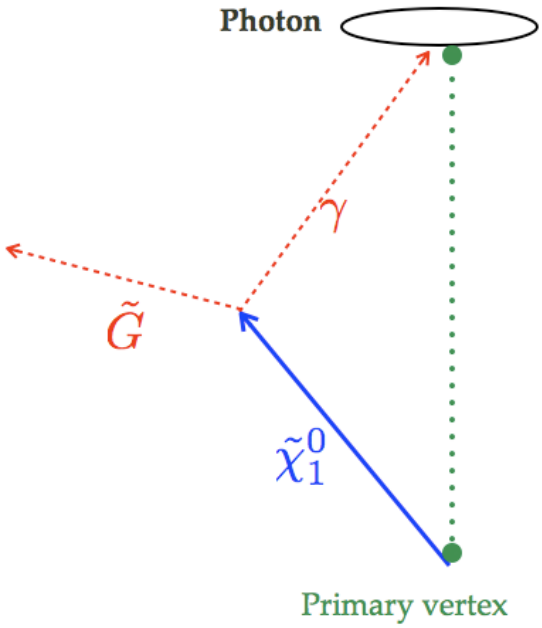

(a)

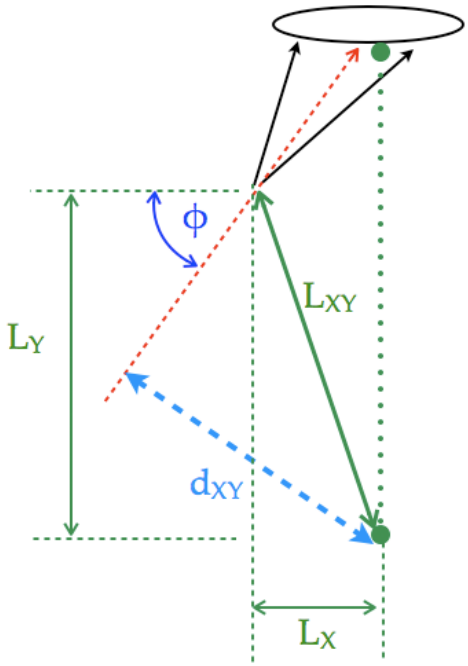

(b)

Figure 6.15: (a) $\tilde{\chi}_1^0 \to \gamma + \tilde{G}$ view in the CMS tracker (b) the photon converts into e^+e^- pairs to reconstruct the impact parameter.

good for all pile-up conditions.

6.4.1 Conversion Selections

The conversions are selected with the following criteria:

- Two tracks of the conversion should have opposite charge;
- At least 5 valid hits for each track;
- Valid vertex fit with χ^2 probability $> 5 \times 10^{-4}$;

If there are more than one conversions, the one with largest d_{XY} is selected in this analysis. The conversion reconstruction is able to find the conversion vertices up to a radius of 60 cm in the CMS tracker (Fig 6.17), which gives the capability to find the displaced photons with conversions.

6.4.2 Displaced Photon Impact Parameter

The impact parameter (IP) of a photon is calculated w.r.t the primary vertex, by extrapolating the conversion momentum from the conversion vertex. In the decay of $\tilde{\chi}_1^0 \to \gamma + \tilde{G}$, the non-zero impact parameter (IP) of the daughter γ indicates a non-zero $\tilde{\chi}_1^0$ lifetime. The reconstructed γ transverse impact parameter d_{XY} distribution from different $\tilde{\chi}_1^0$ lifetimes in MC samples is shown in Figure6.18. The d_{XY} distributions for larger lifetimes spread more in d_{XY}.

By comparing with simulation truth, both primary vertex and conversion vertex reconstruction have a good position resolution in the transverse plane for all pile-up conditions (Figure 6.16). The photon impact parameter resolution is $\sigma_{XY} = 0.011$ cm for transverse IP shown in Figure. 6.19(a), and $\sigma_Z = 0.013$ cm for longitudinal IP shown

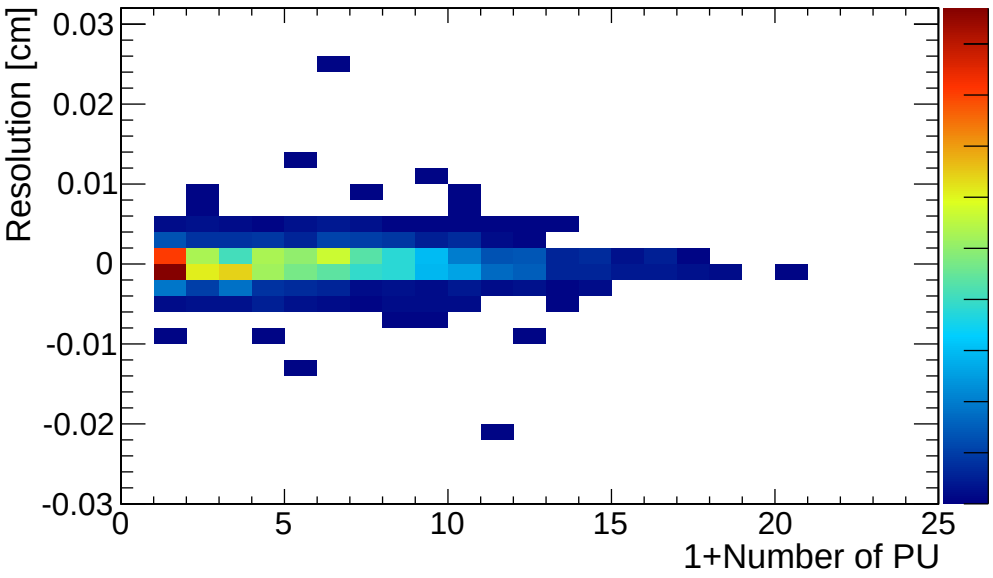

(a)

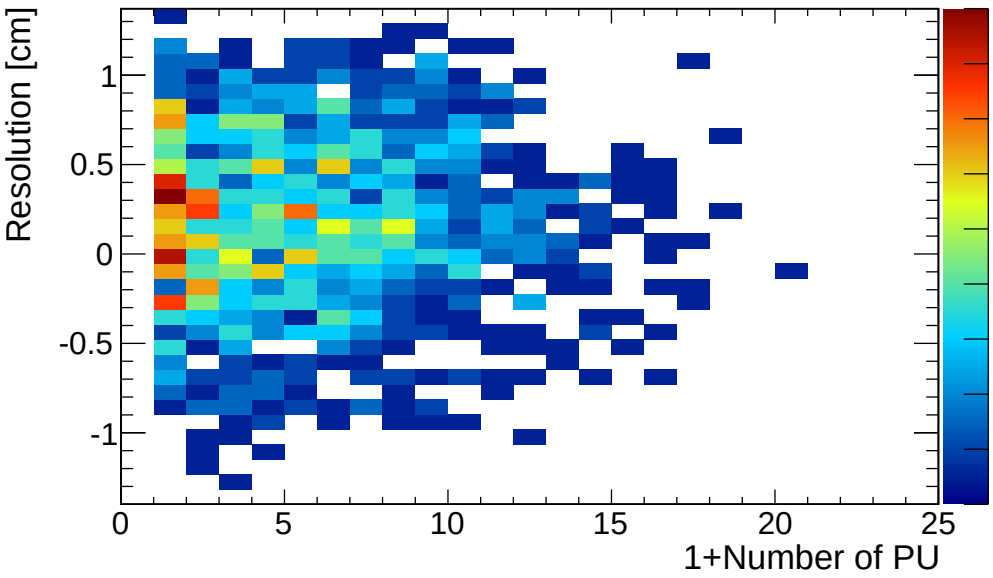

(b)

Figure 6.16: (a) Primary vertex position resolution in the transverse plane vs number of pile-up vertices (b) Conversion vertex position resolution vs number of pile-up vertices, in the transverse plane.

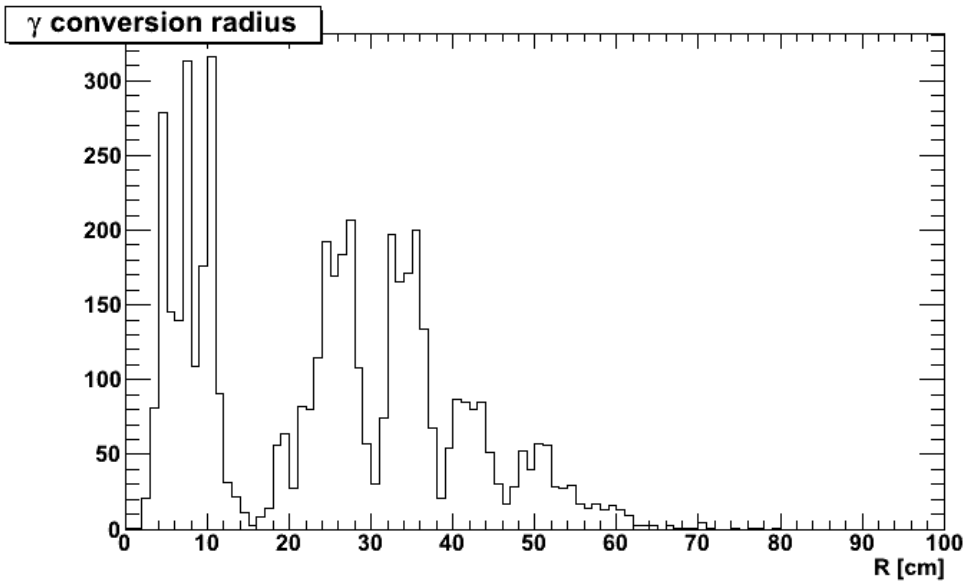

Figure 6.17: Conversion radius in the tracker for $\tilde{\chi}_1^0$ $c\tau = 5$ cm Monte Carlo samples.

in Figure. 6.19(b) from Gaussian fits. Figure 6.19 uses the samples for neutralino mass of 140 GeV and $c\tau = 5$ cm to demonstrate the resolution.

To illustrate the d_{XY} signature, its distribution in data with $E_T^{miss} > 30$ GeV is compared with a Monte Carlo sample with $\tilde{\chi}_1^0$ lifetime $c\tau = 5$ cm and the neutralino mass 140 GeV, as shown in Figure 6.20.

In addition to the trigger requirements and the other selection criteria, a cut on d_{XY} can be set to distinguish the signal from the background. We use $E_T^{miss} < 20$ GeV in data as the background control sample (detailed discussions are in Section 6.6) and optimize the expected limits on the production cross section for the d_{XY} cut. Figure 6.22 shows the average expected limit as a function of d_{XY} by scanning d_{XY} in Figure 6.21 [79]. With the scan sampling interval of 0.05 cm, using $c\tau$=5 cm as the worst case, and one can find the optimal cut on d_{XY} is at 0.6 cm.

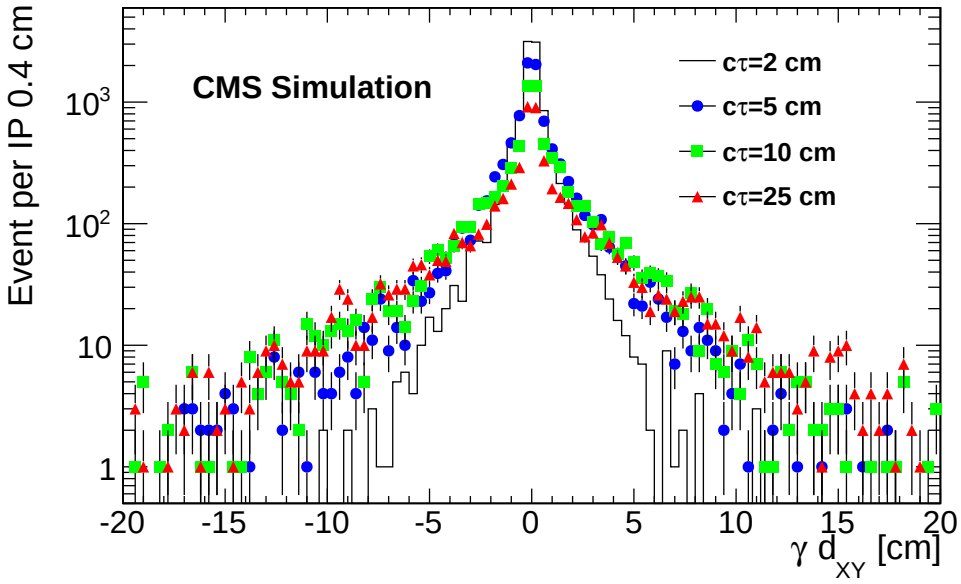

(a)

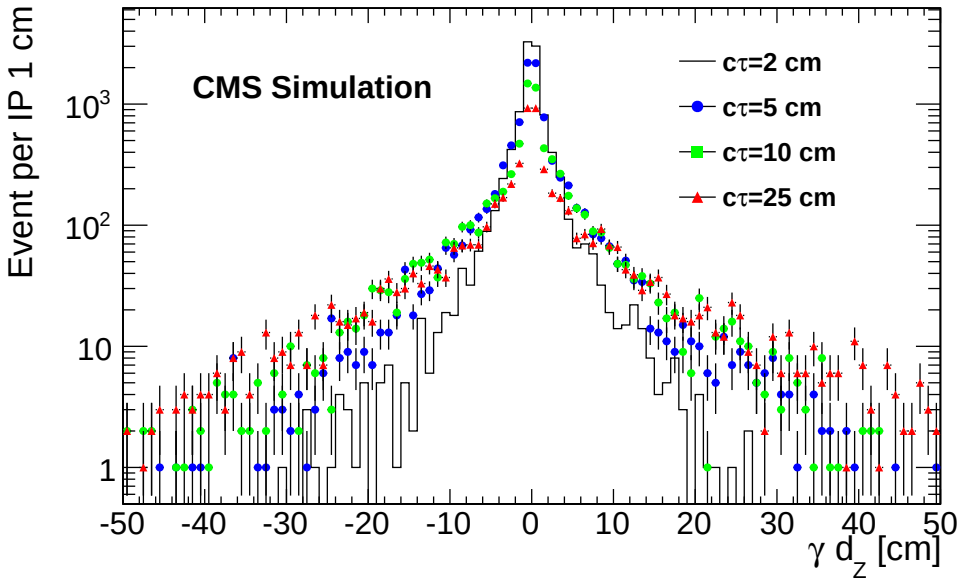

(b)

Figure 6.18: Reconstructed γ impact parameter from $\tilde{\chi}_1^0 \to \gamma + \tilde{G}$ decay, (a) transverse (b) longitudinal.

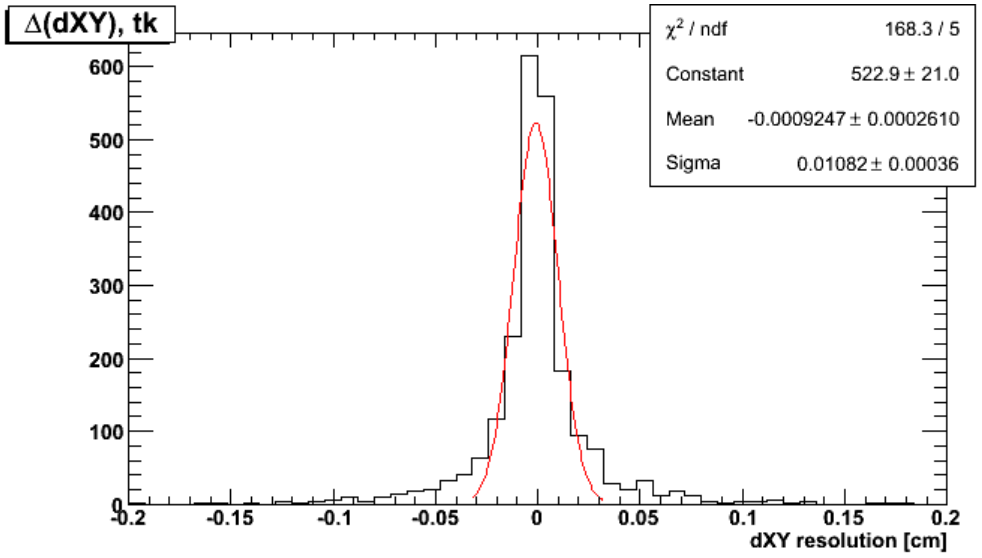

(a)

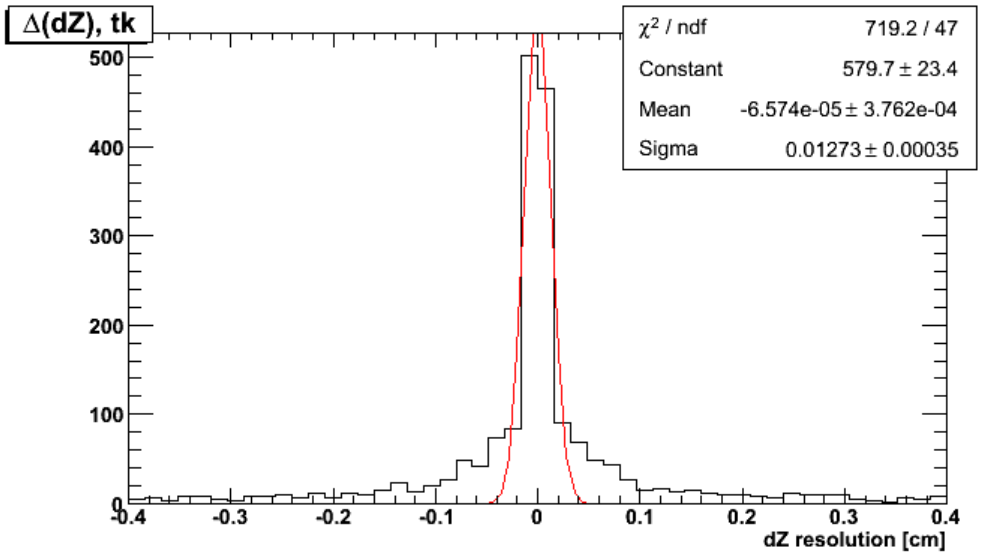

(b)

Figure 6.19: Reconstructed γ impact parameter resolution from $\tilde{\chi}_1^0 \to \gamma + \tilde{G}$ decay, (a) transverse (b) longitudinal.

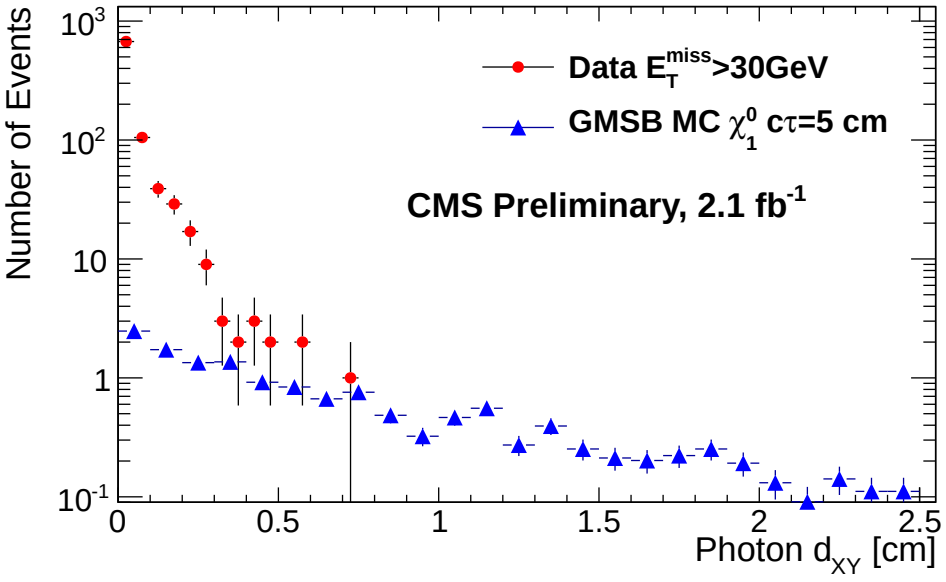

Figure 6.20: Transverse impact parameter distribution for data with $E_T^{miss} > 30$ GeV compared with signal simulation for $c\tau$ 5 cm normalized to the integrated luminosity of the data.

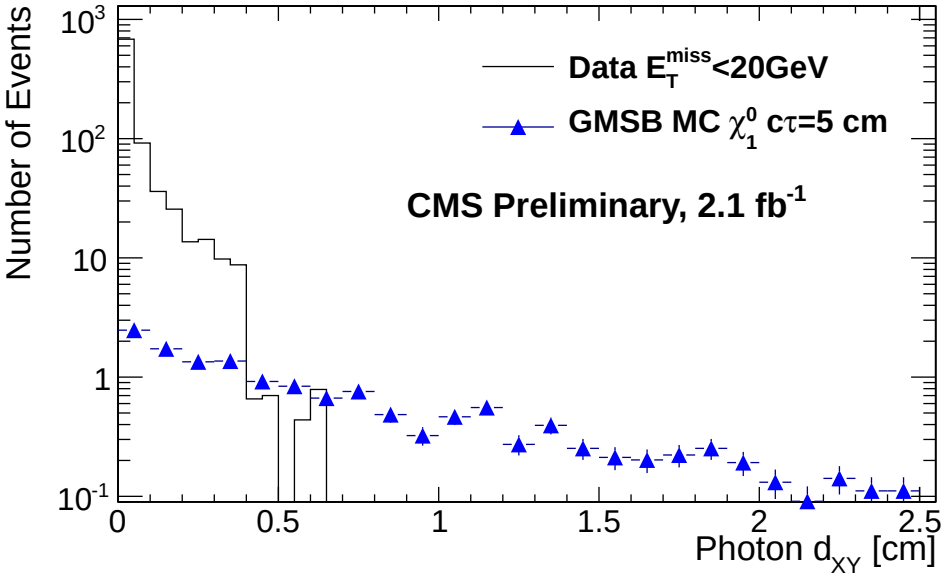

Figure 6.21: Transverse impact parameter distribution for data with $E_T^{miss} < 20$ GeV (background control region) compared with signal simulation for $c\tau = 5$ cm normalized to the integrated luminosity of the data.

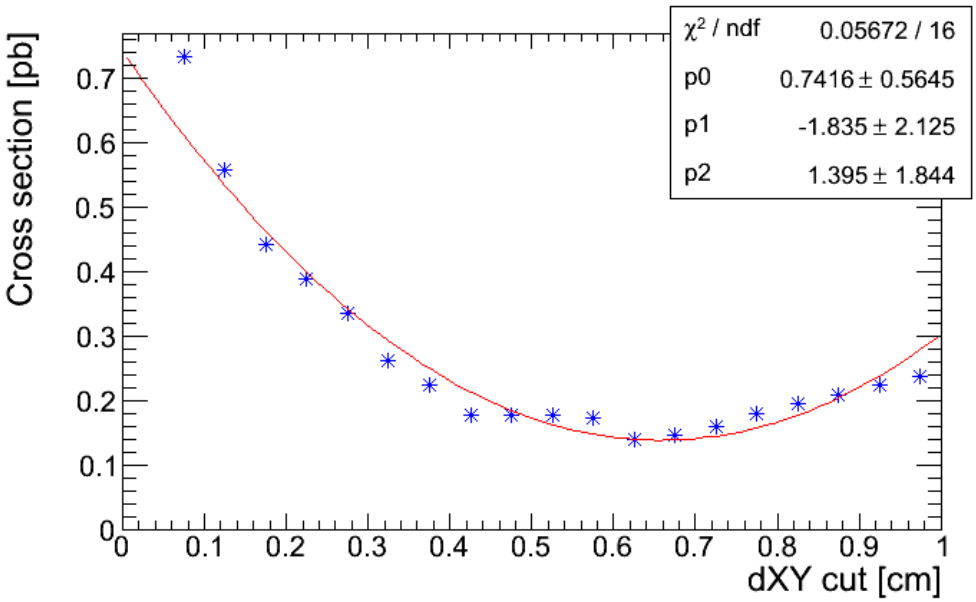

Figure 6.22: Average expected limits of cross sections as a function of d_{XY}. $\tilde{\chi}_1^0$ lifetime $c\tau$=5 cm for example.

6.5 Efficiency

6.5.1 Event selection cut flow

The effects of the event selections are illustrated in Table 6.3 for the $c\tau = 5$ cm simulation of 45,057 events, where every event has two neutralinos, each of which decays into a photon and a gravitino. The 2.1 fb^{-1} data sample is also listed in Table 6.3 [79] to illustrate the cut flow in data. The total fraction of remaining events for each step of the cut flow in data after the diphoton trigger is shown in Table 6.4 [79], sequentially. We can find out that, the photon selection step and the conversion selection step provide the largest reduction factors for data. After all selection cuts, the Monte Carlo signal sample has 711 events remaining for an overall event selection efficiency of 1.58%, and data have 1 event after all selections. Efficiencies for the four neutralino lifetimes are given in Table 6.5.

Table 6.3: Signal selection cut flow for $c\tau = 5$ cm and data.

Selection	Events in Monte Carlo	Events in Data
Total	45057	-
DiPhoton trigger	39988	1.8×10^7
Photon $E_T > 45$ GeV and $E_T > 30$ GeV	37398	4.9×10^6
Any ECAL barrel photon $E_T > 45$ GeV and Photon identification	27766	2.8×10^5
Jets $p_T > 80$ GeV and $p_T > 50$ GeV	26229	1.5×10^5
Conversion selection	1602	3554
$E_T^{miss} > 30$ GeV	1542	885
$d_{XY} > 0.6$ cm	711	1

Table 6.4: Data cut flow.

Selection cuts	Fraction of data after cut
Photon $E_T > 45$ GeV and $E_T > 30$ GeV	27.2%
Any ECAL barrel photon $E_T > 45$ GeV and Photon identification	1.55%
Jets $p_T > 80$ GeV and $p_T > 50$ GeV	0.831%
Conversion selection	0.020%
$E_T^{miss} > 30$ GeV	0.005%

The statistical error is about 3% to 5% of the selection efficiency.

$c\tau$ [cm]	2	5	10	25
Efficiency	0.921%	1.578%	1.797%	1.388%
Statistical errors	0.046%	0.059%	0.064%	0.055%

Table 6.5: Event selection efficiency vs $\tilde{\chi}_1^0$ lifetimes.

The event selection efficiency is independent of the neutralino mass for the mass in the order of 100 GeV. Taking $c\tau = 5$ cm for example, the event selection efficiency for neutralino masses of 140 GeV, 168 GeV, 196 GeV, 224 GeV and 252 GeV, respectively corresponding to Λ parameters of 100 TeV, 120 TeV, 140 TeV, 160 TeV and 180 TeV, is examined in Table 6.6 and the efficiencies of these mass points agree to within the statistical error $\sim 0.1\%$.

$\tilde{\chi}_1^0$ mass [GeV]	140	168	196	224	252
Efficiency	1.578%	1.612%	1.641%	1.667%	1.677%

Table 6.6: Event selection efficiency for different $\tilde{\chi}_1^0$ masses for the $c\tau = 5$ cm example.

6.5.2 Conversion Efficiency of Displaced Photons

This subsection discuss study the conversion reconstruction efficiency as a function of d_{XY} for displaced photons using Monte Carlo samples.

6.5.2.1 Conversion Efficiency as a Function of d_{XY}

The conversion reconstruction efficiency is defined as: the denominator is the number of photons; the numerator is the number of converted photons with recon-

structed conversions. On the average, the conversion reconstruction efficiency itself is about 4% (Figure 6.23 and Figure 6.24), and the signal event selection efficiency is about 1% to 2% after all the above trigger requirements and the selection cuts (Table 6.5 [79]). From the efficiency distribution and Figure 6.18(a), the sensitive d_{XY} region can be observed; for example, for the $c\tau = 2$ cm sample has a sensitive area of $|d_{XY}| < 5$ cm, and the $c\tau$ 25 cm sample is sensitive up to $|d_{XY}| < 15$ cm.

6.5.2.2 Efficiency in pile-up conditions

Two of the three conversion reconstruction algorithms, the tracker-only and ECAL-seeded algorithms, are not affected much by the pile-up condition, but the GSF electron algorithm has some efficiency loss when the number of pile-up vertices reaches 5 or above because of the electron identifications. The comparison of efficiency in low and high pile-up condition shows some difference for small d_{XY} (Figure 6.25). Also, for large d_{XY}, the high pile-up condition reduces the efficiency by $\sim 40\%$. However, the efficiency of the d_{XY} cut is negligibly affected by the pile-up conditions, within statistical errors (Figure. 6.26). The efficiency calculation in Table 6.5 includes the pile-up effect in the Monte Carlo samples, and the conversion reconstruction efficiency of photons from $Z \to \mu\mu\gamma$ cross-checks the calculation in data. In the conversion reconstruction efficiency studies using $Z \to \mu\mu\gamma$, the Monte Carlo samples have the same pile-up profile as in GMSB samples. Also, both $Z \to \mu\mu\gamma$ and GMSB Monte Carlo should be reweighted to the same pile-up profile of 2011 collision data, so that the pile-up effect of efficiency has been included.

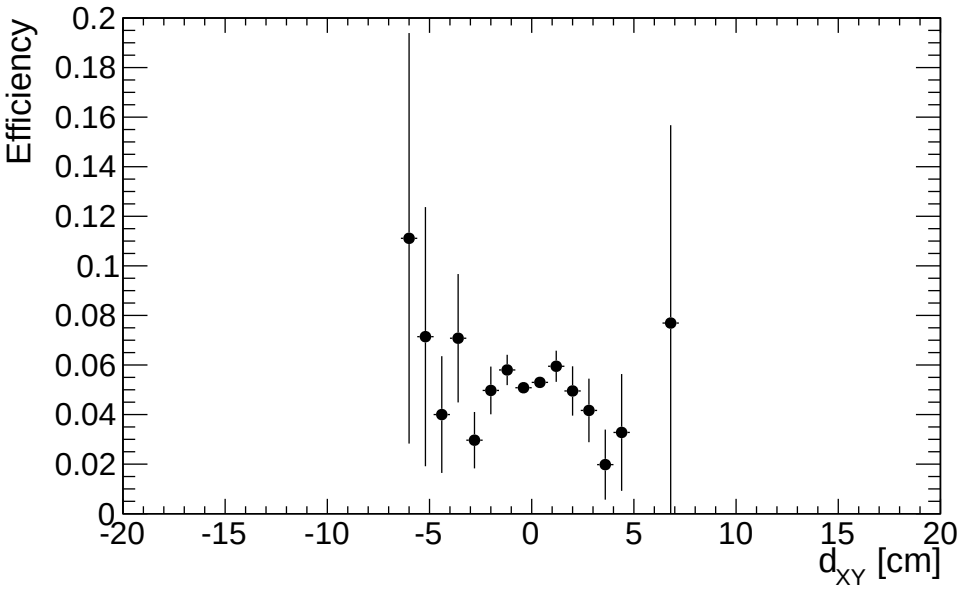

(a)

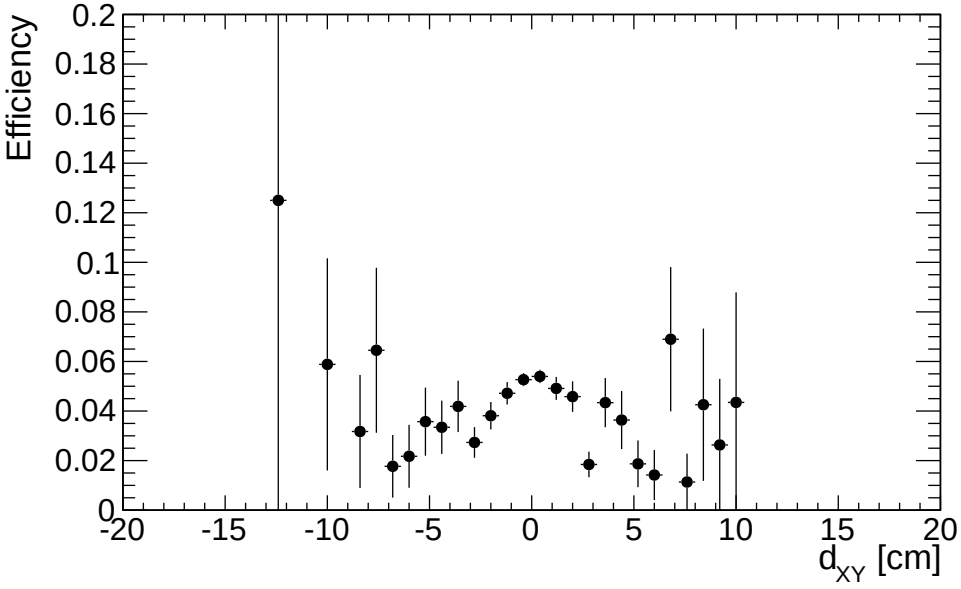

(b)

Figure 6.23: Conversion reconstruction efficiency for different $\tilde{\chi}_1^0$ lifetimes (a) $c\tau$=2 cm (b) $c\tau$=5 cm .

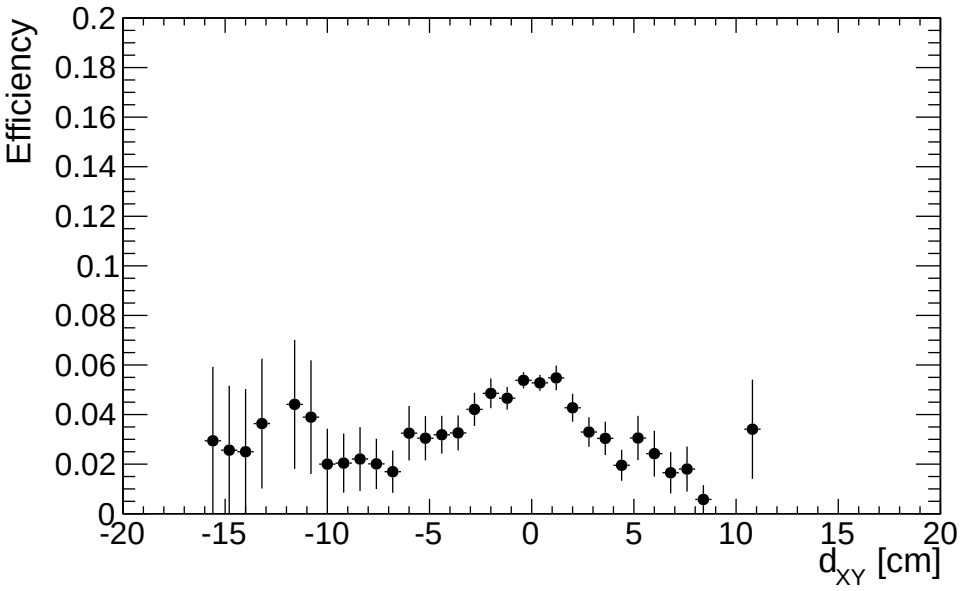

(a)

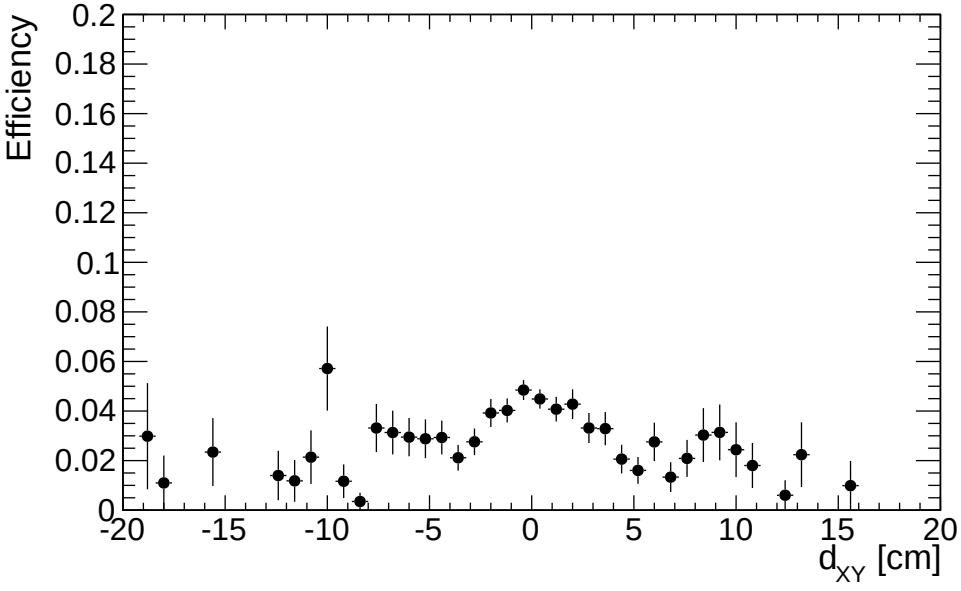

(b)

Figure 6.24: Conversion reconstruction efficiency for different $\tilde{\chi}_1^0$ lifetimes (a) $c\tau$=10 cm (b) $c\tau$=25 cm.

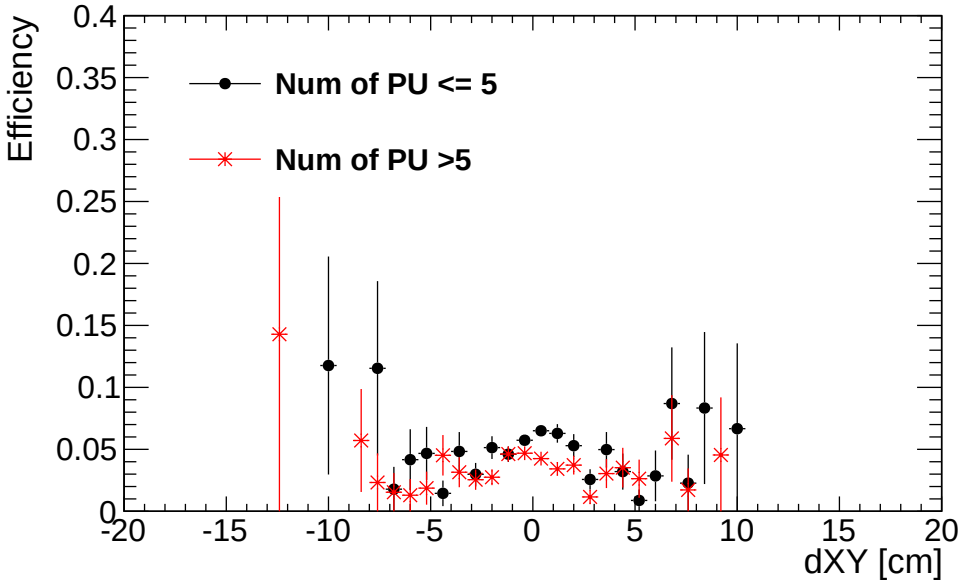

Figure 6.25: Conversion reconstruction efficiency for different pile-up conditions. $\tilde{\chi}_1^0$ lifetime $c\tau$=5 cm for example. (a) number of pile-up vertices ≤ 5 (b) number of pile-up vertices > 5.

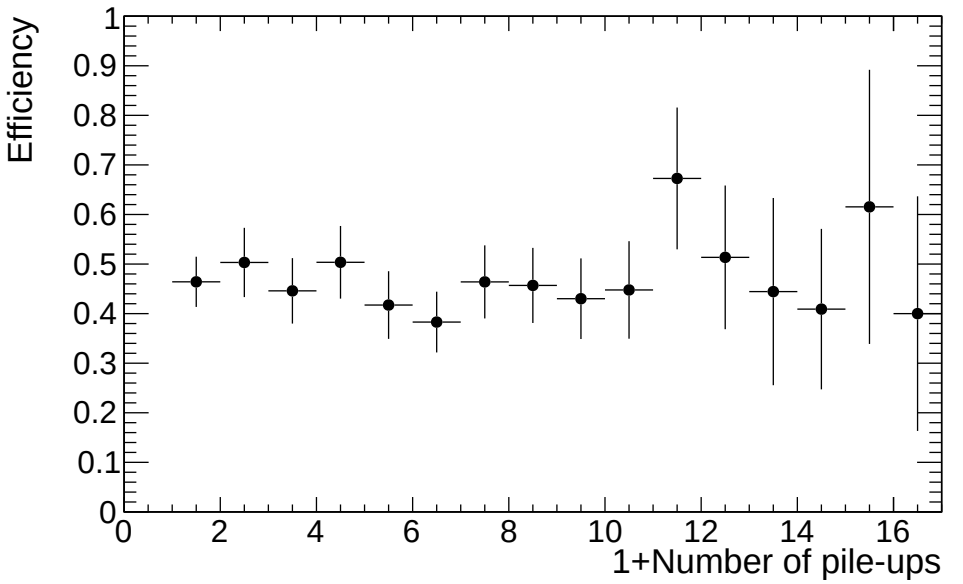

Figure 6.26: Relative efficiency of $d_{XY} > 0.6$ cm cut with respect to the previous cut, as a function of the the number of pile-up vertices for the $\tilde{\chi}_1^0$ lifetime $c\tau$=5 cm example.

6.6 Estimation of background

6.6.1 Data-driven background

Because of the γ's and jets in the final state, the background is due to single-γ-plus-jets events and QCD multi-jets event with no true large E_T^{miss}. In single-γ-plus-jets events, the energetic photons are the final state photons. And in QCD multi-jets events, the jets can be misidentified as photons, e.g. "fake photons". The strategy for determining the background is to use control samples which are kinematically similar to the candidate sample while having no real E_T^{miss}. Therefore we use the following data-driven method for the background estimation.

The $\tilde{\chi}_1^0 \to \gamma + \tilde{G}$ decay has two signatures: E_T^{miss} from the unseen $\tilde{G}$ and large transverse IP from the displaced photons. Therefore the $\tilde{\chi}_1^0$ signal has large E_T^{miss}, while the background (single-γ-plus-jets and QCD multi-jets) has small E_T^{miss} with tails extending to high E_T^{miss}. We construct a control region of low E_T^{miss}, which then is used to estimate the background in the search region by comparing the d_{XY} distributions. Thus, the data are separated into low E_T^{miss} (as the background region) and high E_T^{miss} (as the signal region). We use the low E_T^{miss} region for background estimation, and the high E_T^{miss} region for the signal search.

For example, in this analysis, we define $E_T^{miss} < 20$ GeV as the background control region, and the $E_T^{miss} > 30$ GeV as the signal region. The d_{XY} distribution of the $E_T^{miss} < 20$ GeV background region is compared with the $E_T^{miss} > 30$ GeV signal region. The two distributions are superimposed, then normalized to the total number of conversions and re-weighted by the conversion vertex χ^2 probability. The conversion vertex χ^2 probability distributions of the two regions are shown in Figure 6.27. A selection cut on d_{XY} can be set by optimizing the expected limit on the cross section,

and the number of background events can be estimated by applying this d_{XY} cut on the d_{XY} distribution for the background region. Together with the statistical errors, the uncertainties on the number of background events should come from the d_{XY} cut resolution.

The estimation of the background from the low E_T^{miss} control region assumes that the photon d_{XY} distribution is independent of E_T^{miss}, which can be demonstrated by using the "fake photons" as control samples.

6.6.2 Fake photons for background estimation

To ensure that the low E_T^{miss} background control samples can be used to estimate the actual background, fake photons are used as control samples for the background estimation.

Photon-like signals, referred to as "fake photons," have similar selection criteria as isolated photons, but they do NOT satisfy at least one of the following photon isolation criteria:

- ECAL E_T in the ECAL isolation cone $< 0.006 \cdot E_T + 4.2$ GeV ;
- HCAL E_T in HCAL isolation cone $< 0.0025 \cdot E_T + 2.2$ GeV ;
- E_T of the tracks in the track isolation cone $< 0.001 \cdot E_T + 2.0$ GeV ;

The electron veto is required and under the same definition as in the signal photon selections. These "fake photons" objects are electromagnetically fluctuated jets or photons from π^0 decays.

The reconstructed photon d_{XY} distributions for isolated photons and fake photons are shown in Figure. 6.28. If the photon d_{XY} resolution is independent of E_T^{miss}, and

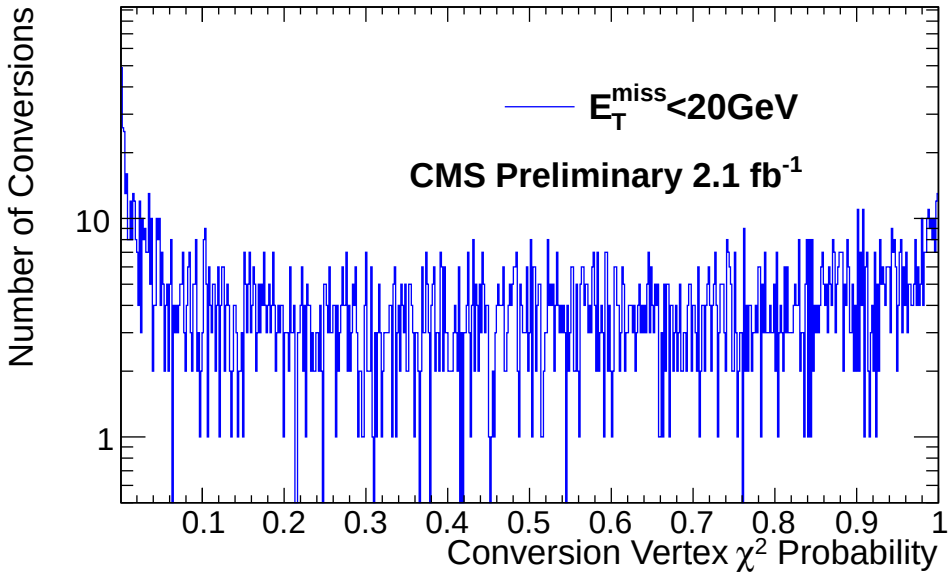

(a)

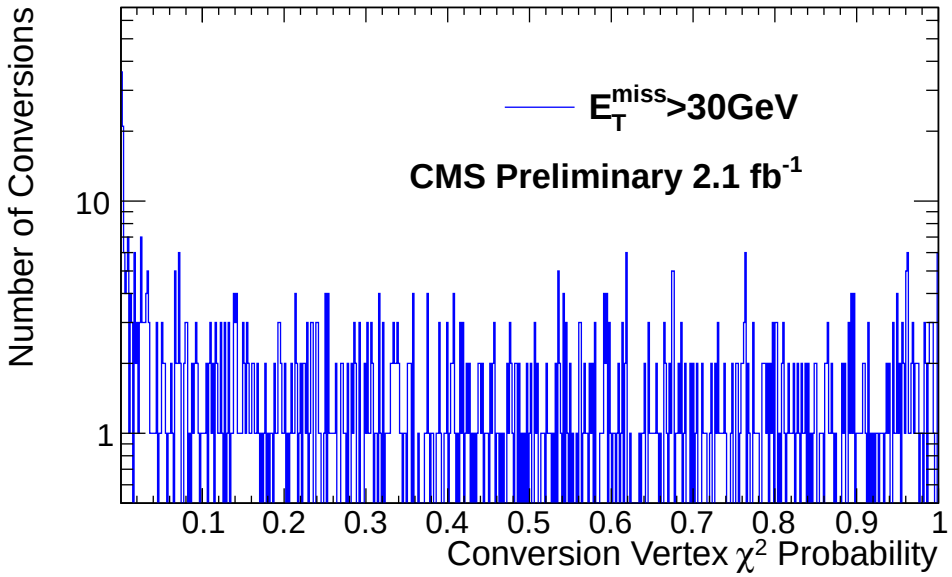

(b)

Figure 6.27: Converted isolated photon vertex χ^2 probability in 2011 7 TeV data (a) $E_T^{miss} < 20$ GeV background region (b) $E_T^{miss} > 30$ GeV signal region.

the fake photons have the same d_{XY} resolution as the isolated photons, the $E_T^{miss} < 20$ GeV region from data can be used to predict the background. In other words, the photon d_{XY} distribution should be comparable for low E_T^{miss} and high E_T^{miss}, and the d_{XY} distribution of isolated photons should be comparable to the fake photons. In this way we can confirm that the low E_T^{miss} region from data can be used to predict the background.

6.6.2.1 Fake-fake comparison

Pure fake photons are selected, and separated into low E_T^{miss} (background region) and high E_T^{miss} (signal region). The conversions of fake photons can be either from true photons in π^0 decays with conversion vertex χ^2 probability from 0 to 1, or totally random combinations of track pairs, which give conversion vertex χ^2 probability ~ 0. For example, for 2011 7 TeV data, there are many conversion vertices with very low χ^2 probability around $E_T^{miss} = 20$ GeV (Figure 6.29). The d_{XY} resolution is strongly dependent on the conversion vertex χ^2 probability, and as a result, the worse χ^2 probability gives worse vertex position resolution, leading to worse d_{XY} resolution. The d_{XY} distribution for low E_T^{miss} (background region) is re-weighted by the conversion vertex χ^2 probability, conversion by conversion. The photon d_{XY} vs the conversion vertex χ^2 probability is shown in Figure. 6.30 for 2011 7 TeV data.

By comparing the fake photon d_{XY} distributions in these two regions (Figure6.31 [79]), one can make sure that the d_{XY} resolution of fake photons does not depend on E_T^{miss}. The photon d_{XY} distribution is comparable for fake photons, both in the signal and background regions.

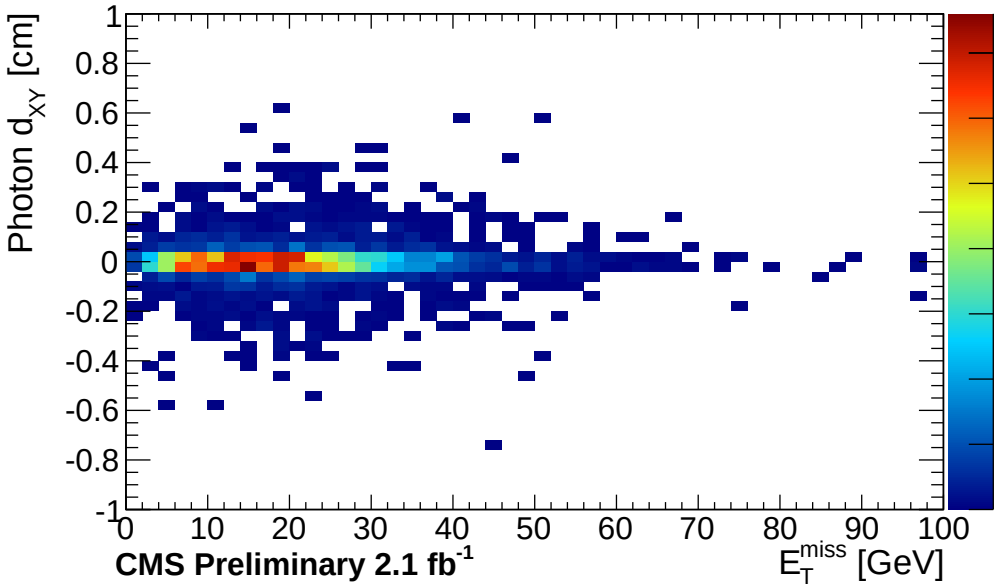

(a)

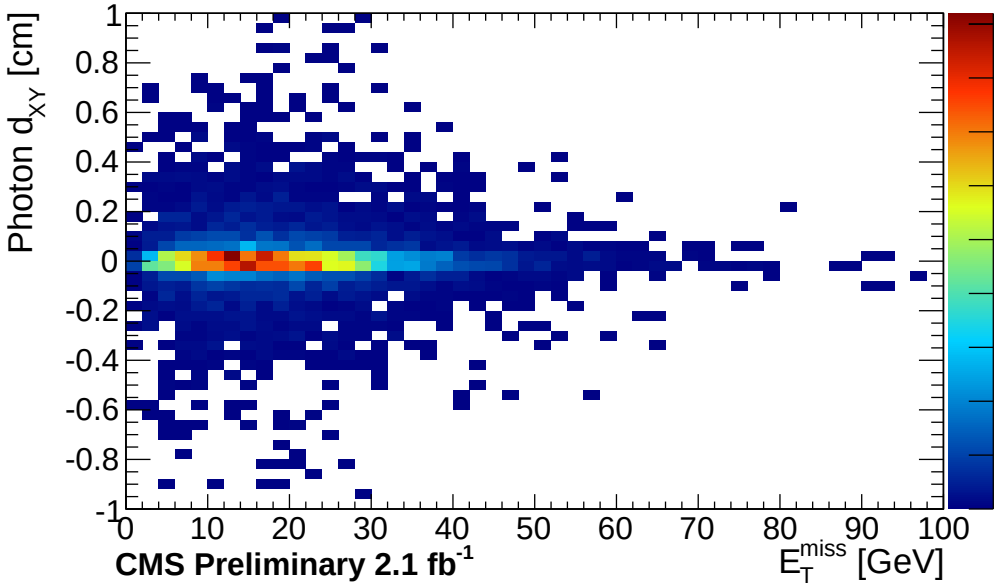

(b)

Figure 6.28: Reconstructed γ transverse impact parameter d_{XY} vs E_T^{miss} in 2011 7 TeV data (a) isolated photons (b) fake photons.

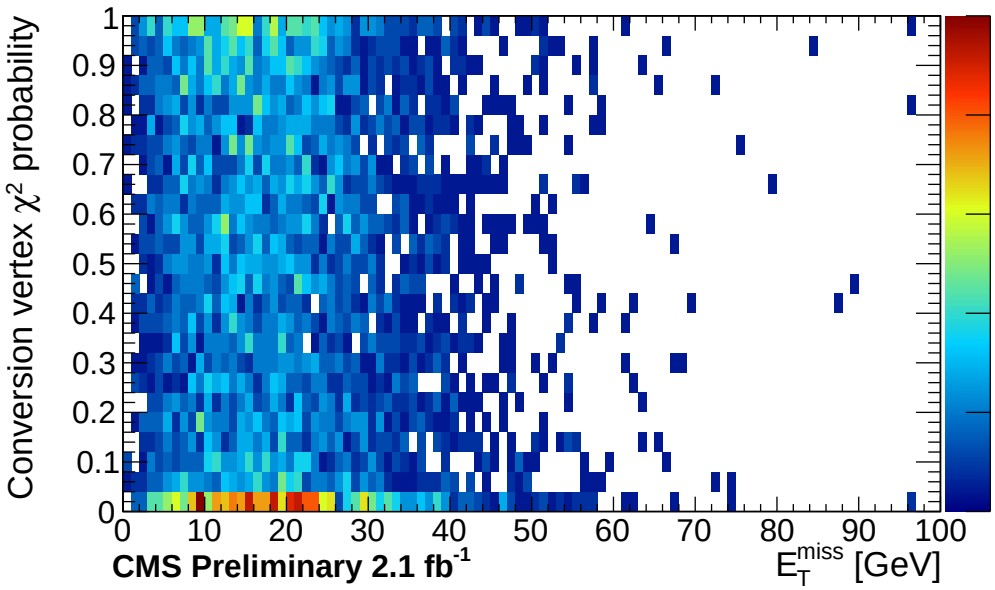

(a)

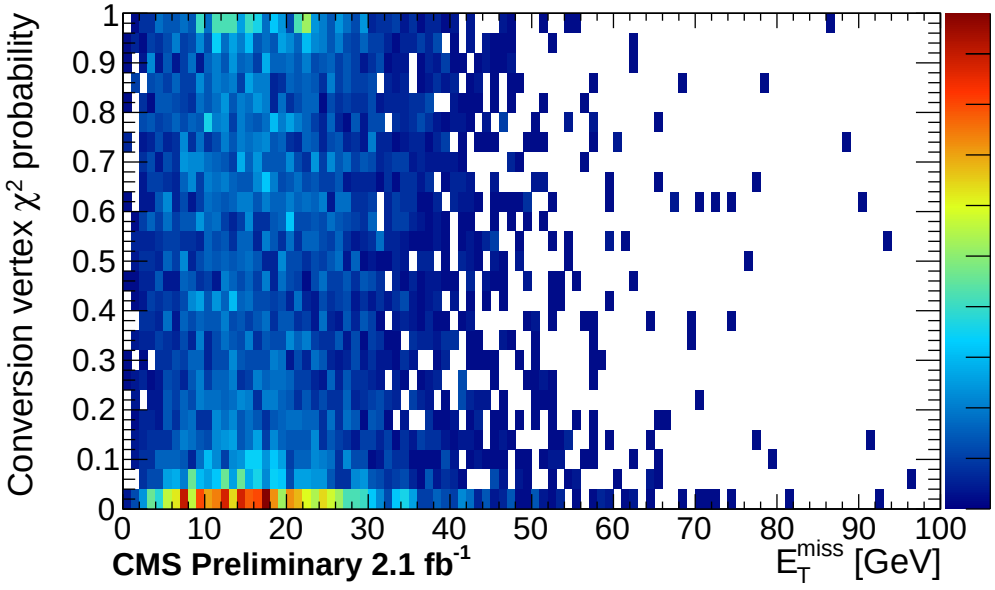

(b)

Figure 6.29: Reconstructed photon conversion vertex χ^2 probability vs E_T^{miss} in 2011 7 TeV data (a) isolated photons (b) fake photons.

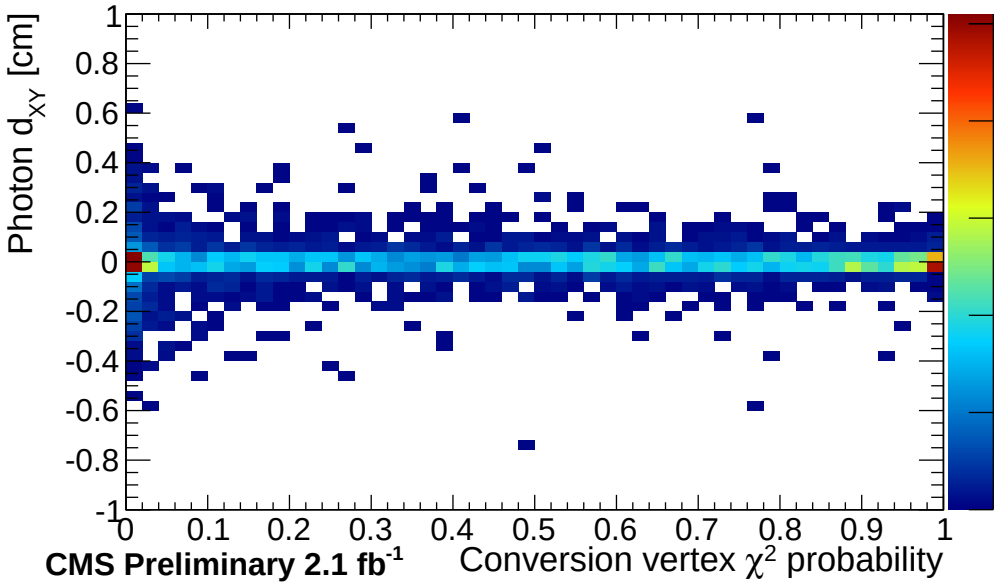

(a)

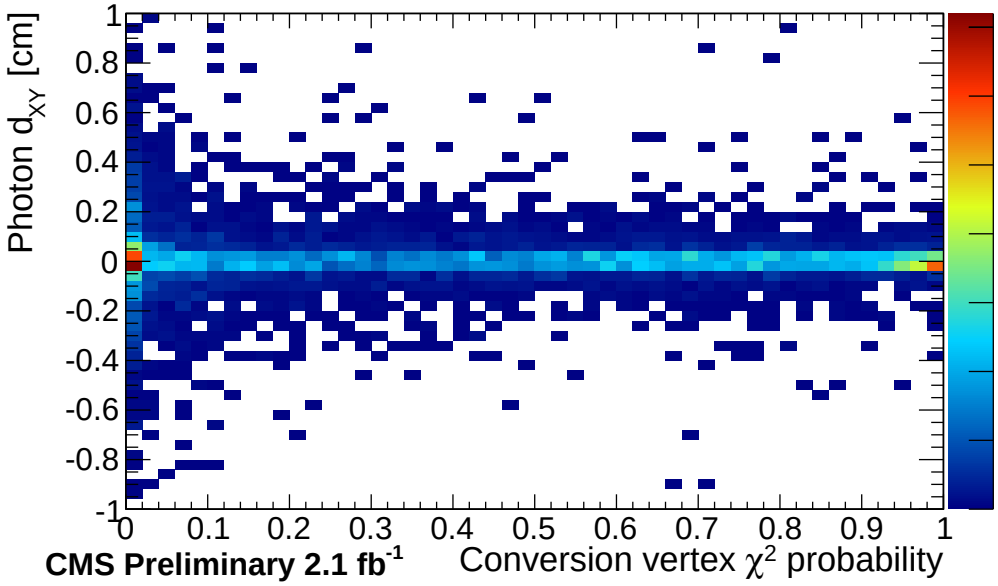

(b)

Figure 6.30: Reconstructed photon d_{XY} vs conversion vertex χ^2 probability in 2011 7 TeV data (a) isolated photons (b) fake photons.

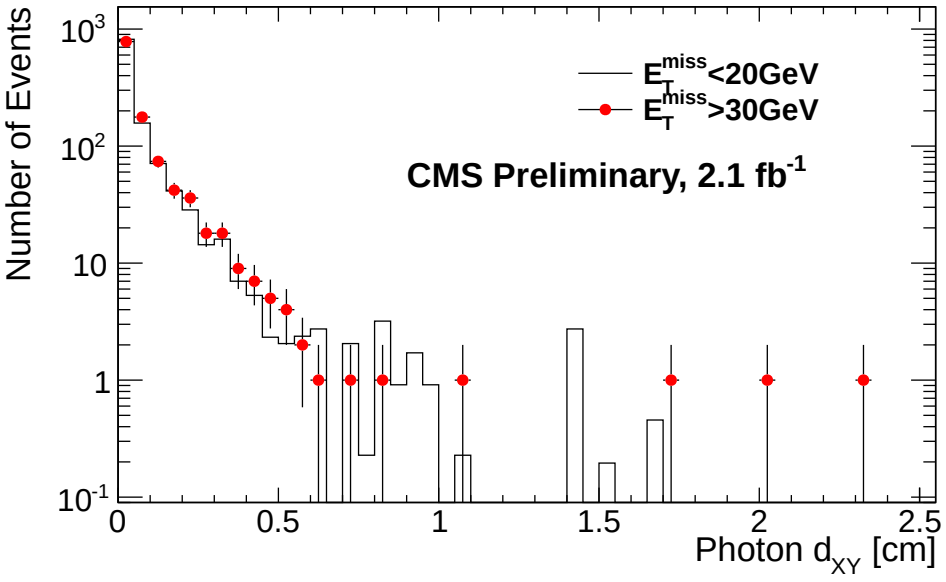

Figure 6.31: Photon d_{XY} comparison for fake photons in background and signal region.

6.6.2.2 Isolated photons vs fake photons comparison

The d_{XY} distributions of isolated photons and fake photons in the low E_T^{miss} region is normalized to the pure fake photons in low E_T^{miss} by the total number of conversions, and also re-weighted by the conversion vertex χ^2 probability for the same reason as above (Figure6.32 [79]). With no significant excess, we can confirm that the isolated photon d_{XY} is comparable with the fake photon d_{XY} in the background region.

From the two comparisons of the fake photons, we can confirm that the $E_T^{miss} <$ 20 GeV can be used to estimate the background.

6.6.3 Background events

By normalizing the data-driven background ($E_T^{miss} <$ 20 GeV) to the signal region by the total number of conversions, and re-weighting by the conversion vertex

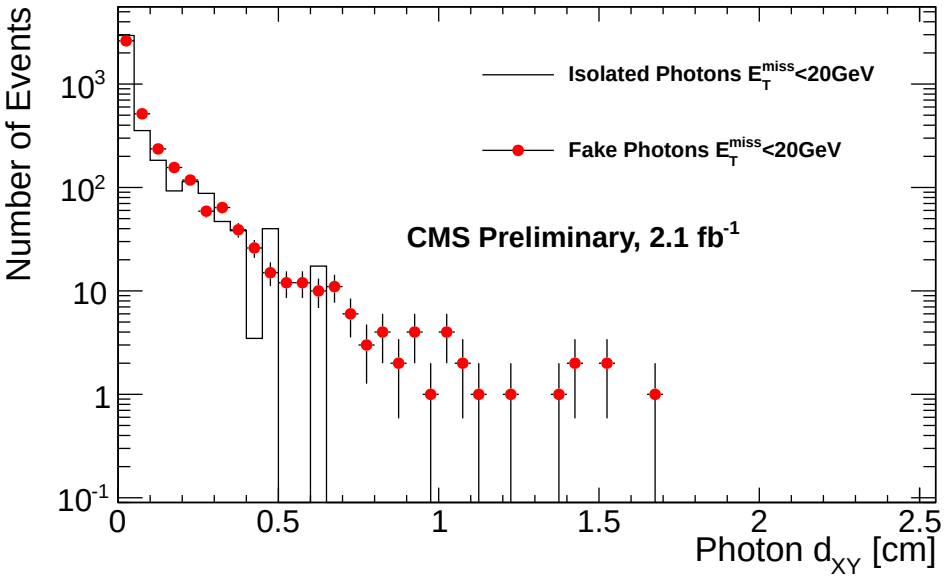

Figure 6.32: Photon d_{XY} comparison for isolated and fake photon distributions in background region.

χ^2 probability for the same reason as above, a cut on the transverse impact parameter $d_{XY} > 0.6$ cm is applied to the background region $E_T^{miss} < 20$ GeV, giving an estimate of the total background of $0.78^{+1.25}_{-0.48}$ events (Figure 6.33 [79]), by applying the normalization factor 0.78 to the background of $1.00^{+1.62}_{-0.62}$ event from the background region $E_T^{miss} < 20$ GeV before the normalization and using Poisson statistical errors. The uncertainty on the background estimation comes from statistical uncertainty in the control region ($E_T^{miss} < 20$ GeV).

6.7 Systematic Uncertainties

For systematic uncertainties, the following sources are considered:

- Conversion reconstruction efficiency
- Photon d_{XY} uncertainties

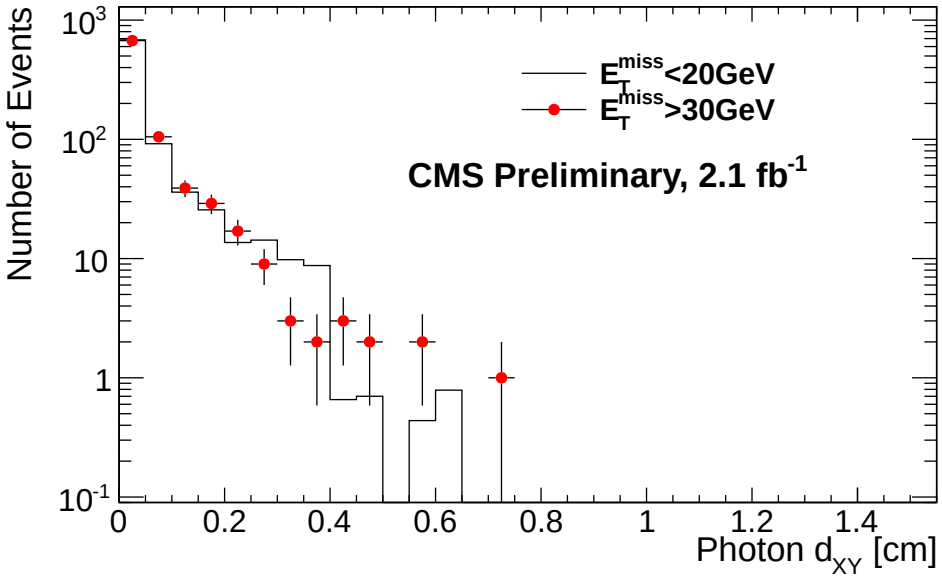

Figure 6.33: d_{XY} distribution: background region compared to the signal region.

- Electron veto uncertainty
- Photon ID efficiency
- Pile-up effect
- The error on integrated luminosity
- Signal under $E_T^{miss} < 20$ GeV
- E_T^{miss} error and jet selection error

The systematic uncertainty on the conversion reconstruction efficiency (20.6%) has already been considered in Section 5.8. The following subsections describe the rest of the uncertainties.

6.7.1 Transverse impact parameter resolution uncertainty

By comparing the photon d_{XY} distribution in $Z \to \mu\mu\gamma$ decays for data and Monte Carlo (Figure. 6.34), good agreement of d_{XY} resolution at 0.06 cm is observed. By counting the events of the signal Monte Carlo in $d_{XY} = 0.6 \pm 0.06$ cm, we can set the uncertainty at less than 0.5% for signal selection. The tails of the resolution distribution are from the conversion vertex position resolution, which has been discussed previously in Section 6.6.

6.7.2 Electron veto uncertainty

In photon identification, the electron veto is applied using the pixel-match. To keep the conversions using GSF electron algorithm, an additional check is applied to examine if the pixel-match electron is from conversions. In MC samples of $Z \to \mu\mu\gamma$, the conversion-keeping check recovers 44 more photons than the standard pixel-match with 7197 photons in total. The contribution to the total uncertainty is less than 0.1%.

6.7.3 Other sources of uncertainties

The other sources of uncertainties are due to four sources:

- Integrated luminosity (4.5%);
- Jet p_T/E_T^{miss} selection cut;
- Photon identification;
- Other sources such as signal contribution in the $E_T^{miss} < 20$ GeV background region.

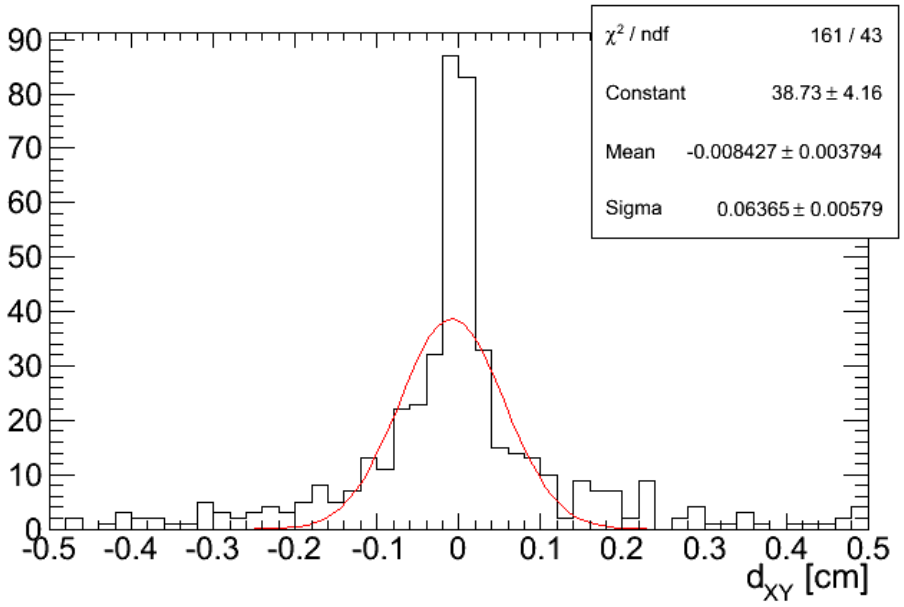

(a)

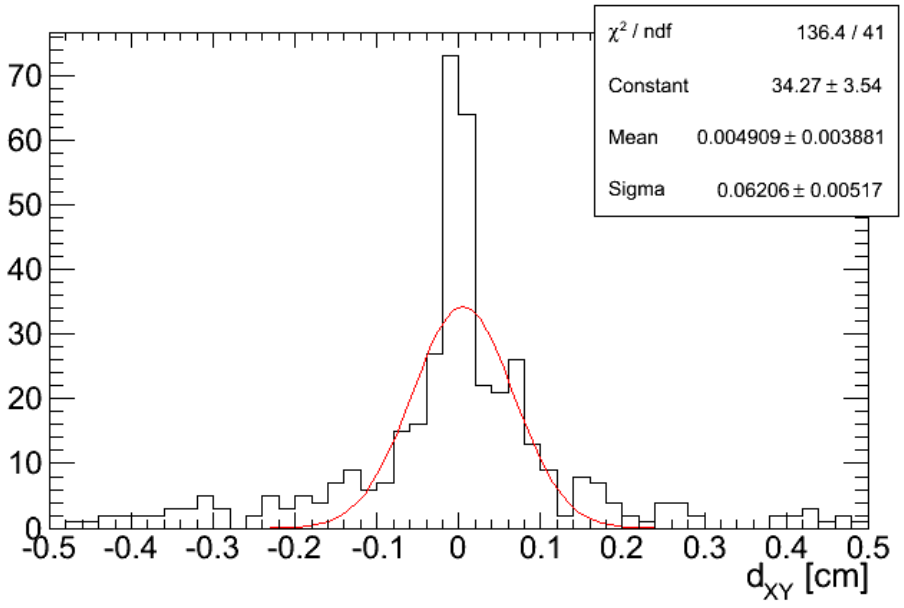

(b)

Figure 6.34: Photon d_{XY} in $Z \to \mu\mu\gamma$ decays (a) in Drell-Yan Monte Carlo samples (b) in data samples

For the 1% jet energy scale uncertainties [49] on the jet energy cut of $p_T > 80$ GeV and $p_T > 50$ GeV, the ± 0.8 GeV error is applied to the jet selection, which gives a negligible uncertainty on the event selection of less than 0.5%. THe E_T^{miss} energy scale uncertainty is 1% [76] as well, and the ± 0.3 GeV error is applied to the E_T^{miss} selection, which gives an uncertainty of less than 0.1%.

The photon efficiency data-MC scale is studied in Ref [4], which includes three sources of uncertainties from the pile-up (2.5%), photon Data/MC scale (2.6%) and photon ID (0.5%). This gives a resulting scale factor of $\epsilon_e^{data}/\epsilon_e^{MC} = 0.953 \pm 0.014(stat.) \pm 0.068(syst.)$.

- The effect of pile-up on the scale factor is studied by comparing the efficiency ϵ_e^{data} and ϵ_e^{MC} for data and MC versus the number of primary vertices (N_{PVX}) in the event.

- The photon Data/MC scale factor $\epsilon_e^{data}\epsilon_e^{MC}$ is compared for photon E_T, η, $\Delta R_{\gamma/jet}$ and N_{jets}.

- Because of electron bremsstrahlung, the electron efficiency is different from the photon efficiency. A comparison [82] of the MC electron efficiency using $Z \to ee$ samples and the MC photon efficiency using a γ+jet sample has been performed for to determine the photon identification uncertainty.

From the signal Monte Carlo samples shown Figure 6.3(a), the amount of signal events with $E_T^{miss} < 20$ GeV is less than 1%. With the normalization to data by the integrated luminosity, it gives negligible contribution to the total uncertainty of background. Also, other sources of uncertainties can be considered as negligible when compared to the conversion reconstruction efficiency uncertainties.

Source of Uncertainty	Uncertainty (%)
Integrated luminosity	4.5
Jet p_T/E_T^{miss} energy scale	< 0.5
Pile-up	2.5
Photon identification Data/MC scale	2.6
Photon-electron difference	0.5
Conversion reconstruction efficiency	20.6
Photon d_{XY} resolution	< 0.5
Total	25

Table 6.7: Summary of systematic uncertainties.

By considering all the above sources (Table 6.7 [79]), the total systematic uncertainty is determined to be 25%.

6.8 Results

The estimated background is $0.78^{+1.25}_{-0.48}$ events. We determine the upper limits for the cross section for pair-production of neutral particles, each of which decays into one photon and invisible particles. A CLs limit setting method [83, 84] is employed using the log-normal model, to incorporate uncertainties on the total background, the integrated luminosity, and total acceptance times efficiency. The observed 95% confidence level limits vary between 0.12 and 0.24 pb, depending on the neutral particle lifetime (Table 6.8 [79] and Figure 6.35 [79]):

There is one observed event that satisfies the selection criteria has $d_{XY} = -0.74$ cm and $E_T^{miss} = 44.9$ GeV. The momenta of the converted photon are highly imbalanced.

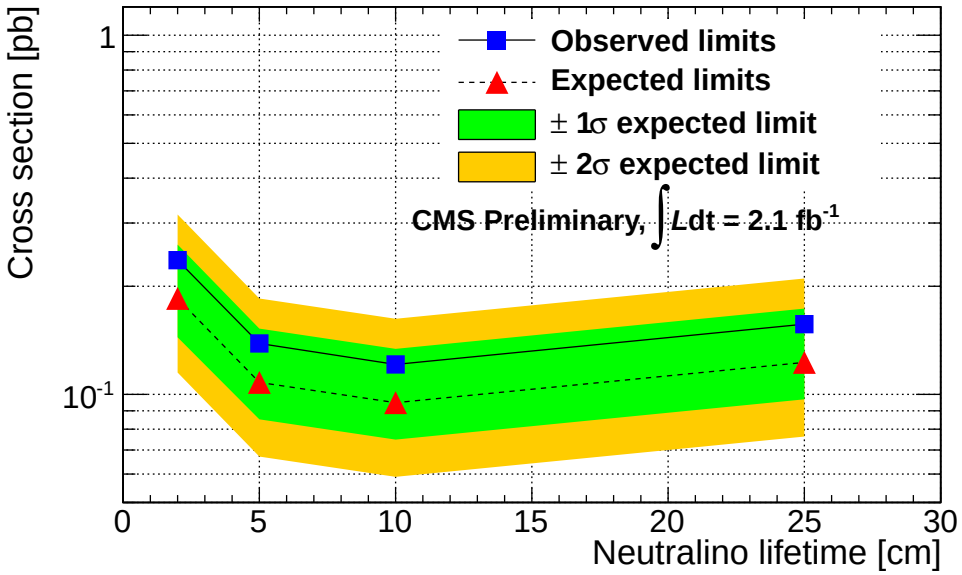

Figure 6.35: 95% C.L. upper limits on the pair-production cross section for neutral particles, each of which decays into a photon and invisible particles, as a function of neutralino lifetime.

The converted photon consists two tracks: one from the GSF electron algorithm with p_T = 93.5 GeV; the other from the general track algorithm with p_T = 0.8 GeV. The event display for different views shown in Figs. 6.36, 6.37 6.38 and 6.39 are made using Fireworks [85], and the two tracks are colored in red in the direction of 7 o'clock. The E_T^{miss} is shown as a red arrow pointing up in Figure 6.37 and point to the direction of 1 o'clock in Figure 6.36. The reconstructed photon for this conversion has a transverse energy E_T of 83.8 GeV.

6.9 Interpretation

Upper limits on the cross section for pair-production of $\tilde{\chi}_1^0$s, each of which decays into a photon and invisible particles, are calculated as a function of the $\tilde{\chi}_1^0$

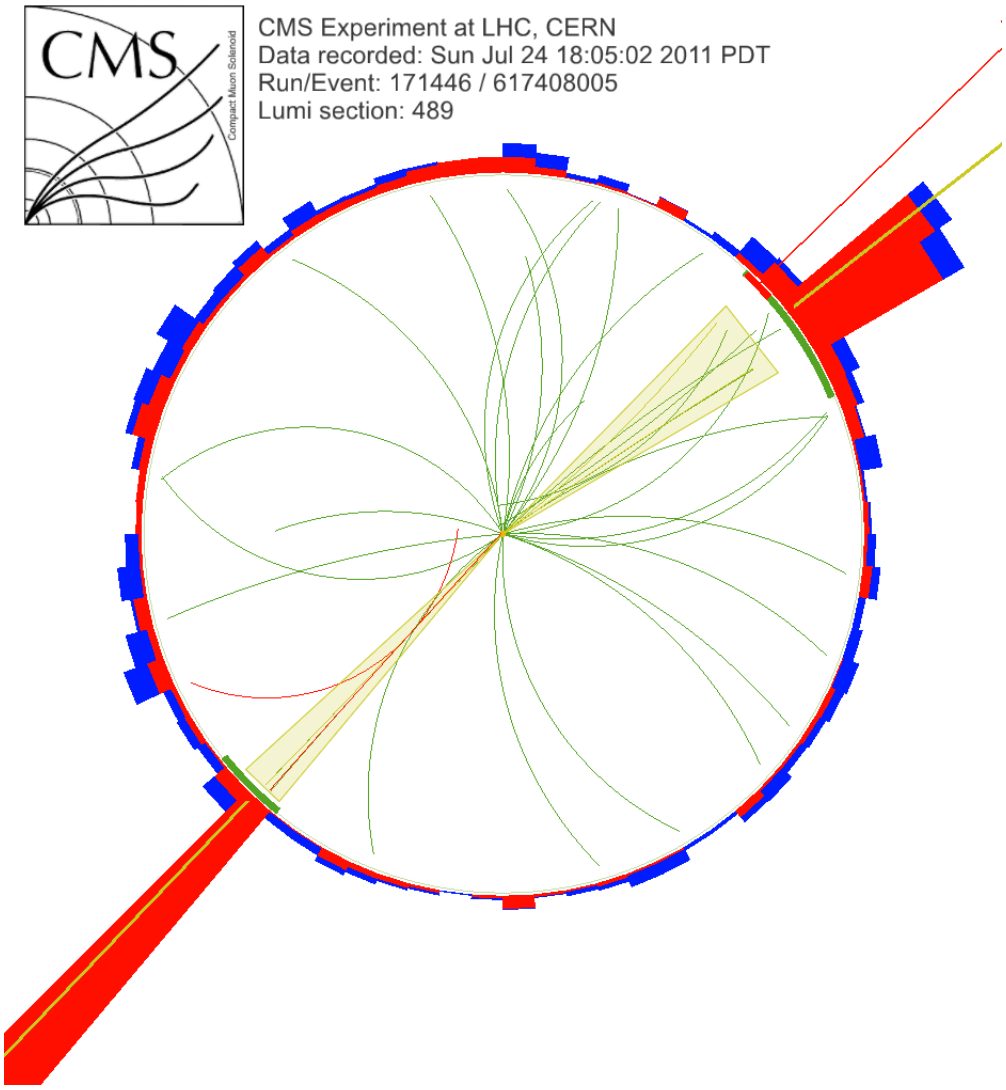

Figure 6.36: r-ϕ view of the observed event.

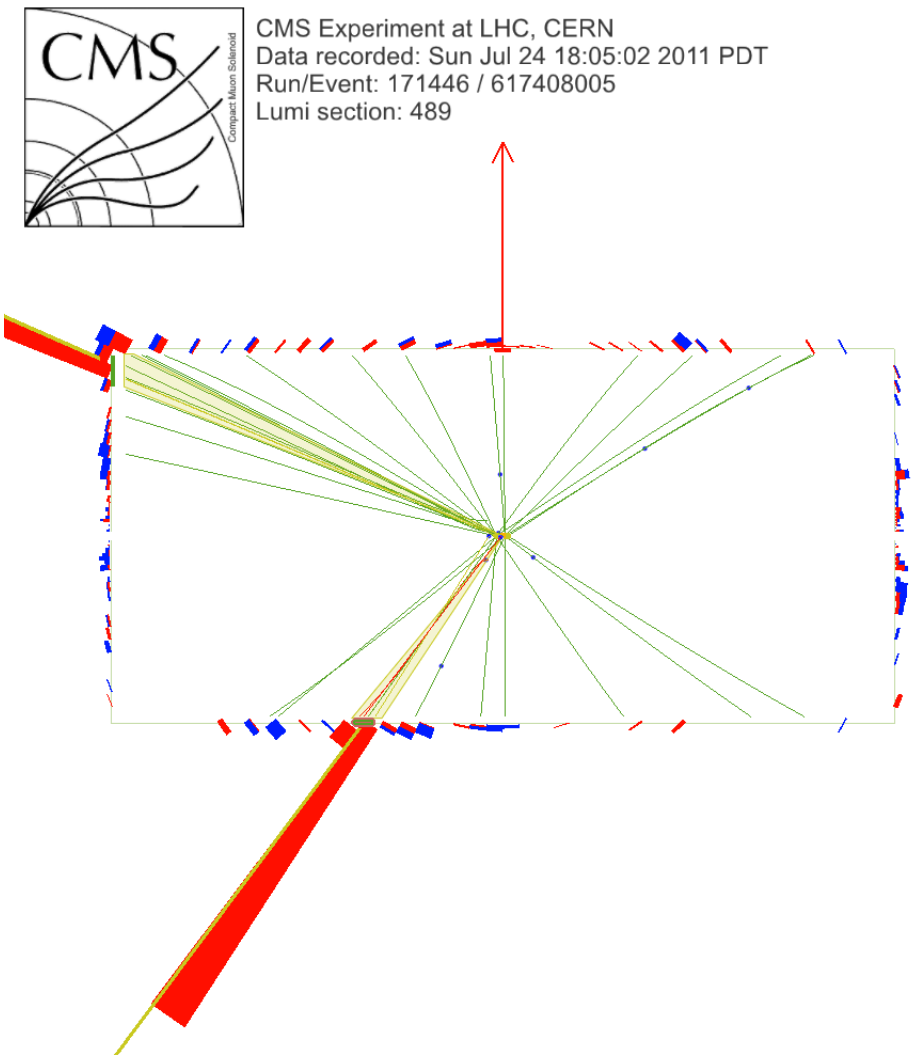

Figure 6.37: r-z view of the observed event.

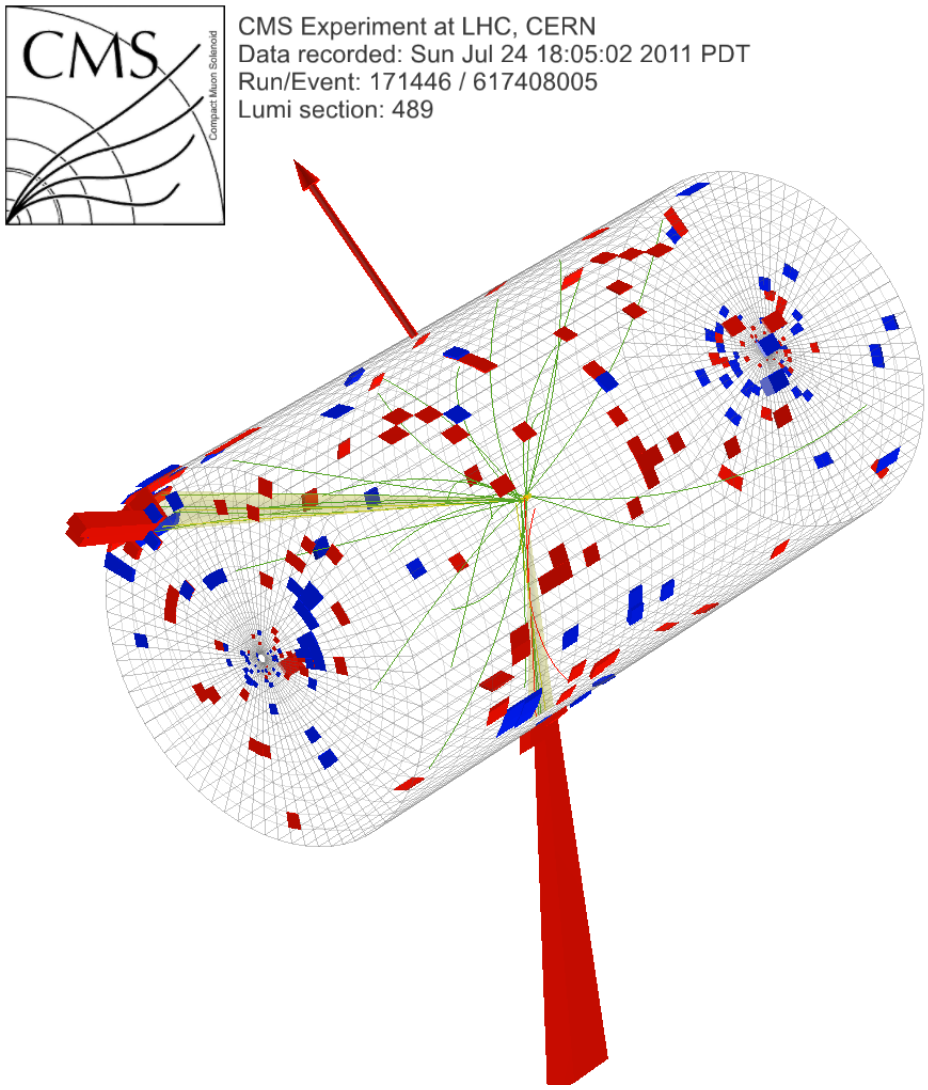

Figure 6.38: 3-D view of the observed event.

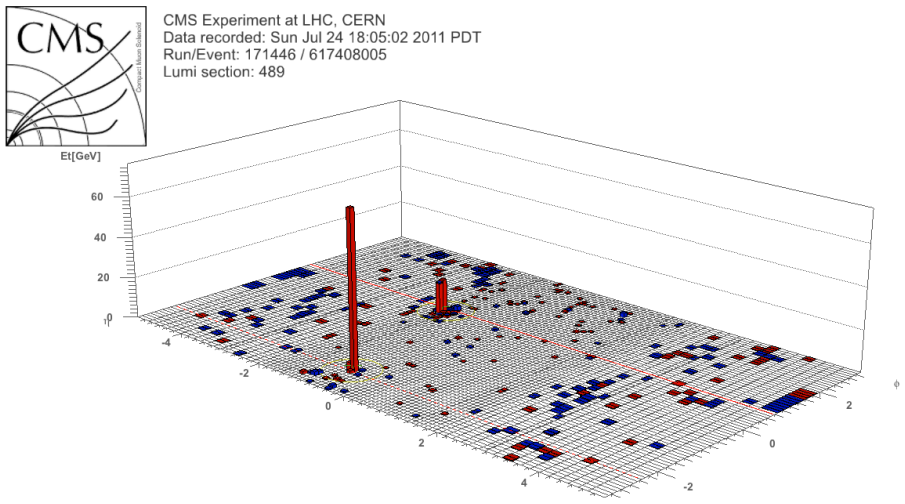

Figure 6.39: Lego view of the observed event.

lifetime. The limits are model-independent and they can interpreted using different models, for example, some Hidden Valley [68] models. It can also be interpreted using some low scale gauge mediation scenarios [28] where two $\tilde{\chi}_1^0$ are from a Higgs boson $H \to \tilde{\chi}_1^0\tilde{\chi}_1^0$, each of which decays into a photon and a gravitino.

In the minimal GMSB model, the $\tilde{G}$ is able to acquire a supersymmetry-breaking mass as a result of the super-Higgs mechanism [86], and the $\tilde{G}$ mass is related to the $\tilde{\chi}_1^0$ lifetime by the C_{grav} parameter of the minimal GMSB model. Therefore an upper limit on the cross section can be set as a function of $\tilde{G}$ mass (Table 6.8).

To demonstrate the limit setting, we take a signal point, $\tilde{\chi}_1^0$ lifetime $c\tau = 5$ cm for example, corresponding to $\tilde{G}$ mass 0.10 keV. With the selection criteria and the total acceptance times efficiency of $0.01578 \pm 0.00059(stat.) \pm 0.00395(syst.)$, the upper limits from this measurement are determined to be 0.14 pb for the assumption of a log-normal

background uncertainty distribution. Thus, in minimal GMSB model for any neutralino decay into a photon and a $\tilde{G}$ (mass = 0.10 keV), the upper limit of cross section for pair-production of $\tilde{\chi}_1^0$'s, each of which decays into a photon and invisible particles, is set to 0.14 pb at the 95% confidence level.

$c\tau$ [cm]	2	5	10	25
$\tilde{G}$ mass [keV]	0.06	0.10	0.14	0.22
σ [pb] 95% C.L	0.24	0.14	0.12	0.16

Table 6.8: 95% C.L. upper limits on the cross section for pair production of neutralinos, each of which decays into a photon and invisible particles, as a function of the neutralino lifetime in the minimal GMSB model.

In summary, the photon conversion impact parameter method has been applied to search for new physics involving long-lived particles decaying into photons. By using a data-driven method to estimate the background, a search in the final state of γs, jets and missing transverse energy has been performed. Upper limits on the cross section for such particles from pair-production decaying into a photon and invisible particles are set as a function of the long-lived particle's lifetime.

Chapter 7

Conclusions

In this dissertation, a method using the photon impact parameter is presented for searches for long-lived particles decaying into photons. The impact parameter of the photon relative to the beam-beam collision point can be reconstructed using converted photons. The method is sensitive to lifetimes of $\mathcal{O}$(0.1 - 1 ns), corresponding to decay lengths of $\mathcal{O}$(1 - 10 cm). Upper limits at the 95% confidence level are presented on the cross section for pair-production of such particles, each of which decays into a photon and invisible particles. The results are not sensitive to the neutralino mass for the mass in the order of 100 GeV. The results are model-independent and not limited to any specific GMSB model. This analysis has a relatively lower E_T^{miss} threshold (E_T^{miss} >30 GeV) compared with other SUSY searches involving photons [57, 4], which opens the possibility of searches for long-lived particles with relatively low E_T^{miss} in the final state, such as some low scale gauge mediation scenarios [28].

Bibliography

[1] M. E. Peskin, "Beyond the standard model," arXiv:hep-ph/9705479 [hep-ph].

[2] J. T. Ruderman and D. Shih, "General Neutralino NLSPs at the Early LHC," arXiv:1103.6083 [hep-ph].

[3] G. L. e. a. Bayatian, *CMS Physics Technical Design Report Volume I: Detector Performance and Software.* Technical Design Report CMS. CERN, Geneva, 2006.

[4] **CMS** Collaboration, C. Collaboration, "Search for Supersymmetry in Events with Photons, Jets and Missing Energy," *CMS Physics Analysis Summary* **SUS-11-009** (2011) .

[5] C.-N. Yang and R. L. Mills, "Conservation of Isotopic Spin and Isotopic Gauge Invariance," *Phys.Rev.* **96** (1954) 191–195.

[6] **LEP Working Group for Higgs boson searches, ALEPH Collaboration, DELPHI Collaboration, L3 Collaboration, OPAL Collaboration** Collaboration, R. Barate *et al.*, "Search for the standard model Higgs boson at LEP," *Phys.Lett.* **B565** (2003) 61–75, arXiv:hep-ex/0306033 [hep-ex].

[7] **CDF and DØ** Collaboration, "Higgs Searches at the Tevatron,". http://www.ino.tifr.res.in/MaKaC/getFile.py/access?contribId=117&sessionId=4&resId=0&materialId=slides&confId=79.

[8] **CMS** Collaboration, "Combined Standard Model Higgs boson searches with up to 2.3 inverse femtobarns of pp collision data at sqrt(s)=7 TeV at the LHC,".

[9] "Combined Standard Model Higgs boson searches with up to 2.3 fb-1 of pp collisions at sqrts=7 TeV at the LHC," Tech. Rep. ATLAS-CONF-2011-157, CERN, Geneva, Nov, 2011.

[10] H. Georgi and S. Glashow, "Unity of All Elementary Particle Forces," *Phys.Rev.Lett.* **32** (1974) 438–441.

[11] T. Kajita, "Searches for neutrino oscillations. I: Solar and atmospheric neutrinos: Evidence for oscillation of atmospheric neutrinos,".

[12] **Super-Kamiokande Collaboration** Collaboration, Y. Fukuda *et al.*, "Evidence for oscillation of atmospheric neutrinos," *Phys.Rev.Lett.* **81** (1998) 1562–1567, arXiv:hep-ex/9807003 [hep-ex].

[13] W. Siegel, "Introduction to string field theory," arXiv:hep-th/0107094 [hep-th].

[14] N. Arkani-Hamed, S. Dimopoulos, and G. Dvali, "The Hierarchy problem and new dimensions at a millimeter," *Phys.Lett.* **B429** (1998) 263–272, arXiv:hep-ph/9803315 [hep-ph].

[15] S. P. Martin, "A Supersymmetry primer," arXiv:hep-ph/9709356 [hep-ph].

[16] D. Kazakov, "Beyond the standard model," arXiv:hep-ph/0411064 [hep-ph].

[17] L. J. Hall, J. D. Lykken, and S. Weinberg, "Supergravity as the Messenger of Supersymmetry Breaking," *Phys.Rev.* **D27** (1983) 2359–2378.

[18] S. K. Soni and H. Weldon, "Analysis of the Supersymmetry Breaking Induced by N=1 Supergravity Theories," *Phys.Lett.* **B126** (1983) 215. Revised version.

[19] G. Giudice and R. Rattazzi, "Theories with gauge mediated supersymmetry breaking," *Phys.Rept.* **322** (1999) 419–499, arXiv:hep-ph/9801271 [hep-ph].

[20] S. Dubovsky, D. Gorbunov, and S. V. Troitsky, "Gauge mechanism of mediation of supersymmetry breaking," *Phys.Usp.* **42** (1999) 623–651, arXiv:hep-ph/9905466 [hep-ph].

[21] A. H. Chamseddine, R. L. Arnowitt, and P. Nath, "Locally Supersymmetric Grand Unification," *Phys.Rev.Lett.* **49** (1982) 970.

[22] D. Kaplan, G. Kribs, and M. Schmaltz, "Supersymmetry breaking through transparent extra dimensions,".

[23] L. Randall and R. Sundrum, "Out of this world supersymmetry breaking," *Nucl.Phys.* **B557** (1999) 79–118, arXiv:hep-th/9810155 [hep-th].

[24] **CDF Collaboration** Collaboration, T. Aaltonen *et al.*, "Inclusive Search for Squark and Gluino Production in $p\bar{p}$ Collisions at $\sqrt{s} = 1.96$-TeV," *Phys.Rev.Lett.* **102** (2009) 121801, arXiv:0811.2512 [hep-ex].

[25] S. Dimopoulos, S. D. Thomas, and J. D. Wells, "Sparticle spectroscopy and electroweak symmetry breaking with gauge mediated supersymmetry breaking," *Nucl.Phys.* **B488** (1997) 39–91, arXiv:hep-ph/9609434 [hep-ph].

[26] G. D. Kribs, "Distinguishing anomaly mediation from gauge mediation with a wino NLSP," *Phys.Rev.* **D62** (2000) 015008, arXiv:hep-ph/9909376 [hep-ph].

[27] P. Meade, N. Seiberg, and D. Shih, "General Gauge Mediation," *Prog.Theor.Phys.Suppl.* **177** (2009) 143–158, arXiv:0801.3278 [hep-ph].

[28] J. D. Mason, D. E. Morrissey, and D. Poland, "Higgs Boson Decays to Neutralinos in Low-Scale Gauge Mediation," *Phys.Rev.* **D80** (2009) 115015, arXiv:0909.3523 [hep-ph].

[29] P. Meade, M. Reece, and D. Shih, "Prompt Decays of General Neutralino NLSPs at the Tevatron," *JHEP* **1005** (2010) 105, arXiv:0911.4130 [hep-ph].

[30] S. Ambrosanio, G. L. Kane, G. D. Kribs, S. P. Martin, and S. Mrenna, "Search for supersymmetry with a light gravitino at the Fermilab Tevatron and CERN LEP colliders," *Phys.Rev.* **D54** (1996) 5395–5411, arXiv:hep-ph/9605398 [hep-ph].

[31] P. Meade, M. Reece, and D. Shih, "Long-Lived Neutralino NLSPs," *JHEP* **1010** (2010) 067, arXiv:1006.4575 [hep-ph].

[32] **CDF Collaboration, representing the CDF Collaboration** Collaboration, A. L. Scott, "Search for long-lived parents of the Z^0 boson," *Int.J.Mod.Phys.* **A20** (2005) 3263–3266, arXiv:hep-ex/0410019 [hep-ex].

[33] L. Evans and P. Bryant, "LHC Machine," *Journal of Instrumentation* **3** no. 08, (2008) S08001. http://stacks.iop.org/1748-0221/3/i=08/a=S08001.

[34] O. S. Brning, P. Collier, P. Lebrun, S. Myers, R. Ostojic, J. Poole, and P. Proudlock, *LHC Design Report*. CERN, Geneva, 2004.

[35] **CMS** Collaboration, "The CMS experiment at the CERN LHC," *Journal of Instrumentation* **3** no. 08, (2008) S08004. http://stacks.iop.org/1748-0221/3/i=08/a=S08004.

[36] **ATLAS** Collaboration, "The ATLAS Experiment at the CERN Large Hadron Collider," *Journal of Instrumentation* **3** no. 08, (2008) S08003. http://stacks.iop.org/1748-0221/3/i=08/a=S08003.

[37] **CMS** Collaboration, "Measurement of CMS Luminosity,".

[38] **CMS** Collaboration, "CMS Luminosity-Public Results,". https://twiki.cern.ch/twiki/bin/view/CMSPublic/LumiPublicResults.

[39] **CMS Collaboration** Collaboration, R. Adolphi *et al.*, "The CMS experiment at the CERN LHC," *JINST* **3** (2008) S08004.

[40] **CMS Collaboration** Collaboration, S. Chatrchyan *et al.*, "Performance of the CMS Hadron Calorimeter with Cosmic Ray Muons and LHC Beam Data," *JINST* **5** (2010) T03012, arXiv:0911.4991 [physics.ins-det].

[41] **CMS Collaboration** Collaboration, S. Dasu *et al.*, "CMS. The TriDAS project. Technical design report, vol. 1: The trigger systems,".

[42] **CMS Collaboration** Collaboration, e. Sphicas, P., "CMS: The TriDAS project. Technical design report, Vol. 2: Data acquisition and high-level trigger,".

[43] "The CMS Offline SW Guide,". https://twiki.cern.ch/twiki/bin/view/CMSPublic/SWGuide.

[44] **CMS** Collaboration, "CMSSW and Event Data Model (EDM),". https://twiki.cern.ch/twiki/bin/view/CMSPublic/WorkBookCMSSWFramework.

[45] "The Worldwide LHC Computing Grid (WLCG) project,". http://lcg.web.cern.ch/LCG/public/default.htm.

[46] **CMS Collaboration** Collaboration, V. Khachatryan *et al.*, "CMS Tracking Performance Results from early LHC Operation," *Eur.Phys.J.* **C70** (2010) 1165–1192, arXiv:1007.1988 [physics.ins-det].

[47] R. E. Kalman, "A New Approach to Linear Filtering and Prediction Problems," *Transactions of the ASME–Journal of Basic Engineering* **82** no. Series D, (1960) 35–45.

[48] M. Cacciari, G. P. Salam, and G. Soyez, "The Anti-k(t) jet clustering algorithm," *JHEP* **0804** (2008) 063, arXiv:0802.1189 [hep-ph].

[49] **CMS** Collaboration, C. Collaboration, "Jet Performance in pp Collisions at $\sqrt{s}$=7 TeV," *CMS Physics Analysis Summary* **JME-10-003** (2010) .

[50] **CMS** Collaboration, C. Collaboration, "The Jet Plus Tracks Algorithm for Calorimeter Jet Energy Corrections in CMS," *CMS Physics Analysis Summary* **JME-09-002** (2009) .

[51] **CMS** Collaboration, C. Collaboration, "Particle-Flow Event Reconstruction in CMS," *CMS Physics Analysis Summary* **PFT-09-001** (2009) .

[52] R. Frhwirth, "A Gaussian-mixture approximation of the BetheHeitler model of electron energy loss by bremsstrahlung,".

[53] J. B. M. Sani, M. Pieri, "Electron GSF Tracking Commissioning with first LHC Data," *CMS NOTE* **2010/038** (2010) .

[54] G. Kitagawa, "Non-Gaussian State-Space Modeling of Nonstationary Time Series," *Journal of the American Statistical Association* **Vol. 82, No. 400 (Dec., 1987)** (1987) 1032–1041.

[55] E. M. et al., "Electron Reconstruction in the CMS Electromagnetic Calorimeter," *CMS NOTE* **2001/034** (2001) .

[56] T. C. A. et al., "A Simple Method of Shower Localization and Identification in Laterally Segmented Calorimeters," *Nuclear Instruments and Methods in Physics Research Section A* **311** (1992) 130–138.

[57] **CMS Collaboration** Collaboration, S. Chatrchyan *et al.*, "Search for Supersymmetry in *pp* Collisions at $\sqrt{s} = 7$ TeV in Events with Two Photons and Missing Transverse Energy," *Phys. Rev. Lett.* **106** (2011) 211802, arXiv:1103.0953 [hep-ex]. * Temporary entry *.

[58] "Monte Carlo Method,". http://mathworld.wolfram.com/MonteCarloMethod.html.

[59] T. Sjostrand, S. Mrenna, and P. Z. Skands, "PYTHIA 6.4 Physics and Manual," *JHEP* **0605** (2006) 026, arXiv:hep-ph/0603175 [hep-ph].

[60] B. Andersson, G. Gustafson, G. Ingelman, and T. Sjostrand, "Parton Fragmentation and String Dynamics," *Phys.Rept.* **97** (1983) 31–145.

[61] M. L. Mangano, M. Moretti, F. Piccinini, R. Pittau, and A. D. Polosa, "ALPGEN, a generator for hard multiparton processes in hadronic collisions," *JHEP* **0307** (2003) 001, arXiv:hep-ph/0206293 [hep-ph].

[62] F. Maltoni and T. Stelzer, "MadEvent: Automatic event generation with MadGraph," *JHEP* **0302** (2003) 027, arXiv:hep-ph/0208156 [hep-ph].

[63] M. Asai, "Geant4-a simulation toolkit," *Trans.Amer.Nucl.Soc.* **95** (2006) 757.

[64] N. Marinelli, "Track finding and identification of converted photons," *CMS NOTE* **2006/005** (2006) .

[65] P. et al, "Very Large Impact Parameter Track Reconstruction," *CMS NOTE* **2009/107** (2009) .

[66] T. S. K.Prokofiev, "A Kinematic fit and a decay chain reconstruction library," *CMS IN* **2004/020** (2004) .

[67] **CMS** Collaboration, "Studies of Tracker Material," *CMS Physics Analysis Summary* **TRK-10-003** (2010) . `http://cdsweb.cern.ch/record/1279138`.

[68] M. J. Strassler and K. M. Zurek, "Echoes of a hidden valley at hadron colliders," *Phys.Lett.* **B651** (2007) 374–379, `arXiv:hep-ph/0604261 [hep-ph]`.

[69] L. M. Carpenter, "Surveying the Phenomenology of General Gauge Mediation," `arXiv:0812.2051 [hep-ph]`.

[70] A. Rajaraman, Y. Shirman, J. Smidt, and F. Yu, "Parameter Space of General Gauge Mediation," *Phys.Lett.* **B678** (2009) 367–372, `arXiv:0903.0668 [hep-ph]`.

[71] S. Abel, M. J. Dolan, J. Jaeckel, and V. V. Khoze, "Phenomenology of Pure General Gauge Mediation," *JHEP* **0912** (2009) 001, `arXiv:0910.2674 [hep-ph]`.

[72] **D0 Collaboration** Collaboration, V. Abazov *et al.*, "Search for long-lived particles decaying into electron or photon pairs with the D0 detector," *Phys.Rev.Lett.* **101** (2008) 111802, `arXiv:0806.2223 [hep-ex]`.

[73] **CDF Collaboration** Collaboration, A. Abulencia *et al.*, "Search for heavy, long-lived particles that decay to photons at CDF II," *Phys.Rev.Lett.* **99** (2007) 121801, `arXiv:0704.0760 [hep-ex]`.

[74] B. Allanach, M. Battaglia, G. Blair, M. S. Carena, A. De Roeck, *et al.*, "The Snowmass points and slopes: Benchmarks for SUSY searches," *Eur.Phys.J.* **C25** (2002) 113–123, `arXiv:hep-ph/0202233 [hep-ph]`.

[75] **CMS** Collaboration, P. V. Group, "Physics Validation: Pileup Studies,". `https://twiki.cern.ch/twiki/bin/view/CMS/PileupInformation`.

[76] **CMS** Collaboration, C. Collaboration, "MET Performance in pp Collisions at $\sqrt{s}$=7 TeV," *CMS Physics Analysis Summary* **JME-10-009** (2010) .

[77] **CMS** Collaboration, C. Collaboration, "Measurement of the Differential Isolated Prompt Photon Production Cross Section in *pp* Collisions at $\sqrt{s} = 7$ TeV," *CMS Physics Analysis Summary* **QCD-10-037** (2010) .

[78] **CMS** Collaboration, C. Collaboration, "Search for a Higgs boson decaying into two photons in the CMS detector," *CMS Physics Analysis Summary* **HIG-11-010** (2011) .

[79] **CMS** Collaboration, C. Collaboration, "Search for new physics with long-lived particles decaying to photons and missing energy," *CMS Physics Analysis Summary* **EXO-11-067** (2011) . `http://cdsweb.cern.ch/record/1394286`.

[80] P. V. R. Fruehwirth, W. Waltenberger, "Adaptive Vertex Fitting," *CMS NOTE* **2007/008** (2007) .

[81] W. Erdmann, "Offline Primary Vertex Reconstruction with Deterministic Annealing Clustering," *CMS IN* **2011/014** (2011) .

[82] M. A. et al, "Search for General Gauge Mediated Supersymmetry with Two Photons and Missing Transverse Energy," *CMS NOTE* **2011/289** (2011) .

[83] A. L. Read, "Presentation of search results: The CL(s) technique," *J.Phys.G* **G28** (2002) 2693–2704.

[84] L. Moneta, K. Belasco, K. Cranmer, A. Lazzaro, D. Piparo, *et al.*, "The RooStats Project," *PoS* **ACAT2010** (2010) 057, `arXiv:1009.1003 [physics.data-an]`. * Temporary entry *.

[85] **CMS** Collaboration, "Physics Analysis Oriented Event Display (Fireworks / cmsShow),". `https://twiki.cern.ch/twiki/bin/view/CMSPublic/WorkBookFireworks`.

[86] S. Deser and B. Zumino, "Broken Supersymmetry and Supergravity," *Phys.Rev.Lett.* **38** (1977) 1433.

[87] M. Buican, P. Meade, N. Seiberg, and D. Shih, "Exploring General Gauge Mediation," *JHEP* **0903** (2009) 016, `arXiv:0812.3668 [hep-ph]`.

[88] M. Pioppi, "Iterative Tracking," *CMS IN* **2007/065** (2007) .

[89] W. A. et al, "Track Reconstruction with Cosmic Ray Data at the Tracker Integration Facility," *CMS NOTE* **2009/003** (2009) .

[90] N. et al, "Track finding and identification of converted photons with the CMS Tracker and ECAL," *CMS NOTE* **2008/102** (2008) .

[91] **CMS** Collaboration, R. Adolphi *et al.*, "The CMS experiment at the CERN LHC," *JINST* **0803** (2008) S08004.

[92] **Particle Data Group** Collaboration, K. Nakamura *et al.*, "Review of particle physics," *J.Phys.G* **G37** (2010) 075021.

[93] **CMS** Collaboration, C. Collaboration, "Isolated Photon Reconstruction and Identification at $\sqrt{s}$=7 TeV," *CMS Physics Analysis Summary* **EGM-10-006** (2010) . `http://cdsweb.cern.ch/record/1324545`.

[94] **CMS** Collaboration, C. Collaboration, "Jet Energy Corrections determination at *sqrts*=7 TeV," *CMS Physics Analysis Summary* **JME-10-010** (2010) .

[95] S. Abel, M. J. Dolan, J. Jaeckel, and V. V. Khoze, "Pure General Gauge Mediation for Early LHC Searches," *JHEP* **1012** (2010) 049, `arXiv:1009.1164 [hep-ph]`. * Temporary entry *.

[96] E. Nakamura and S. Shirai, "Discovery Potential for Low-Scale Gauge Mediation at Early LHC," *JHEP* **1103** (2011) 115, arXiv:1010.5995 [hep-ph].

[97] G. H. H. Liu, N. Marinelli, "Conversion reconstruction with tracker seeded tracks in CMS 7 TeV data," *CMS NOTE* **2010/101** (2010) .